Scaling of Hybrid Wing-Body-Type Aircraft: Exploration Through High-Fidelity Aerodynamic Shape Optimization

by

Thomas A. Reist

A thesis submitted in conformity with the requirements
for the degree of Doctor of Philosophy
Graduate Department of Aerospace Science and Engineering
University of Toronto

Abstract

Scaling of Hybrid Wing-Body-Type Aircraft:
Exploration Through High-Fidelity
Aerodynamic Shape Optimization

Thomas A. Reist
Doctor of Philosophy
Graduate Department of Aerospace Science and Engineering
University of Toronto
2016

Unconventional aircraft configurations have the potential to reduce aviation's contribution to climate change through substantial reductions in fuel burn. One promising configuration which has received much attention is the hybrid wing-body (HWB). Due to the lack of design experience for unconventional configurations, high-fidelity design and optimization methods will be critical in their development.

This thesis presents the application of a gradient-based aerodynamic shape optimization algorithm based on the Reynolds-averaged Navier-Stokes equations to the aerodynamic design of conventional tube-and-wing (CTW) and HWB aircraft. The optimal aerodynamic shapes and performance for a range of aircraft sizes including regional, narrow-body, mid-size, and wide-body classes are found so as to characterize the aerodynamic efficiency benefits of the HWB configuration with respect to equivalent CTW designs. Trim-constrained drag minimization is performed at cruise, with a large design space of over 400 design variables. The smaller optimized HWBs, including the regional and narrow-body classes, while more aerodynamically efficient, burn at least as much fuel as to the equivalently optimized CTWs due to their increased weight, while the larger wide-body-class HWB has almost 11% lower cruise fuel burn.

To investigate alternative configurations which may yield improved efficiency, exploratory optimizations with significant geometric freedom are then performed, resulting in a set of

novel shapes with a more slender lifting fuselage and distinct wings. Based on these exploratory results, new lifting-fuselage configurations (LFCs) are designed. The slenderness of the LFC fuselage decreases with aircraft size, such that, for the largest class, the LFC reverts to a classical HWB shape. This new configuration offers higher aerodynamic efficiency than the HWBs, with the smaller classes seeing the largest benefit from the new configuration. This new lifting-fuselage concept offers 6% lower cruise fuel burn than the CTW in the regional class, and a marginal benefit in the narrow-body class. The effects of cruise altitude, stability requirements, and weight sensitivity are also examined.

To my parents

Acknowledgements

First and foremost, I would like to thank Dr. David W. Zingg for his support and guidance throughout this work. Ever patient and supportive, his passion for his work was always inspirational. In addition, his commitment to the UTIAS community helps to make it a world-class institution, while simultaneously being a unique and connected environment.

Thanks to my doctoral committee members, Dr. Prasanth Nair and Dr. Craig Steeves for their guidance throughout this work, and to Dr. Dimitri Mavris and Dr. Markus Bussmann for their contribution to my final oral examination.

Many thanks are owed to Dr. Jason Hicken, Dr. Michal Osusky, and Dr. Lana Osusky for their work on the development of the code that forms the foundation of this thesis, as well as for their help and guidance on its use and best practices when I first joined the computational aerodynamics group. Also to Howard Buckley and the rest of the Computational Aerodynamics Group for their support.

Thanks to Pete Szabo, Jon Gammell, Pat McGarey, and the ShockWaves for great times on the field, and to the rest of the student body for making my time at UTIAS enjoyable.

To my family, Rachel, Justin, and Luke, but particularly to my parents. Your selfless level of support, from my formative years to today, is something I can only ever aspire too.

And to Cora, thank you for your unwavering support throughout this journey. You were always there to believe in me, even when I did not.

I am grateful to the National Science and Engineering Research Council of Canada, the Government of Ontario, the University of Toronto, and to Bombardier Aerospace for their financial support of this work.

Thank you all,
Thomas A. Reist

University of Toronto Institute for Aerospace Studies
September, 2016

Contents

List of Tables

List of Figures

Nomenclature

Symbols

$\boldsymbol{\mathcal{A}}$	Discrete flow Jacobian
$\mathcal{AR}$	Aspect ratio ($\mathcal{AR} = b^2/S$)
$\mathcal{AR}_{\text{wet}}$	Wetted aspect ratio ($\mathcal{AR}_{\text{wet}} = b^2/S_{\text{wet}}$)
α	Aircraft angle-of-attack
b	Total aircraft span
$\boldsymbol{B}$	Cartesian coordinates of B-spline control points
c	Local chord length
c_d, C_D	Section and aircraft drag coefficient, respectively
C_{Df}	Friction drag coefficient
C_{Dp}	Pressure drag coefficient
c_l, C_L	Section and aircraft lift coefficient, respectively
c_m, C_M	Section and aircraft pitching moment coefficient , respectively
C_p	Coefficient of pressure
C_f	Skin friction coefficient
c_T	Thrust specific fuel consumption
D	Drag force
$\boldsymbol{f}_m$	Implicit force vector for the linear elasticity problem at mesh increment m
$\boldsymbol{K}_m$	Linear elasticity stiffness matrix at mesh increment m
L	Lift force
L/D	Lift-to-drag ratio
M	Mach number, pitching moment
$\boldsymbol{\mathcal{M}}_m$	Mesh movement equation residual at increment m
N_m	Number of mesh movement increments
$\mathcal{N}$	B-spline basis function
$\boldsymbol{Q}$	Vector of continuous conserved flow variables
$\boldsymbol{\mathcal{Q}}$	Vector of discrete conserved flow variables

q	Dynamic pressure
R	Range
$\boldsymbol{\mathcal{R}}$	Discrete flow residual
S	Reference wing area
S_{wet}	Wetted area
t/c	Section thickness normalized with local chord length
T	Thrust
V	Velocity, volume
W	Aircraft weight
W_{fuel}	Fuel weight
x, y, z	Streamwise, spanwise, and vertical coordinates, respectively
$\boldsymbol{x}$	3-vector of Cartesian coordinates $[x, y, z]^T$
$\boldsymbol{X}$	Vector of design variables
$\boldsymbol{\xi}$	3-vector of parametric coordinates $[\xi, \eta, \zeta]^T$

Acronyms

AoA	Angle-of-attack
APM	Airport planning manual
ASO	Aerodynamic shape optimization
CAD	Computer aided design
CFD	Computational fluid dynamics
CG	Center of gravity
CTW	Conventional tube-and-wing
DOC	Direct operating cost
GCROT	Generalized conjugate residual with inner orthogonalization and outer truncation
GMRES	Generalized minimum residual
HWB	Hybrid wing-body
ICA	Initial cruise altitude
ICAO	International Civil Aviation Organization
ISA	International Standard Atmosphere
LFC	Lifting-fuselage configuration
MAC	Mean aerodynamic chord
MFW	Maximum fuel weight
MTOW	Maximum take-off weight
MZFW	Maximum zero-fuel weight

OEW	Operating empty weight
PAX	Passengers
PRSEUS	Pultruded rod stitched efficient unitized structure
RDV	Region design variables
TSFC	Thrust specific fuel consumption
ULD	Unit load device

Subscripts

0	Initial value, fixed value
∞	Freestream value
w	Wing
t	Tail (horizontal stabilizer)
f	Fin (vertical stabilizer)

Chapter 1

Introduction

1.1 Motivation

The aviation industry is being faced with great pressure to reduce fuel burn. This is motivated by 1) the desire of operators to reduce operating costs and 2) concerns over aviation's contributions to anthropogenic climate change. In contrast to aviation's other environmental impacts, such as noise and local air quality, reducing fuel burn aligns with both economic and environmental motivations. From an economic standpoint, as fuel is a large portion of direct operating costs (DOC), reducing fuel burn leads to a direct reduction in DOC, and hence aircraft manufactures are incentivised to reduce fuel burn so as to make their products more competitive. Environmentally, carbon-dioxide (CO_2) emissions are a large component of an aircraft's greenhouse gas emissions [1], and reducing fuel burn leads to a proportional reduction in CO_2 emissions. There are of course other emissions which can contribute to climate change such as NO_x, particulates, and water vapour [1,2], but in contrast to the relationship between CO_2 and climate change, the relationship between these latter emissions and operating conditions, atmospheric conditions, and climate change are more complex. So while reducing non-CO_2 emissions must be addressed for both climate change and other environmental reasons, reducing CO_2 through reduced fuel burn has a direct and quantifiable impact on reducing both greenhouse gases and operating costs.

For an aircraft in flight, the rate of fuel burn is given by

$$\frac{dW_{\text{fuel}}}{dt} = \frac{dW}{dt} = -c_T T \tag{1.1}$$

where W_{fuel} is the fuel weight, W is the total aircraft weight, c_T is the thrust-specific fuel consumption for a given jet engine at certain operating conditions and throttle setting,

and T is the thrust, equal to drag, D, for steady-level flight [3]. Thus, reducing drag will in turn reduce the fuel-flow rate and hence total fuel burn. Rearranging and integrating Equation 1.1 for cruise, assuming a cruise-climb profile, i.e. a constant lift-to-drag ratio, L/D, with changes in weight, yields the Breguet range equation

$$R = \frac{VL/D}{c_T} \ln\left(\frac{W_0 + W_{\text{fuel}}}{W_0}\right) \tag{1.2}$$

which can be rearranged to obtain an expression for cruise fuel burn

$$W_{\text{fuel}} = W_0 \left[\exp\left(\frac{Rc_T}{VL/D}\right) - 1\right] \tag{1.3}$$

where R is the cruise segment range, V is the cruise speed, and W_0 is the fixed weight of the aircraft. From this it is evident that cruise fuel burn can be reduced by reducing aircraft weight, W_0, thrust-specific fuel-consumption, c_T, and increasing aerodynamic efficiency, L/D. This thesis aims to focus on the last contributor, aerodynamic efficiency.

The International Civil Aviation Organization (ICAO), has laid out a target of carbon-neutral growth by 2020 and a 50% reduction in CO_2 emissions by 2050 relative to 2010 levels. They propose achieving this target through a combination of 1) known technology, operations and infrastructure measures, 2) the use of biofuels, 3) additional technologies such as drag reduction and unconventional airframes, and 4) economic measures such as carbon taxes and emission trading schemes. Conventional tube-and-wing (CTW) aircraft have become highly optimized over the years, and while it is still possible to obtain aerodynamic improvements, a step change in aerodynamic efficiency will be required if ICAO's carbon-reduction goals are to be met. Such a step change may be possible through novel aircraft configurations. A number of such configurations have been proposed, including strut-braced wings [4–6], the 'double-bubble' concept [7], joined-wing systems [8–12], and blended, or hybrid, wing-bodies (HWBs)[1] [13].

The HWB configuration has shown much promise for the potential to reduce both emissions and noise [5,13,14]. As will be demonstrated in the following section, most work has focused on large aircraft, to which the intrinsic design features of this concept lend themselves well. This thesis will examine the ability of the HWB concept to provide fuel burn savings across a range of aircraft sizes, with an emphasis on smaller aircraft for which there has been little focus in the past.

[1]While traditionally referred to as 'blended wing-body' (BWB) aircraft, in recent years the name 'hybrid wing-body' (HWB) has become widely used. Boeing and European organizations tend to use the term BWB, while NASA and other US entities have migrated to the HWB moniker.

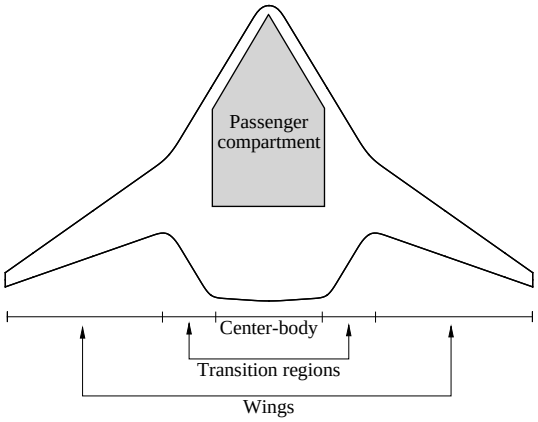

Figure 1.1: Basic HWB concept.

1.2 The Hybrid Wing-Body Concept

The HWB configuration combines the fuselage, stabilizers, wings, and potentially the propulsion system, into one highly integrated airframe, a notional example of which is shown in Figure 1.1. The main advantages, challenges, and the work that has been conducted to investigate this concept are detailed in the following sections.

1.2.1 HWB Advantages and Challenges

Aerodynamics

The HWB's primary benefit is arguably an increase in aerodynamic efficiency. The two largest potential aerodynamic benefits come from reductions in wetted area and increased span. It is argued by Liebeck [13] that the HWB offers lower wetted area than an equivalent CTW design. For large aircraft this is true; however, as shall be shown in this thesis, this benefit is highly dependent on aircraft size. Any reduction in wetted area leads to a proportional decrease in parasitic drag. The highly span-loaded[2] nature of the HWB has the potential to allow for a larger wing-span without an increase in wing structural weight. These two features allow for a large wetted aspect ratio, $\mathcal{R}_{\text{wet}} = b^2/S_{\text{wet}}$, with which the lift-to-drag ratio scales [15]. Additional aerodynamic benefits come from the integrated nature of the wings and fuselage which does not lead to interference drag as seen with CTW designs. In addition, due to the large lifting area HWBs typically have low wing-loading, W/S. This can allow for lower approach speeds, simpler high-lift devices, or a combination thereof.

[2]Span-loading is the distribution of the payload laterally along the span as opposed to longitudinally along the fuselage length.

Structures

The primary structural benefit of the HWB concept is the increased span-loading, which aligns the inertial and lifting loads, thus reducing bending moments in the structure. However, as a consequence, this leads to the pressurized passenger compartment not taking the form of a cylinder. Thus, one of the major challenges of the HWB concept is the design of a non-cylindrical pressure vessel which can support the internal pressure loads without leading to a large weight increase. An additional challenge is the coupling of the pressure and bending loads imposed on the center-body. For a CTW design these two loads are largely independent, but for the HWB concept the center-body structure must simultaneously support the internal pressure loads and the bending loads transfered from the wing. Studies by Mukhopadhyay et al. at NASA [16,17] investigated via 2D nonlinear beam-column analysis four concepts for non-cylindrical pressure vessels, all of which are significantly heavier than a cylindrical section. This was followed by 3D FEM analysis and optimization of rib-stiffened 2-5 bay multi-bubble configurations whose weight was compared with a similarly optimized cylindrical fuselage for a 400-500-passenger class aircraft. It was found that these configurations are between 20% and 110% heavier than the cylindrical fuselage on a per-unit floor area basis. The heaviest non-cylindrical designs are the four and five bay concepts, as they required additional reinforcement external to the pressure vessel in order to accommodate bending loads without buckling.

To address these issues, NASA and Boeing are developing the 'Pultruded Rod Stitched Efficient Unitized Structure' (PRSEUS) concept [18] as part of the ERA program. This concept consists of foam core frames and pultruded rod stringers which are all stitched to a composite skin. The stitched construction eliminates mechanical fasteners and the associated tear-through failure, as well as providing a damage-arresting mechanism in the event of skin failure. In addition to the structural concept, a key portion of the PRSEUS program was the demonstration of efficient, high-volume, and quality manufacturing methods through the use of unitized panels which can be efficiently manufactured in an out-of-autoclave process. The PRSEUS concept has progressed through a series of technology demonstration tests including single-panel and unit-cube specimens subjected to tension, buckling, and pressure load tests. In these tests, the PRSEUS concept demonstrated its damage-arresting capability and buckling resistance [19]. This program has culminated in the design and construction of a 75% scale HWB center-body specimen which is currently undergoing final testing [20].

Using the new PRSEUS technology, cylindrical, double-bubble, and multi-bay HWB fuselage sections were sized by Mukhopadhyay et al. [17,21]. With the PRSEUS panels, the multi-bay HWB fuselage is the lightest on a weight-per-unit-area basis of all the concepts

studied, and is 22% lighter than a conventional aluminum cylindrical fuselage, 4% lighter than an advanced composite cylindrical fuselage, and 21% lighter than a double-bubble fuselage.

When the HWB concept was first proposed, the design of an efficient non-cylindrical pressure vessel was one of the biggest challenges to the feasibility of the HWB concept. As shown above, work over the past 20 years has addressed this issue, such that a competitive non-cylindrical fuselage seems, at the very least, feasible.

Stability and Control

One of the primary challenges for the HWB concept is stability and control due to the absence of an empennage. The absence of a horizontal tail aft of the center of gravity (CG) makes attaining trim and a positive static margin difficult. Historically, longitudinal static stability of flying wings is obtained by either sweeping the wings and adding significant washout such that the tips carry little, or negative, lift, or by using reflexed airfoils [22]. However, these are both inefficient, as sweeping and unloading the tips decreases the effective span and does not allow for an elliptical lift distribution, and reflexed airfoils are highly fore-loaded which degrades transonic performance. As part of the Silent Aircraft Initiative, Sargeant et al. [23] designed an HWB which features a 'leading edge carving' on the center-body such that most of the center-body lift is carried ahead of the CG, while the wing uses supercritical sections for improved transonic performance, and a nearly elliptical lift distribution. Due to the large center-body chords, the center-body sections are only lightly loaded such that good transonic performance is preserved. In addition, the aerodynamic centers of the center-body airfoils are located at about 35% chord, compared to the typical 25%, thus moving the aircraft neutral point aft.

Cook and de Castro [24] examined the trim and control requirements for a large HWB at low speed. For the HWB studied, the elevator angles for trim for a range of CG locations, approach speeds, and static margins were studied. For both highly stable and unstable CG locations, the elevator deflection angles for trim were impractical, particularly at low speeds. For example, an approach speed of 150 kts would require elevator deflections of approximately $\pm 22^\circ$ for static margins of -23% and $+18\%$, respectively; deflections which are likely infeasible since additional deflection margins required for maneuvering would also be required. At the same speed, a stable design with $K_n = +2\%$ would only require a 6° deflection, and an unstable design with $K_n = -5\%$ would require a 3° deflection. Also, the associated angles-of-attack for the unstable configuration are lower and hence more favourable. Similar trends were seen for the 'elevator angle per g'; highly stable or unstable

designs would require excessive control power, and a nearly neutrally stable aircraft, for which stability augmentation would be required, is desirable to minimize control power.

Garmendia et al. [25] conducted low-fidelity studies on the optimal number and arrangement of control surfaces for longitudinal control. Four different control surface configurations with between 7 and 11 electrically actuated trailing edge control effectors were analyzed and compared on the basis of power consumption and their system-level fuel burn effect. Their work showed that a large center-body elevon generated the highest hinge moment, and therefore the highest control power requirement, for a given deflection rate. Thus, to minimize control power, the center-body elevon should be used only for low-frequency control, as is done with the all-moving tail in conventional aircraft, to maintain trim as fuel is burned. The remaining control surfaces, which are significantly smaller, are then better suited for control requiring higher deflection rates. However, using the center-body elevon as a trim-only device resulted in a decreased lift-to-drag ratio and hence higher fuel burn.

Due to the large number of redundant control surfaces on HWB aircraft, control allocation becomes more challenging than for conventional aircraft. Control power minimization through optimal control allocation was investigated by Chhabra et al. as part of the OREIO project [26]. Using 15 control surfaces, including 2 rudders mounted on vertical tails, control power, for which the sum of all hinge moments acted as a surrogate, was minimized using a neural network and NASTRAN based optimization. For a $2.5g$ pull-up maneuver, it was shown that, with an optimal control distribution, the sum of the hinge moments was up to 45% lower than if the center-body mounted elevon was used for trim in isolation. Control deflections ranged from $-6\,^\circ$ to $+25\,^\circ$.

Garmendia and Mavris [27] investigated solving the redundant control problem using various solution techniques for approach, and approach in a crosswind. In all cases trim was obtained without control saturation (defined as $\pm 30\,^\circ$), with the 35 knot crosswind requiring almost $\pm 30\,^\circ$ deflections. They showed that the redundant control problem can be highly multimodal, and that seeking a solution that minimizes drag is ineffective, as it yields approach drag so low that a throttle setting below flight idle would be required. Imposing minimum throttle constraints to comply with FAR requirements resulted in very large control deflections, such that the control surfaces acted as air brakes, leaving little remaining margin for maneuvering.

A means of providing lateral control is an open issue for the HWB configuration due to the lack of (a) vertical stabilizer(s), or fin(s). Meheut et al. [28] examined the impact of winglets on lateral stability, and of winglet mounted rudders on directional control, at both low and high-speed conditions for the VELA2 configuration. At both low and high-speed

conditions the VELA2 configuration had the required negative rolling moment derivative, C_{l_β}, with and without the winglet. However, with the exception of the wingletted configuration at high-speed, the VELA2 configuration did not have the required positive yawing moment derivative, C_{n_β}. The winglet mounted rudders did not provide sufficient lateral control at both low and high-speeds. The authors recommend the use of center-body mounted fins for adequate lateral stability and control. Similar conclusions with respect to directional stability are drawn by Rahman and Whidborne [29], although details of their sizing procedure are lacking.

Propulsion

While existing engine technology could simply be slung underneath the wings as is done in modern CTW aircraft, more innovative engine installations could yield both performance improvements and noise reduction through acoustic shielding. The simplest option is the use of pylon-mounted engines mounted on the aft upper surface of the center-body. With the trend of increasing bypass ratio on modern turbofans, and consideration of open-rotor technology, mounting on the aft center-body negates ground clearance issues associated with under-wing mounting. Aft-mounted engines would, however, not be without challenges. The ingestion of a relatively uniform flow-field at the fan face is important for engine efficiency and longevity. This could prove challenging if there is little vertical separation between the engine and upper surface, or at high angles-of-attack. In addition, the installation of engines on the suction side of the lifting-body would require careful design of the upper surface and pylons to reduce interference drag and distortion at the fan-face. The most integrated propulsion concept is the use of boundary-layer ingesting engines, where the engines are mounted flush with, or recessed into, the fuselage and ingest the low-speed flow in the boundary layer. This increases the momentum change imparted by the engine, resulting in a lower TSFC [30]. The challenge with this concept is the design of distortion tolerant engines, as the flow entering the fan is highly non-uniform [30–33]. Also, engine tolerance to the ingestion of ice or other debris which may accumulate on the upper surface must be addressed. Even more advanced concepts such as distributed propulsion have also been proposed [34,35].

Acoustics

The primary acoustic benefits of the HWB concept stem from both engine placement and reductions in airframe noise. As discussed in the previous section, mounting the engines above the fuselage not only provides for the potential of TSFC improvements, but also

allows the body and any vertical stabilizers to serve as acoustic shields to radiate engine sound away from the ground. The use of acoustic shielding has been investigated by NASA and Boeing [36–40] and formed a core component of the Silent Aircraft Initiative [41,42].

The low wing-loading typical of HWB aircraft also allows for both a reduction in approach speed as well as the potential for smaller and simpler high-lift systems. Both of these contribute to reductions in airframe noise and have been studied by NASA [40,43] and as part of the Silent Aircraft Initiative [44]. As noted in the above works, with improvements in engine acoustics design and with the acoustic shielding provided by the HWB configuration, airframe noise can easily become the dominant noise source, particularly on approach. Thus, reduction of airframe noise becomes critical for overall noise reduction.

Operations and Passenger Acceptance

The introduction of HWB aircraft would have implications for air-traffic management and operations. As shown by Ghigliazza et al. [45], the strength of the wake vortex is proportional to the aircraft span-loading, W/b, which is typically smaller for HWB aircraft than for CTWs. They showed that during take-off and approach, the most safety critical conditions for minimum separation, the 300 and 800-passenger HWBs studied produced up to a 20% weaker wake, defined in terms of the induced velocity in the wake at a given separation. This corresponds to wakes generated by 150 and 200-passenger CTWs, respectively. This would then allow for potentially decreased separation between aircraft on take-off and approach.

The resulting increase in airport utilization was studied by Martinez-Val et al. [46] where they demonstrated up to a 46% increase in passenger traffic, should half of the medium and heavy conventional aircraft be replaced with 300-passenger HWBs, and up to a 63% increase if 70% of medium and 30% of heavy aircraft were replaced with 300-passenger HWBs. Some of the increased passenger traffic gains were due to decreased separation distances, resulting in up to an 11% increase in aircraft operations, but the main increase in passenger traffic came from the increased capacity of the HWBs; the study did not consider various sizes of HWBs. In addition, the assumption was made that the airport infrastructure would not become saturated, and that the increased span of the HWBs would not be gate class limited. The authors also point out that the higher cruise altitude implied by the lower wing-loading of HWBs would allow for increased utilization of airspace by freeing space at lower altitudes which could then be utilized by conventional aircraft. While increased utilization of higher flight levels by HWB aircraft would free congested airspace, the impact on operations of having to climb to such a high altitude would have to be addressed, particularly for short-range missions.

In addition, the radically different cabin design could potentially reduce turn-around times due to the use of multiple aisles for passenger loading and unloading. In some cases existing unit load devices (ULDs) may not fit efficiently in HWB cargo holds, thus requiring special ULDs for this type of aircraft. This would have implications on cargo usage, particularly if cargo was being transferred between HWB and CTW aircraft.

Acceptance by the flying public of HWB aircraft may pose challenging, in part due to the radically different cabin layout. Van der Voet et al. [47] presented the results of surveys on passenger acceptance of HWB interiors. The need for windows, or some way of orienting the passenger within the unconventional cabin, was one of the dominant desires. While exterior cameras presenting a real-time exterior image locally to each seat were desired by respondents, this solution was thought to be insufficient for passenger acceptance as it does not aid in passenger orientation within the cabin and does not alleviate potential feelings of claustrophobia. A number of cabin configurations and interior designs were presented with the aim of providing a suitable passenger experience, feasible emergency egress options, and maximization of revenue space.

Passenger acceptance of unconventional cabin configurations could pose a challenge. In addition, due to their lower wing-loading and the lateral offset of passengers from the aircraft centerline, HWBs would likely exhibit degraded ride quality compared to CTWs. The degree to which this is true could perhaps be mitigated by active-control, but would need to be assessed for passenger acceptance.

Emergency egress from the non-cylindrical cabin has often been raised as an issue. Fire and evacuation simulations and experiments by Galea et al. [48] on a single-deck, 1000-passenger HWB demonstrated an average 'out of aircraft' evacuation time of 85.9 sec. The 'on-ground' evacuation requirement is 90 sec. The primary challenges to quick evacuation found in the experimental demonstration were passenger unfamiliarity with the unconventional cabin layout, and the distance between crew and exits, which made direction of passengers difficult. Both of these factors would be less pronounced in a smaller aircraft.

Additional considerations such as crashworthiness [49] and design for commonality [13, 50] have also been explored.

1.2.2 Global HWB Projects

Most of the work discussed above has been conducted as part of several research programs which have been conducted globally to establish the performance potential of the HWB concept and develop enabling technologies. Some of the main research programs are summarized

below.

The European Union has funded a series of research programs aimed at the development of the HWB concept. The first, from 2000-2003, was the Multidisciplinary Optimization of an HWB (MOB) project which developed a multidisciplinary design optimization framework distributed across a number of partner organizations [51,52]. This distributed computational design engine was used for the design of a cargo HWB aircraft with a 260,000 lb payload. High-fidelity aerodynamic shape optimization for improved cruise performance was also performed [53,54]. From 2002-2005 the Very Efficient Large Aircraft (VELA) project examined two 700-passenger HWB concepts with a focus on maximizing cruise efficiency [55,56] and developing structural [57] and control [28,58] solutions. From 2005-2009 the New Aircraft Concepts Research (NACRE) [59] expanded on the results of the VELA project and studied a 750-passenger HWB. Finally, from 2008-2012, the Active Control for Flexible Aircraft (ACFA 2020) [60] project examined a scaled down version of the NACRE design for 450-passengers and aimed to reduce structural loads and improve ride quality through the development of an active control system. In addition, Russia's Central Aerohydrodynamic Institute (TsAGI) conducted conceptual-level design studies of 750 passenger class aircraft with varying levels of 'blending' between the fuselage and wings. These ranged from a conventional fuselage with an extended wing root, or 'hybrid' configuration, to a pure flying wing, with the hybrid solution offering the highest aerodynamic efficiency [61].

Significant work has been done in the United States towards the development of the HWB concept. McDonnell Douglas conducted studies into the feasibility of an 800-passenger HWB aircraft in the 1990s [13,62]. Upon McDonnell Douglas' acquisition by Boeing in 1997, the focus of these studies shifted to a 450-passenger design [13]. These studies demonstrated the potential benefits of the design; however, at the time, the design of an efficient non-cylindrical pressure vessel was an open question, upon which the viability of the concept rested. Much of this work, led by Robert Liebeck, formed some of the most seminal contributions to the HWB concept, and led to the development of the X-48B/C flight demonstrators. The focus of these demonstrators was to examine the low-speed and post-stall behaviour of the concept [63,64].

More recently, significant amounts of work have been conducted by Boeing and NASA as part of the NASA funded Environmentally Responsible Aviation (ERA) project. One of Boeing's first contributions to this project was their Subsonic Ultra Green Aircraft Research (SUGAR) program to investigate unconventional aircraft concepts, including the HWB, with the potential to provide significant reductions in environmental impacts [5,65]. The 'SUGAR Ray', the HWB design to come out of the SUGAR program, was to serve as a 155-passenger

transport with a gross weight of just over 182,000 lb. More recently, Boeing has pursued studies into the use of open rotors on HWBs, leading to the Open Rotor Engine Integration On an HWB (OREIO) design [66,67]. This concept is designed as a freighter, of a size similar to that of a 220-passenger class HWB.

MIT led a team in the development of an aircraft for which reduced noise was the main design driver. This was the Silent Aircraft Initiative, and led to the development of the 220-passenger SAX-40 design [23,44]. In response to NASA's ERA program, MIT expanded this work so as to meet the targets of the ERA program. This resulted in the development of both the D8 'double-bubble' concept as well as an HWB based off of the SAX-40 [7,14,68]. Also starting from the SAX-40 design, Boeing developed the N2-A/B/EXTE HWB designs to meet the ERA program's N+2 targets. These designs have served as the basis for further studies by NASA, Boeing, and others [25,27,36,69].

Most of the above programs examined HWBs for 220-1,000 passengers. The HWB's intrinsic design features lend themselves well to large aircraft. However this design may also offer advantages for smaller aircraft. Nickol examined a series of HWB aircraft ranging from 98-400 passengers using low-fidelity conceptual design methods [70]. The aerodynamic and fuel burn benefits were most significant for the larger aircraft, with the 98 passenger aircraft burning more fuel than a comparable tube-and-wing aircraft. However, the fuel burn disadvantage of the small HWB was highly sensitive to drag. Thus, if a suitable drag reduction can be achieved through aerodynamic shape optimization, perhaps resulting in a shape significantly different than that assumed by Nickol, the HWB could potentially be more fuel efficient than the tube-and-wing aircraft even for smaller aircraft classes. A 100-passenger HWB-like short take-off and landing concept developed by a team lead by California Polytechnic State University featured a design with a largely conventional cylindrical fuselage integrated into a wing with a large root chord [71]. This concept was primarily used to investigate the use of circulation control, and no performance comparisons with conventional designs are publicly available.

The potential performance benefits of the HWB, as found in the above projects which provide relative performance numbers, are summarized in Table 1.1.

Table 1.1: Summary of the relative performance of HWBs from the literature. Values in parentheses are relative to conventional tube-and-wing designs.

Study	PAX [–]	Span [ft]	MTOW [lb]	L/D [–]	Fuel burn [%]	Advanced technology	Notes
Boeing [13]	800	289	823,000 (−15%)	23.0 (+21%)	(−28%)	BLI, CFRP	
	450	249	– (−18%)	–	(−32%)	CFRP	Relative to early 2000-era conventional aircraft
Boeing [5]	155	169	182,500 (+35%)	26.6 (+27%)	(+2%)	CFRP, LFC, advanced propulsion	43% fuel burn reduction relative to 2008 conventional aircraft
NASA [70]	98	142	101,000 (+10%)	20.7 (+5%)	(+4.0%)	Advanced composites, LFC, advanced propulsion, gust load alleviation, other	Performance relative to advanced tube-and-wing aircraft
	160	182	166,100 (+18%)	23.1 (+17%)	(+4.0%)		
	216	210	286,900 (+6%)	22.3 (+12%)	(−2.3%)		
	301	240	542,600 (+1%)	23.5 (+9%)	(−6.0%)		
	400	260	693,600 (+9%)	23.7 (+16%)	(−4.6%)		
MIT [14]	180	164	173,000 (−1%)	22.1	(−45%)	Advanced composites, BLI, advanced propulsion	Performance relative to existing in-service aircraft
	250	207	378,800 (−25%)	24.4			
	350	213	487,600 (−36%)	24.1	(−54%)		

BLI: Boundary layer ingestion CFRP: Carbon fiber reinforced polyme LFC: Laminar flow control

Due to their unconventional nature, design of HWB aircraft is not well served using correlation based methods, or in some cases, low-fidelity methods. For example, Hileman et al. [44] demonstrate that the use of two-dimensional section design for the HWB center-body is insufficient due to the highly three-dimensional flow on the HWB center-body. Also from an aerodynamic modelling perspective, linear aerodynamic models, such as panel methods, are incapable of modelling, and thus designing for, transonic conditions. As fidelity is increased to Euler codes, which can capture compressible phenomena, viscous effects are still not captured. Since one of the drivers of the HWB configuration is the potential for wetted area reductions, modelling of viscous effects is vital and is provided by the solution of the Navier-Stokes equations. This work will make use of the Reynolds-averaged Navier-Stokes (RANS) equations.

In addition, the absence of designer experience for unconventional configurations motivates the use of numerical optimization in design. Modelling of the design problem thus becomes critical, so that the optimizer has information of the relevant physics underlying the problem. Using high-fidelity[3] methods in optimization provides sufficient information of the flow physics to allow the optimizer to appropriately design the aerodynamic shape.

Vehicle design is a highly multidisciplinary problem. While this work uses high-fidelity aerodynamic modelling to determine optimal aerodynamic performance, as will be discussed later, constraints and assumptions are imposed so as to reflect the requirements of other disciplines.

1.3 High-Fidelity Aerodynamic Shape Optimization of HWB Aircraft

High-fidelity aerodynamic shape optimization has been applied to HWB aircraft by a number of researchers, the most significant examples of which are outlined below.

Peigin and Epstein [72] performed section and twist optimization of the MOB configuration using a genetic optimizer and a Navier-Stokes solver with reduced order modelling. They demonstrated that the performance difference between two designs, one with, and one without, a pitching moment constraint is quite small; however the corresponding section shapes are markedly different. Without the pitching constraint the optimizer designs highly aft-loaded sections, and hence a strong nose-down moment. The addition of the pitching moment constraint leads to more fore-loaded sections while still being shock-free. In addition,

[3]While there is no clear demarcation between levels of fidelity, in this work high-fidelity aerodynamic modelling is defined as the solution of nonlinear flow models, such as the Euler and Navier-Stokes equations.

three-point optimizations including high-speed and high-lift conditions are considered. As with the pitching moment constraint, these multipoint optimizations gave markedly different shapes yet similar performance at the main design point.

As part of the MOB project, Qin et al. [53] investigated the optimal spanwise lift distribution for the MOB configuration. They claim that an elliptical lift distribution is not optimal as the resulting high local lift coefficients on the outboard wing result in high wave drag and additional trim drag. They argue that an average triangular and elliptical distribution is optimal as it is a compromise between wave and induced drag. However, these lift distributions were attained by specifying a twist distribution, and are still not shock-free, and the lift-to-drag ratio is under 15. Other means of wave drag reduction, such as section optimization, could potentially not require sacrificing the elliptical lift distribution and are addressed by Qin et al. [73]. Section optimization using multi-fidelity (Euler and RANS) and RANS-based optimization with an SQP method are performed in 2D and then the optimized sections are mapped back to the 3D model, which is analyzed. The maximum lift-to-drag ratio improves, yet wave drag returns when the shock-free sections are mapped back to the 3D design. Finally, 3D Euler-based trim-constrained drag minimization optimization is performed with twist and section control on the wing. The resulting shape is then analyzed with a RANS solver. Unlike the previous optimizations, this full 3D optimization is able to largely eliminate wave drag, while also achieving an induced drag reduction. This study highlights the need for full 3D surface optimization in order to minimize the sum of all drag sources, as 2D and quasi-3D methods are insufficient due to the largely 3D nature of the flow caused by the high sweep angles associated with the configuration. More recently, Le Moigne and Qin [74] used a gradient-based optimizer coupled with an Euler solver to perform section and twist optimization of the MOB configuration. Similar behaviour to that of Peigin and Epstein is seen, where the optimizer fore-loads the sections to obtain trim; however in this work significant aft-loading is present on the center-body. In addition, the authors demonstrate the same small decrement in performance due to the pitching moment constraint. The optimal lift distribution found in this paper is nearly elliptical, in contrast to the previous works of Qin [53,73] which suggested that a more lightly loaded tip was beneficial due to wave drag. The necessity of full 3D surface optimization is also highlighted in this work, as it has allowed both the minimization of induced and wave drag. All of the Euler-optimized designs are analyzed with the Navier-Stokes equations. This leads to one of the main points of the authors, that the performance benefit seen when conducting Euler-based optimization translates to the viscous design space. However, this assertion is made by comparing viscous performance on Euler-optimized designs only, without quantification

of the potential performance had they been optimized using the Navier-Stokes equations. So while some of the drag reduction will remain, such as the reduction of wave drag, the full benefit may not have been realized, as described by Osusky and Zingg [75]. In all of these MOB-based works, the final lift-to-drag ratio is always less than 16, which is uncompetitive with CTW aircraft.

ONERA and Airbus conducted gradient-based optimization of the AVECA configuration using the Navier-Stokes equations, as described by Méheut et al. [76] Several optimizations were performed for various planforms derived by perturbing parameters such as chord, taper, and span of the original design. Each of these planforms was optimized to minimize drag at the cruise condition by changing chord and twist, while constraining the pitching moment and center-body shape. One of the more notable contributions was the consideration of a take-off rotation constraint, which was accounted for via a minimum pitching moment at zero lift. The authors found that the imposition of this constraint resulted in no performance degradation at the main design point; however it did decrease the maximum attainable lift-to-drag ratio.

RANS-based aerodynamic shape optimization was performed by Lyu and Martins [77] for a large HWB based on that of Liebeck [13]. Their primary focus was the characterization of optimal performance when subjected to different design variables and constraints. Lift-constrained drag minimization optimizations with twist and section freedom served as the basis of comparison. They then sequentially added trim, static margin, and bending moment constraints to quantify the performance trade-offs. The imposition of a trim constraint incurred a 5 count, or 5.6%, drag penalty which was primarily caused by the creation of reflexed sections and increased induced drag caused by unloading of the swept wing. Further drag reduction was achieved through the addition of a center of gravity design variable which was limited through a 1% static margin constraint; the original designs all being neutrally stable. Finally, the introduction of a root bending moment constraint, which required that the bending moment not increase relative to the twist-optimized baseline, and planform variables led to a further one count of drag reduction. In addition, a multipoint optimization was performed, which, as expected, increased the size of the region with 99% of the maximum ML/D.

All of the works described above discuss very large capacity HWBs. Kuntawala et al. [78] used gradient-based optimization and the Euler equations to perform aerodynamic shape optimization of a small HWB with section, twist, and planform freedom. Drag reductions of up to 50% were achieved relative to the baseline design through reduction of wave and induced drag. The authors note that, in agreement with Qin et al. [53], an elliptical lift-

distribution is not necessarily optimal for minimum total drag, as a compromise between wave and induced drag reduction must be found. This work used some of the same aerodynamic shape optimization framework as the current work.

1.4 Thesis Outline and Objectives

The majority of works presented above have studied large HWB aircraft, with little consideration of the potential for smaller classes. This is particularly true for the studies which have applied high-fidelity aerodynamic shape optimization to the HWB concept. In addition, all of the high-fidelity aerodynamic shape optimization studies have utilized a relatively restricted geometric design space, typically with only section, twist, and in some cases wing sweep freedom. While there can be good cause to do this, particularly when the given planform has been well studied for a given size of aircraft, the potential may exist, especially for smaller aircraft, for further performance improvements to be found through optimization with increased geometric freedom. In addition, most of these high-fidelity studies do not provide performance comparisons between similarly optimized CTW aircraft.

Thus, this thesis has the following objectives:

1. Examine how the efficiency of the HWB concept relative to CTWs scales with aircraft size, including down to smaller classes of aircraft for which this concept is often not considered, and whether high-fidelity aerodynamic shape optimization can be used to design HWBs which offer performance benefits in classes for which the HWB is not believed to be beneficial.
2. Investigate alternative configurations which may be more efficient than HWB aircraft, and how the optimal shape changes with aircraft size.

Each of the above objectives will be accomplished through:

1. The application of RANS-based aerodynamic shape optimization to the aerodynamic design of both CTW and HWB aircraft for a range of aircraft classes, from regional-jets to wide-bodies.
2. Exploratory optimization based upon the RANS equations, and with significant geometric freedom, such that alternative configurations can be found through optimization.

This thesis is structured as follows. Chapter 2 will outline the aerodynamic shape optimization framework which has been developed within the computational aerodynamics

group and the author's contributions to it. Chapter 3 will present the conceptual design of both conventional and HWB aircraft for a range of classes. Chapter 4 presents the application of the high-fidelity aerodynamic shape optimization tool to the problem at hand, including the optimization problem definition and results. Chapter 5 presents the exploratory optimization of loosely constrained HWB design problems for each class which leads to a new configuration. Chapter 6 will compare the performance of the three concepts, including the effect of cruise altitude and reduced structural weight. Chapter 7 further studies the effect of different constraints and assumptions for the regional class aircraft. Finally, conclusions and recommendations for future work are presented in Chapter 8.

Chapter 2

High-Fidelity Aerodynamic Shape Optimization

The high-fidelity aerodynamic shape optimization (ASO) framework used has been developed largely through the efforts of Hicken and Zingg [79,80], Hicken [81], M. Osusky and Zingg [82], M. Osusky [83], L. Osusky et al. [84], and L. Osusky [85]. It consists of four primary components which will be described below:

1. Geometry parameterization and mesh movement scheme
2. Computational fluid dynamics (CFD) solver for the Euler and Navier-Stokes equations
3. Gradient evaluation via the discrete adjoint method
4. Gradient-based optimizer

This framework has been used extensively for ASO of various problems including the benchmark validation problems of the AIAA Aerodynamic Design Optimization Discussion Group [86–88], induced drag minimization of non-planar wings [6,89], optimization of wings in transonic [90] and turbulent flows [84], the design of low-sweep wings [91], investigation of the multimodality of ASO problems [92], and the optimization of unconventional aircraft [6,78,93–95] aircraft. This framework has also been extended to aerostructural optimization [96,97].

2.1 Geometry Parameterization and Mesh Movement

For ASO, or indeed any optimization scheme which requires user-independent geometric changes, some method of changing the geometry (i.e. geometric control), and subsequently

the CFD grid (i.e. mesh movement), in response to design variable changes is required.

2.1.1 Geometric Parameterization

The simplest method of controlling the geometry is the use of the CFD grid points as design variables with some form of gradient smoothing [98]. While this does not require geometric parameterization, it results in a large number of geometric design variables, which can greatly hinder optimizer performance. Alternatively, some form of geometric parameterization such as bump functions [99], class/function shape transformation methods [100], and methods based on basis functions (e.g. Bézier surfaces, Bernstein polynomials, radial basis functions, or non-uniform rational B-splines) can be used. Free-form deformation methods do not parameterize the geometry, but rather its deformation [101]. An industrially attractive option is the use of CAD-based control [102]. However, this is complicated by the proprietary nature of most CAD package source code which renders accurate surface sensitivity evaluation difficult. These methods can also be used in conjunction with each other, such as in the work of Gagnon and Zingg [6,11].

For this work, Basis-spline (B-spline) surfaces of the form

$$S(\boldsymbol{\xi}) = \sum_{i=1}^{N_i} \sum_{j=1}^{N_j} \boldsymbol{B}_{ij} \mathcal{N}_i(\xi) \mathcal{N}_j(\eta) \tag{2.1}$$

are used to parameterize the geometry, where S is the surface representation in $\mathbb{R}^2$, $\boldsymbol{\xi} = (\xi, \eta)$ is the parametric space on $[0, 1]$, $\boldsymbol{B}$ are the coordinates of the surface control points, and $\mathcal{N}$ are the basis functions which are joined on a non-decreasing knot vector. The design variables are (or control), the control points, $\boldsymbol{B}$, which in turn control the surface geometry. Further details can be found in Hicken and Zingg [80].

2.1.2 Mesh Movement

After the geometry has been moved, some way of moving the CFD grid in a corresponding way is required. In theory, for a new geometry the CFD grid could simply be regenerated. However, this is typically not a simple task for complex geometries, and obtaining the mesh sensitivities can be difficult. Another, relatively simple, approach is algebraic mesh movement [90]; however this is restricted to cases with small geometric changes and can be difficult to apply to arbitrary multiblock grid topologies, and on complex geometries. The use of radial basis functions which interpolate surface changes into the CFD grid is another

option [103]. The method used in this work is based on the equations of linear elasticity, as implemented by Truong et al. [104] and Hicken and Zingg [80].

In this method, the geometry parameterization and mesh movement are tightly coupled. The B-spline surface representation given in Equation 2.1 is extended to three dimensions, where now, each block of the CFD grid is parameterized to obtain a B-spline volume, given as

$$V(\boldsymbol{\xi}) = \sum_{i=1}^{N_i} \sum_{j=1}^{N_j} \sum_{k=1}^{N_k} \boldsymbol{B}_{ijk} \mathcal{N}_i(\xi) \mathcal{N}_j(\eta) \mathcal{N}_k(\zeta) \tag{2.2}$$

where V is the volume representation in $\mathbb{R}^3$, and the parameter vector is now $\boldsymbol{\xi} = (\xi, \eta, \zeta)$. The parametric representation is obtained by

1. Calculating the parameter values, $\boldsymbol{\xi}$, based on the CFD grid points via an arc-length parameterization.
2. Calculating the knot vectors upon which the basis functions, $\mathcal{N}$, are defined such that an equal number of parameter values fall within each knot vector. This ensures that the B-spline control points mimic the spacing of the CFD grid.
3. A least-squares fitting routine is then used to determine the B-spline control point locations, $\boldsymbol{B}$, that best fit the mesh.

The geometry of interest, i.e. the aerodynamic surface, is then simply a subset of the B-spline volume, for example $S(\xi, \eta) = V(\xi, \eta, \zeta = 0)$, termed a 'patch'. The B-spline control points which define this surface are either the geometric design variables themselves, or are controlled by the design variables.

The mesh movement is accomplished by treating the B-spline volume representation as a linear elastic solid. The B-spline control points form a control grid which is used to construct a series of N_m finite element problems of the form

$$\boldsymbol{\mathcal{K}}_m(\boldsymbol{B}_{m-1})(\boldsymbol{B}_m - \boldsymbol{B}_{m-1}) - \boldsymbol{f}_m = \boldsymbol{\mathcal{M}}_m = 0, \qquad m = 1, \ldots, N_m \tag{2.3}$$

where $\boldsymbol{\mathcal{K}}_m(\boldsymbol{B}_{m-1})$ is the stiffness matrix, $\boldsymbol{B}_m$ are the B-spline control points at each of the $m = 1, \ldots, N_m$ increments, $\boldsymbol{f}_m$ is the implicit force vector defined based upon the known displacements of a subset of B-spline control points, such as on the surface or far-field. The dependence of the stiffness matrix on $\boldsymbol{B}$ arises from the use of a spatially varying Young's modulus which is a function of cell volume and orthogonality, see Hicken and Zingg [80] for more details. Since the finite element problem is linear (based upon the assumption of small strains), for cases where shape changes are large and this assumption is no longer valid, the

problem can be solved in N_m increments, where the known B-spline surface displacements on the surface are broken down as

$$\boldsymbol{B}_m = \boldsymbol{B}_0 + \frac{m}{N_m}\left(\boldsymbol{B}_{N_m} - \boldsymbol{B}_0\right), \qquad m = 1, \ldots, N_m \tag{2.4}$$

and the subscript 0 corresponds to the values on the initial, i.e. unmoved, control grid. At each mesh increment, m, the linear system of Equation 2.3 is solved in parallel using the conjugate gradient method with a block Jacobi preconditioner with the third-party package PETSc [105] to a relative tolerance of 10^{-12}. Typically, between five and ten mesh increments are used for the results presented in this thesis. This coupled geometry parameterization and mesh movement scheme has been found to be very robust for large shape changes, while incurring little computational cost relative to a flow solution. For the problems considered in this thesis, mesh movement is typically accomplished in 30-60 sec, or 3-5% of the time required for a flow solution.

2.1.3 Geometric Design Variable Definition

While the B-spline control points on the aerodynamic surface provide significant geometric control, their use as design variables is often unintuitive and cumbersome when switching between various block, and hence patch, topologies. A method of easily specifying the desired geometric freedom for a range of problems is thus required. To address this, a means of controlling the control point locations for a range of geometries and topologies has been developed, and is termed 'region design variables', RDVs.

The basic idea behind RDVs is the definition of 'components' and 'regions'. Based on user input, a given number of patches are assigned to each region in a (j, k) grid, and regions are in-turn assigned to each component. A sample wing-body geometry illustrating this layout is shown in Figure 2.1 with components, regions and patches identified.

Those control points which fall adjacent to stitches are not included as region variables, but rather are determined as a combination of their neighbours such that G^0, G^1 and pseudo-G^2 continuity[1] is maintained on all stitches.[2] The combination of patches into regions allows for the use of arbitrarily fine block topologies with a single set of design variable definitions and input files.

[1] G^k continuity refers to the geometry, but not necessarily its underlying parameterization, being k^{th}-order continuous.

[2] This is only pseudo-curvature continuity, as the relation used is only valid for curves and not surfaces, and a slight modification is used to preserve CFD grid quality with respect to the original fit. These approximations have been found to introduce curvature continuity errors of no more than a few percent.

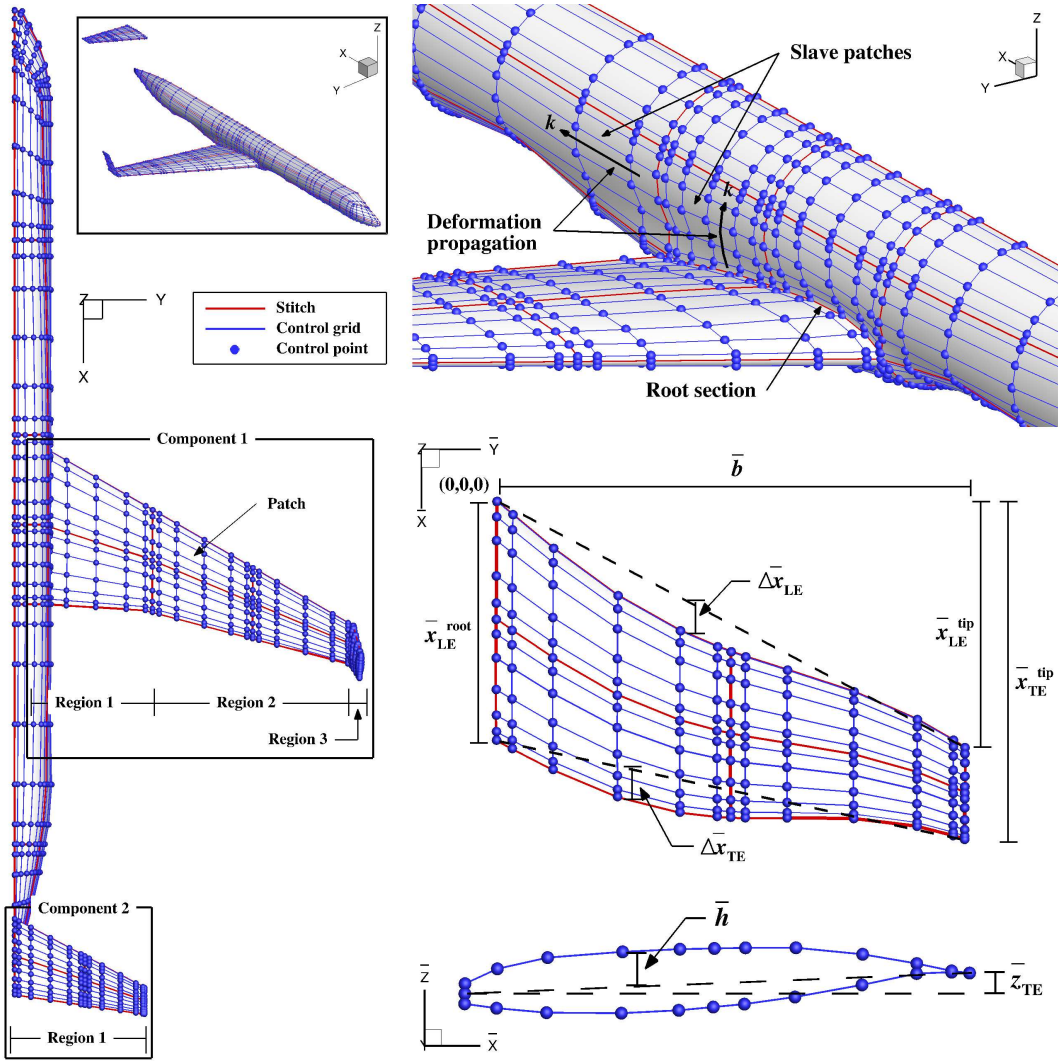

Figure 2.1: Left: Sample wing-body geometry showing the decomposition of patches, regions, and components. Top right: Wing-body junction showing slave patches and directions over which wing-root geometry changes propagate. Middle right: A sample region showing the primary variables which make up the planform geometric design variables. Lower right: Sample section showing section shape and twist variables. Note that not all design variables are shown in this figure. Namely, a $\Delta\bar{z}_{\mathrm{LE/TE}}$ is also present which corresponds with the marked $\Delta\bar{x}_{\mathrm{LE/TE}}$.

Each region is defined in its own coordinate system, which allows the extraction of intuitive design variables for each region, regardless of whether the different regions have significantly different orientations in global-space. A sample region along with its design variables is shown in the lower right of Figure 2.1. There are many possible ways of defining the design variables such that the region control points can be completely defined. The variable definition used is chosen such that as many constraints as possible can be expressed

as linear functions. Due to SNOPT's ability to satisfy linear constraints immediately (see Section 2.3), this property allows for 1) the determination of infeasible designs at the beginning of an optimization, and 2) the ability to use the variable and constraint definitions to manipulate the geometry at the start of an optimization based upon user input. A sample of these local coordinate systems is shown on the lower right of Figure 2.1. In this local coordinate system, variables are automatically extracted and defined as shown.

Upon specification of these local variables, the global control points of region R, can be constructed via

$$\boldsymbol{B}_R = \sum_{r=1}^{R-1} \begin{bmatrix} \bar{x}_{\text{LE}}^{\text{tip}} \\ \bar{b}\cos\Gamma \\ \bar{b}\sin\Gamma \end{bmatrix}_r + \phi(\Gamma_R)\ \bar{\boldsymbol{x}}_R \tag{2.5}$$

where Γ is the dihedral variable for each region,[3] ϕ is the rotation matrix about the $\bar{x}$-axis given by

$$\phi(\Gamma) = \begin{bmatrix} 1 & 0 & 0 \\ 0 & \cos\Gamma & -\sin\Gamma \\ 0 & \sin\Gamma & \cos\Gamma \end{bmatrix}$$

and $\bar{\boldsymbol{x}}_R$ are the coordinates of the control points expressed in the region coordinate system.

In order to represent more complex geometries, e.g. those with multiple surfaces, the concept of 'components' is introduced. A component is simply a collection of regions. Each component is isolated from other components and contains its own unique set of regions. Components may not intersect or share patches. This is intended, for example, to allow for the optimization of full aircraft configurations, where say the wing is one component and the horizontal tail is another, and each can be controlled independently based on the role of that component. Such an example is shown for a two-component geometry in Figure 2.1. The global space referenced previously is actually the local space of a component. Components can translate and rotate about the spanwise axis, and in so doing, all the regions which are included on that component translate and rotate accordingly. Components also allow for the interaction of patches which are included in the design space, e.g. a wing, and those which are not directly controlled by the optimizer, e.g. a fuselage. If a component is mounted on a symmetry plane, no special treatment is needed. If a component is mounted on another set of patches, as in the wing-fuselage case, the control points on the mount, e.g. the fuselage, are controlled via algebraic movement based on the movement of the control points on the

[3]This is the only region variable which is expressed in the global coordinate system.

root of the component via

$$\boldsymbol{B}_k = \boldsymbol{B}_k^0 + \Delta\boldsymbol{B}\left[\frac{1+\cos(\pi S_k)}{2}\right]^\beta \qquad k = 1, \ldots, N_k \tag{2.6}$$

for each control mesh grid line k normal to the component root section. The 3-vector $\boldsymbol{B}_k$ contains the new x, y, z control point coordinates on the mount surface, $\boldsymbol{B}_k^0$ are the original control points on the mount surface, and $\Delta\boldsymbol{B}$ is the movement of the component root relative to the original shape. The variable S_k is the arc length along the grid line given by

$$S_k = \frac{\sum_{i=2}^{k} ||\boldsymbol{B}_i - \boldsymbol{B}_{i-1}||_2}{\sum_{i=2}^{N_k} ||\boldsymbol{B}_i - \boldsymbol{B}_{i-1}||_2} \tag{2.7}$$

and β is a factor which allows control over how far along the grid line the geometry change at the component root is propagated. Large values of β better maintain the initial mount geometry; however if large changes of the component root occur, the resulting mount geometry may be severely warped. The value $\beta = 2$ is used for the results presented in this thesis.

2.2 Flow Solver

The governing equations used in this thesis are the Reynolds-averaged Navier-Stokes equations in three dimensions. Given in conservative form in Cartesian coordinates, they take the form

$$\frac{\partial \boldsymbol{Q}}{\partial t} + \frac{\partial \boldsymbol{E}}{\partial x} + \frac{\partial \boldsymbol{F}}{\partial y} + \frac{\partial \boldsymbol{G}}{\partial z} = \frac{\partial \boldsymbol{E_v}}{\partial x} + \frac{\partial \boldsymbol{E_v}}{\partial y} + \frac{\partial \boldsymbol{G_v}}{\partial z} \tag{2.8}$$

where $\boldsymbol{Q}$ is the 5-vector of conserved quantities (mass, momentum, and energy), $\boldsymbol{E}$, $\boldsymbol{F}$, and $\boldsymbol{G}$ are the inviscid fluxes, and $\boldsymbol{E_v}$, $\boldsymbol{F_v}$, and $\boldsymbol{G_v}$ are the viscous fluxes. The viscous fluxes in Equation 2.8 contain terms due to turbulence which cannot be evaluated. Thus, the one-equation Spalart-Allmaras turbulence model [106] is used to solve for the turbulent viscosity. This introduces a sixth PDE and solution variable, which is included in the discrete solution vector. While the Spalart-Allmaras model contains a trip function to account for laminar-turbulent transition, it is not used in this work and fully turbulent flow is assumed.

The flow domain is discretized on a grid which is decomposed into multiple blocks to facilitate parallel computation. For each block, the Navier-Stokes equations are then non-dimensionalized and transformed onto a uniformly spaced computational grid. In this computational space, the derivatives are approximated by finite-differences using summation-

by-parts operators, while simultaneous approximation terms are used to enforce both physical boundary conditions and those at block interfaces [107].

The introduction of the turbulence model and the discretization of the governing equations leads to a large system of nonlinear ordinary differential equations of the form

$$\frac{\partial \boldsymbol{\mathcal{Q}}}{\partial t} + \boldsymbol{\mathcal{R}}(\boldsymbol{\mathcal{Q}}) = 0 \tag{2.9}$$

where $\boldsymbol{\mathcal{Q}}$ and $\boldsymbol{\mathcal{R}}$ are the discrete solution vector and flow residual for the domain, respectively. In this work the steady solution $\boldsymbol{\mathcal{R}}(\boldsymbol{\mathcal{Q}}) = 0$ is sought.

Equation 2.9 is solved using pseudo-transient continuation, which involves time-marching with the implicit Euler method. This requires the solution of, at time-step n,

$$\left(\boldsymbol{\mathcal{T}}^{(n)} + \boldsymbol{\mathcal{A}}^{(n)}\right) \Delta \boldsymbol{\mathcal{Q}}^{(n)} = -\boldsymbol{\mathcal{R}}^{(n)} \tag{2.10}$$

where $\boldsymbol{\mathcal{T}}$ is a diagonal matrix of the inverse of the locally varying time-steps, $\boldsymbol{\mathcal{A}}$ is the flow Jacobian $\frac{\partial \boldsymbol{\mathcal{R}}}{\partial \boldsymbol{\mathcal{Q}}}$, and $\Delta \boldsymbol{\mathcal{Q}}^{(n)} = \boldsymbol{\mathcal{Q}}^{(n+1)} - \boldsymbol{\mathcal{Q}}^{(n)}$ is the solution update. For an infinite time-step, i.e. $\boldsymbol{\mathcal{T}} = \mathbf{0}$, this reduces to Newton's method. Equation 2.10 is solved in two phases: 1) a start-up phase which aims to provide a good starting point for Newton's method, and 2) an inexact-Newton phase which drives the solution to steady-state. The difference between the two phases is the manner in which the time-step is ramped up, how the flow Jacobian is formed, and how accurately the linear problem is solved at each time-step.

In the start-up phase, the local time-step at each node is calculated for each time-step, n, as

$$\Delta t^{(n)} \propto ab^n \tag{2.11}$$

where $a = 10^{-3}$ and $b \in [1.05, 1.10]$ for this work. The time step $\Delta t^{(n)}$ is also a function of the metric Jacobian resulting from the coordinate transformation. In the start-up phase, the flow Jacobian is also replaced by a first-order approximation which: 1) increases the second-difference dissipation and removes the fourth-difference dissipation for the inviscid terms, 2) neglects the cross-derivative terms in the viscous stresses, and 3) the viscosity values in the viscous fluxes are treated as a constant. These simplifications increase the sparsity of the flow-Jacobian.

In the inexact-Newton phase, the time-step is increased towards infinity more quickly via

$$\Delta t^{(n)} \propto \max\left[\alpha \left(\frac{||\boldsymbol{\mathcal{R}}^{(n)}||_2}{||\boldsymbol{\mathcal{R}}^{0}||_2}\right)^{-\beta}, \Delta t^{(n-1)}\right] \tag{2.12}$$

where $\beta = 1.5$ for this work, and

$$\alpha = \Delta t^{(n_{\text{switch}})} \left(\frac{||\boldsymbol{\mathcal{R}}^{(n_{\text{switch}})}||_2}{||\boldsymbol{\mathcal{R}}^0||_2} \right)^{\beta} \tag{2.13}$$

where n_{switch} is the time-step at which the algorithm switches from the start-up to the inexact-Newton phase. In the inexact-Newton phase, no low-order approximation to the flow Jacobian is made, and the full Jacobian can either be computed explicitly (as is required for the gradient evaluation as described in Section 2.4), or since a Krylov subspace method is used for solving the linear problem, for which only Jacobian-vector products are required, these Jacobian-vector products can be approximated via a first-order Frechet derivative based upon the flow residual vector.

For both the start-up and inexact-Newton phases, the linear problem arising at each time-step is solved using the generalized minimum residual (GMRES) method, together with approximate-Schur preconditioning. During the start-up phase the linear problem is solved to a relative tolerance,

$$\eta = \frac{\left|\left|\boldsymbol{\mathcal{R}}^{(n)} + \left(\boldsymbol{\mathcal{T}}^{(n)} + \boldsymbol{\mathcal{A}}^{(n)}\right) \Delta \boldsymbol{\mathcal{Q}}^{(n)}\right|\right|_2}{||\boldsymbol{\mathcal{R}}^{(n)}||_2}, \tag{2.14}$$

of 5×10^{-2}, and this tolerance is tightened to 1×10^{-3} for the inexact phase. For many of the cases considered in this work, the solution of the linear problems in the inexact-Newton phase can be quite difficult, in which case a modified flexible version of the generalized conjugate residual method with inner orthogonalization and outer truncation (GCROT(m, k)) [108] is used to attain sufficient convergence of the linear problem without a prohibitive memory increase. Sample flow solver convergence histories are shown in Figure 2.2 for both a CTW and HWB case, with the location of the transition between the two phases indicated. Details of all the elements of this algorithm can be found in Hicken and Zingg [79] and Osusky and Zingg [82]. The flow solver has been validated through participation in the 5$^{\text{th}}$ AIAA Drag Prediction Workshop [109].

2.3 Gradient-Based Optimization

Numerical optimization strategies can broadly be classified as stochastic or gradient-based methods. Stochastic methods, one of the most popular being genetic algorithms [110], have the advantage that they explore the design space globally and are thus not confined to

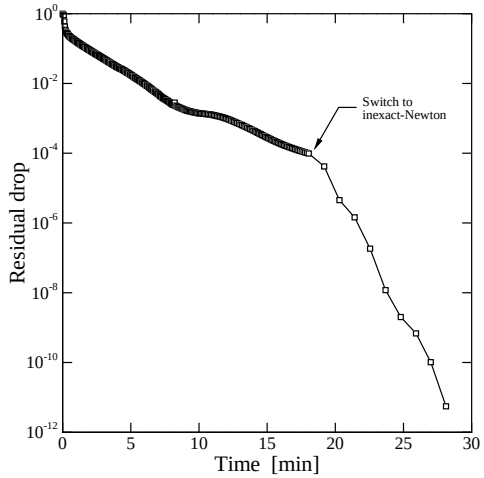

(a) CTW flow solve on a 520-block, 6.3×10^6 node grid

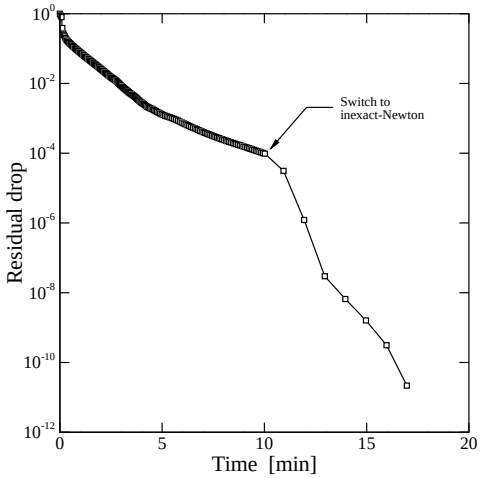

(b) HWB flow solve on a 112-block, 1.5×10^6 node grid

Figure 2.2: Sample flow solve convergence histories for an HWB and CTW case. Symbols indicate nonlinear solver iterations, with the point of transition from the start-up to the inexact-Newton phase indicated. Both solutions are obtained with one block per 2.53GHz Intel Xeon processor, each with 2GB of memory.

finding local optima; however they cannot be guaranteed to find global optima in a finite time either. Secondly, they only require evaluation of the functions of interest, and thus can easily be used with black-box solvers. Gradient-based optimizers may only find locally optimal solutions, and they require computation of all function gradients. For high-fidelity ASO, where the function evaluations are typically very expensive, gradient-based optimizers have the advantage that they typically require far fewer function evaluations then genetic algorithms, as shown by Zingg et al. [111] The issue of convergence to local optima by gradient-based methods has been addressed by Chernukhin and Zingg [92] through the use of hybrid methods and multistart procedures for gradient-based algorithms. Gradient-based methods are used in this thesis due to their lower computational cost.

The third party sequential quadratic programming (SQP) code SNOPT [112] is used in this work. It is designed for large scale optimization problems which are subject to linear

and nonlinear constraints. SNOPT aims to solve the general optimization problem

$$\begin{aligned} \text{minimize} \quad & \mathcal{J} \\ \text{with respect to} \quad & \boldsymbol{X} \\ \text{subject to} \quad & \boldsymbol{L} \leq \begin{pmatrix} \boldsymbol{X} \\ \boldsymbol{AX} \\ \boldsymbol{C}(\boldsymbol{X}) \end{pmatrix} \leq \boldsymbol{U} \end{aligned} \tag{2.15}$$

where $\mathcal{J}$ is the objective, $\boldsymbol{X}$ is the vector of design variables, $\boldsymbol{A}$ is the matrix of coefficients for the linear constraints, $\boldsymbol{C}(\boldsymbol{X})$ is a vector of nonlinear constraints, and $\boldsymbol{L}$, and $\boldsymbol{U}$ are lower and upper bounds for each of the above. For each major iteration[4] of the SQP algorithm, SNOPT generates a new set of design variables which seek to minimize a Lagrangian function of the objective and constraints. At each of these major iterations a quadratic approximation to the Lagrangian, with linearized constraints and a BFGS approximation to the Hessian, is minimized in order to obtain the search direction. A step-size is then determined such that a sufficient decrease in the merit function, the value of the Lagrangian, is attained. This process requires the gradients of the objective and constraints with respect to the design variables. These are computed via the discrete adjoint method as described in the following section.

Three important metrics are useful for analyzing SNOPT convergence and will be referred to throughout this thesis.

Merit function: The merit function is the value of the Lagrangian of the optimization problem, and, when all the constraints are satisfied, reduces to the value of the objective.

Feasibility: Feasibility is a measure of the maximum constraint violation, normalized with the magnitude of the design vector. For all of the studies in this work, all constraints are considered satisfied if the feasibility is below 10^{-4}.

Optimality: Optimality is a measure of the magnitude of the gradient of the linearized Lagrangian. This value should be driven as low as possible; however typically the resulting computational cost required to reach a sufficiently low value is not warranted.

A sample optimization convergence history for a RANS-based optimization of an HWB

[4]Major iterations are the general term used in the optimization literature. As they relate to design optimization, they will typically be referred to as 'design iterations'. They correspond to a new design which has improved performance, i.e. produces a reduced objective function value.

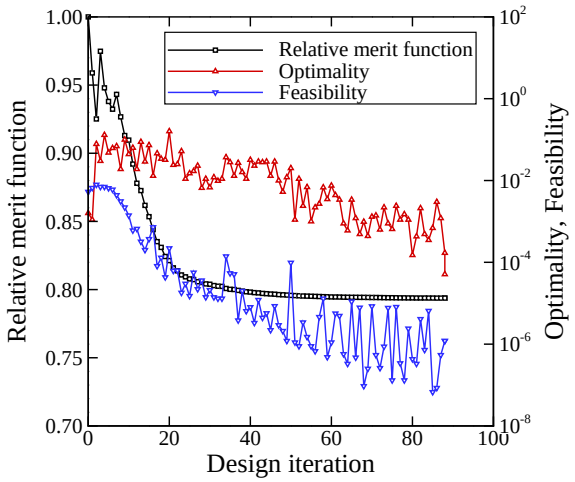

Figure 2.3: A sample optimization problem convergence history.

at transonic speed with 408 design variables is shown in Figure 2.3. Driving the optimality to deep convergence is not achieved in this case. Instead, it can be seen that after about the 40^{th} design iteration there is little change in the merit function; by the 80^{th} iteration the change is imperceptible, and the optimization is thus terminated.

2.4 Gradient Evaluation

For optimization problems constrained by a set of PDEs, as for ASO, the function gradients can be efficiently obtained using the adjoint method as pioneered for ASO by Pironneau [113] and Jameson [114]. For this work, the discrete adjoint method is used. The gradient calculation is explained in detail by Hicken and Zingg [80] and Osusky et al. [84] and summarized here.

First, consider a functional of interest, $\mathcal{F}$, such as the objective or a constraint in the above optimization definition, which is a function of the numerical solution of a PDE. Introducing the Lagrangian function

$$\mathcal{L} = \mathcal{F} + \boldsymbol{\Lambda}^T \boldsymbol{c} \tag{2.16}$$

where $\mathcal{F}$ is the function of interest, $\boldsymbol{\Lambda}$ is a vector of Lagrange multipliers (adjoint variables), and $\boldsymbol{c}$ is a vector of PDE constraints. Here the PDE constraints are the requirement that the governing PDEs have been solved in discrete form, i.e. $\boldsymbol{c} = 0$, where for the current ASO framework, the requirement is that the discrete flow and mesh equations have been solved, i.e. $\boldsymbol{\mathcal{R}}(\boldsymbol{\mathcal{Q}}, \boldsymbol{B}_{N_\text{m}}) = \boldsymbol{0}$ and $\boldsymbol{\mathcal{M}}(\boldsymbol{B}_{m-1}, \boldsymbol{B}_m)_{m=1,\ldots,N_\text{m}} = \boldsymbol{0}$. Thus, the Lagrangian equation

becomes

$$\mathcal{L} = \mathcal{F} + \sum_{m}^{N_\mathrm{m}} \boldsymbol{\lambda}_m^T \boldsymbol{\mathcal{M}}_m + \boldsymbol{\psi}^T \boldsymbol{\mathcal{R}} \tag{2.17}$$

where $\boldsymbol{\lambda}_m$ and $\boldsymbol{\psi}$ are the mesh and flow adjoint variable vectors, respectively. Applying the Karush-Kuhn-Tucker (KKT) conditions to Equation 2.17 yields the following set of equations for the adjoint variables

$$\left(\frac{\partial \boldsymbol{\mathcal{R}}}{\partial \boldsymbol{\mathcal{Q}}}\right)^T \boldsymbol{\psi} = -\left(\frac{\partial \mathcal{F}}{\partial \boldsymbol{\mathcal{Q}}}\right)^T \tag{2.18}$$

$$\left(\frac{\partial \boldsymbol{\mathcal{M}}_{N_\mathrm{m}}}{\partial \boldsymbol{B}_{N_\mathrm{m}}}\right)^T \boldsymbol{\lambda}_{N_\mathrm{m}} = -\left(\frac{\partial \mathcal{F}}{\partial \boldsymbol{B}_{N_\mathrm{m}}}\right)^T - \left(\frac{\partial \boldsymbol{\mathcal{R}}}{\partial \boldsymbol{B}_{N_\mathrm{m}}}\right)^T \boldsymbol{\psi} \tag{2.19}$$

$$\left(\frac{\partial \boldsymbol{\mathcal{M}}_m}{\partial \boldsymbol{B}_m}\right)^T \boldsymbol{\lambda}_m = -\left(\frac{\partial \boldsymbol{\mathcal{M}}_{m+1}}{\partial \boldsymbol{B}_m}\right)^T \boldsymbol{\psi}_{m+1} \qquad m = N_\mathrm{m} - 1, \ldots, 1 \tag{2.20}$$

which are solved in the order shown. The left-hand side of Equation 2.18 is simply the transpose of the flow Jacobian and is solved using GCROT(m, k). In contrast to the linear systems of the flow solution, this linear problem must be solved to a tight tolerance, typically 10^{-10}, thus necessitating the restarting algorithm in order to conserve memory. The mesh adjoint equations, Equations 2.19 and 2.20, are solved using the same preconditioned conjugate gradient solver, and to the same tolerance, as for the mesh movement equations. Most of the terms in the Jacobians that appear in Equations 2.18-2.20 are calculated analytically; however some, such as the SAT terms and $\frac{\partial \boldsymbol{\mathcal{M}}_{m+1}}{\partial \boldsymbol{B}_m}$, are calculated using the complex-step method, as analytical differentiation is complicated and both these terms are inexpensive to compute using the complex-step method. The full gradient of the Lagrangian with respect to the design variables, $\boldsymbol{X}$, is then computed as

$$\mathcal{G} = \frac{\partial \mathcal{L}}{\partial \boldsymbol{X}} = \frac{\partial \mathcal{F}}{\partial \boldsymbol{X}} + \sum_{m=1}^{N_\mathrm{m}} \lambda_m^T \frac{\partial \boldsymbol{\mathcal{M}}_m}{\partial \boldsymbol{X}} + \psi^T \frac{\partial \boldsymbol{\mathcal{R}}}{\partial \boldsymbol{X}} \tag{2.21}$$

The above process must be repeated for each different functional of interest, including the objective, $\mathcal{J}$, and any constraints in $\boldsymbol{C}$ which depend on the flow or mesh equations. For problems with design variables other then geometric, such as angle-of-attack or Mach number, the corresponding terms in $\frac{d\boldsymbol{\mathcal{R}}}{d\boldsymbol{X}}$, such as $\frac{d\boldsymbol{\mathcal{R}}}{d\alpha}$ or $\frac{d\boldsymbol{\mathcal{R}}}{dM}$, are calculated using the complex-step method. In practice, terms with respect to the geometric design variables in Equation 2.21 are actually computed as $\frac{\partial \mathcal{L}}{\partial \boldsymbol{B}}$, and the gradient with respect to the geometric design variables,

such as the region variables discussed previously, are computed via the chain rule as

$$\mathcal{G} = \frac{\partial \mathcal{L}}{\partial \boldsymbol{X}} = \frac{\partial \mathcal{L}}{\partial \boldsymbol{B}} \frac{\partial \boldsymbol{B}}{\partial \boldsymbol{X}} \tag{2.22}$$

Chapter 3

Design Problem

The following four classes of aircraft are considered, with the aircraft used to define the associated reference mission in parentheses:

1. 100-passenger regional jet transport (Embraer E190 [115])
2. 160-passenger narrow-body transport (Boeing 737-800 [116])
3. 220-passenger mid-size transport (Boeing 767-200ER [117])
4. 300-passenger wide-body transport (Boeing 777-200LR [118])

For each class, CTW and HWB designs are created using a low-fidelity conceptual design tool that incorporates aerodynamic and weight-and-balance analyses using the methods of Torenbeek [119], Kroo [120], and Raymer [15]. For the HWB designs, the weight of the center-body structure is obtained using the method of Bradley [121]. The methods used to obtain the remaining structure, systems, fuel, and operational item weights for the HWB are the same as those used for the CTW aircraft. The same low-fidelity aerodynamic models are used for both aircraft, with the HWB being treated as a wing. This weight estimation methodology has been evaluated for a series of CTW designs against publicly available data, and for HWB aircraft against the results of Nickol [70]. For this work, all estimates are based on technology levels similar to those of the reference aircraft, e.g. existing engines, primarily aluminum construction, no active flow control, etc. Further details of this conceptual design framework can be found in Appendix A.

Since most aircraft are not typically operated at their maximum range and/or payload condition for most missions, this study will examine their use for a nominal mission. The nominal mission for the regional jet is chosen to be a 500 nmi route with a full passenger payload of 100 PAX. The narrow-body nominal mission is a 1,000 nmi route with a full passenger

payload of 160 PAX. The mid-size transport nominal mission is a 3,000 nmi mission with full passenger payload, 220 PAX, with an additional 12,800 lb of revenue cargo, corresponding to 50% utilization. Finally, for the wide-body, a 6,000 nmi nominal mission with full, 300 PAX, passenger payload and 50% revenue cargo of 37,500 lb is used. The nominal cruise speeds are Mach 0.78, 0.79, 0.80, and 0.84, respectively, which are chosen to represent typical cruise speeds for the reference aircraft. All designs are chosen to have an initial cruise altitude (ICA) of 36,000 ft for the nominal mission, which is within a typical range for the reference aircraft. The same altitude is used for all classes, and for both the CTW and HWB designs, to allow for comparison at the same conditions. The optimal cruise altitude is dependent on wing loading, engine performance, buffet, etc., and can thus vary between classes. The effect of cruise altitude is examined in Chapter 6.

Each aircraft is sized for its design mission, i.e. the range and payload combinations on the envelope of the payload-range diagram for the reference aircraft. These models are then used to estimate the aircraft weights and CG location at the beginning of the nominal mission cruise, which serves as the operating point for the high-fidelity optimization.

All of the designs presented in this chapter are used as the starting point for the high-fidelity ASO presented in Chapter 4, upon which all performance comparisons will be made. Both the CTWs and HWBs will be optimized in the same manner, subject to the same variables, constraints, and assumptions, which will allow a direct performance comparison between the performance of the two concepts. CTWs are created, and later optimized, for the regional, narrow-body, and wide-body classes. No CTW is explored for the mid-size case. The choice to exclude the mid-size CTW is based on the fact that the other classes provide more relevant information. The regional and narrow-body class HWBs have not been thoroughly studied in the literature, and thus having performance comparisons for these cases is important. The wide-body represents the other end of the size spectrum, and it is included to investigate the scaling of both the CTW and HWB performance with aircraft size. The mid-size HWB is included to help establish the trend of optimal HWB shape with size, as will be discussed in Chapter 5.

3.1 Conventional Tube-and-Wing Designs

CTW designs are created to reflect the reference aircraft in each class, as listed previously. Each CTW uses the same engines as the reference aircraft. The low-fidelity models are shown in Figure 3.1 with basic design information given in Table 3.1, and the conditions at the start of the nominal mission are summarized in Table 3.2.

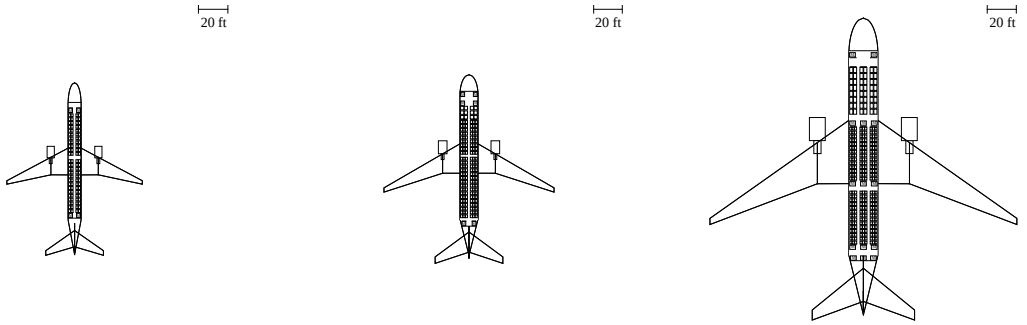

(a) CTW100 (b) CTW160 (c) CTW300

Figure 3.1: Planforms for each of the baseline designs.

Table 3.1: Baseline CTW design information.

Design	PAX	Gate	Span [ft]	Bending span [ft]	Reference area [ft^2]	Aspect ratio [–]	MAC [ft]	Max range [nmi]	Max payload [lb]	OEW [lb]	MTOW [lb]
CTW100	100	C	94	85	1,000	8.9	13.1	2,900	28,400	59,200	105,800
CTW160	160	C	118	105	1,350	10.3	14.3	3,700	47,000	88,100	173,900
CTW300	300	E	213	193	4,990	9.1	30.3	9,500	141,000	330,900	775,500

Table 3.2: Baseline CTW design information at the start of the nominal mission.

Design	Range [nmi]	ICA [ft]	Mach [–]	Payload [lb]	Weight[3] [lb]
CTW100	500	36,000	0.78	22,000[1]	91,500
CTW160	1,000	36,000	0.79	35,200[1]	143,300
CTW300	6,000	36,000	0.84	103,500[2]	633,900

[1] Full passenger payload (@ 220 lb/PAX)
[2] Full passenger payload plus 50% revenue cargo
[3] At the start of cruise

3.2 Hybrid Wing-Body Designs

For each class of aircraft, an HWB is created to reflect shapes typically seen in the literature. The determination of an appropriate span is, however, not obvious. For each class of HWB, two designs with different spans are considered, with the exception of the narrow-body class. For the first set of designs, the span is selected such that the HWB fits inside the same gate as the equivalent CTW. The exception to this is the narrow-body class HWB. Since the CTW160 has a span that is already at the code 'C' gate limit and the creation of a narrow-body class HWB with this span results in exceptionally short wings, this case is not considered. Thus, three HWBs for the remaining classes are designed. These are referred to as the HWB100C with a 118 ft span, the HWB220D with a span of 170 ft, and the HWB300E with a 213 ft span. For all of the HWBs in this work, the letter suffix indicates the gate within which a design resides.

Due to the span loading provided by the broad center-body, larger spans are possible for the HWBs. Wing weight scales strongly with span, and while there are of course other considerations, such as sweep, wing area, high-lift devices, thickness, etc., which affect the wing weight, span is a dominant factor. Thus, the concept of the 'bending span' is introduced. This is taken as the portion of the span which is primarily subjected to bending loads. For the CTW aircraft, this is taken as $b_{\text{bend}} = b - D_{\text{fuse}}$, where b is the total span, and D_{fuse} is the fuselage diameter. For HWB aircraft, the bending span is taken as the span of the wing in isolation and is defined as $b_{\text{bend}} = b - w_{\text{cb}}$, where w_{cb} is the width of the center-body. In this work, the bending span will be used to determine an appropriate span by serving as a low-order surrogate for wing weight. The assumption is then made that an HWB could feasibly be created which has a bending span equivalent to that of a similarly sized CTW. This is a conservative assumption for HWB wings since it does not account for the load relief provided by the increased lift carried by the center-body. This bending span is used

to create larger span versions of the regional, narrow-body, mid-size, and wide-body class HWBs by choosing the spans such that the bending spans are close to those of the equivalent CTWs. If this results in a span coming close to a gate limit, the gate limit value is used since this is a more well defined rationale for the span than the bending span argument. For the regional-class HWB, a 130 ft span design, referred to as the HWB100D, is created which has a bending span similar to that of the CTW100. For the narrow-body, mid-size and wide-body class HWBs, spans are chosen which are at the gate limit of the next gate class; the HWB160D, HWB220E, and HWB300F designs are created with 170 ft, 213 ft, and 262 ft spans, respectively. For these three classes, the equivalent bending span argument yields spans that are close to gate limits, and the spans shown above are thus chosen so that each design resides at a gate limit. This results in bending spans that are within 5% of those of the equivalent CTWs. The above procedure results in each HWB design requiring a gate one size larger than its CTW counterpart, while having similar bending spans. For each class, the spans selected are in line with those seen in the literature. For example, Boeing's OREIO concept, which is similar to the HWB220E here, has a 213 ft span [66]. Boeing's SUGAR Ray, which is similar to the HWB160D, has a span of 168.5 ft [5]. MIT's SAX-40 design, for 215 passengers, and thus similar to the HWB220E, has a span of 221.6 ft. In contrast with Boeing's designs, the SAX-40 does not reside in the code 'E' gate.[1] The N2A, a Boeing derivative of the SAX-40 with maximum payload of 103,000 lb (between the HWB220 and HWB300) has a span of 213 ft [122].

Low-fidelity models are created for each design and are shown in Figure 3.2 with basic design information given in Table 3.3. The conditions at the start of the nominal mission are summarized in Table 3.4.

The interior cabin height for each class is 79 inches. This is the same as the interior height of the regional-class CTW, but smaller than that of the narrow-body, mid-size, and wide-body CTWs. While the cabin height of a CTW is intrinsically linked to the cabin width due to the cylindrical fuselage, this is not the case for HWBs and the cabin height can be chosen independently. For this work, all of the HWB cabin heights are selected to adequately accommodate an adult standing in the aisles. However, consideration would have to be given to passenger comfort, and the cabin height may need to be increased for large capacity, long range aircraft.

The regional and narrow-body-class HWBs have the cargo located outboard of the passenger cabin, while the other two classes have under-floor cargo.

[1] Earlier iterations of the SAX family respected the code 'E' gate limits.

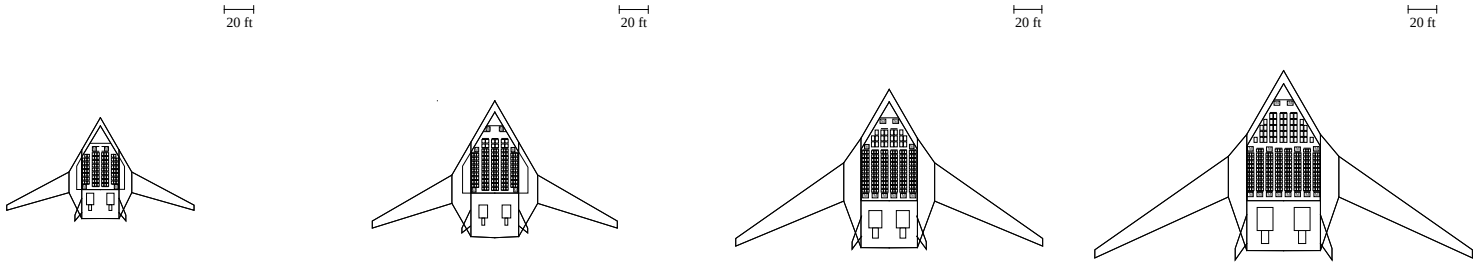

(a) HWB100D (b) HWB160D (c) HWB220E (d) HWB300F

Figure 3.2: Planforms for each of the baseline designs.

Table 3.3: Baseline HWB design information.

Design	PAX	Gate	Span [ft]	Bending span [ft]	Reference area [ft^2]	Wing aspect ratio [–]	MAC [ft]	Max range [nmi]	Max payload [lb]	OEW [lb]	MTOW [lb]
HWB100C	100	C	118	76	2,730	8.3	42.4	2,900	28,400	70,200	117,700
HWB100D	100	D	130	88	2,840	9.7	41.1	2,900	28,400	73,500	121,200
HWB160D	160	D	170	110	5,140	9.0	55.9	3,700	47,000	126,300	217,300
HWB220D	220	D	170	107	6,560	6.7	67.1	8,000	78,400	192,700	411,300
HWB220E	220	E	213	150	7,260	9.4	62.5	8,000	78,400	221,200	432,600
HWB300E	300	E	213	136	8,950	8.1	75.4	9,500	141,000	350,200	768,500
HWB300F	300	F	262	185	9,780	11.0	70.7	9,500	141,000	417,000	826,800

Table 3.4: Baseline HWB design information at the start of the nominal mission.

Design	Range [nmi]	ICA [ft]	Mach [–]	Payload [lb]	Weight[3] [lb]
HWB100C	500	36,000	0.78	22,000[1]	103,100
HWB100D	500	36,000	0.78	22,000[1]	106,600
HWB160D	1,000	36,000	0.79	35,200[1]	185,300
HWB220D	3,000	36,000	0.80	61,200[2]	328,000
HWB220E	3,000	36,000	0.80	61,200[2]	355,400
HWB300E	6,000	36,000	0.84	103,500[2]	638,000
HWB300F	6,000	36,000	0.84	103,500[2]	700,500

[1] Full passenger payload (@ 220 lb/PAX)
[2] Full passenger payload plus 50% revenue cargo
[3] At the start of cruise

The assumption is made that the HWB designs will require some form of lateral stabilizer. It is assumed that two vertical stabilizers, or fins, outboard of the engines will be used so as to also provide noise shielding. These stabilizers are sized such that they have sufficient area to counteract a one-engine-inoperative yawing moment, given the same fin lift coefficient as the baseline conventional aircraft, i.e.

$$S_{F_{\text{HWB}}} = \frac{1}{2}\left(\frac{y_E}{x_F}\right)_{\text{HWB}}\left(\frac{x_F}{y_E}\right)_{\text{CTW}} S_{F_{\text{CTW}}} \tag{3.1}$$

where S_F is the fin area, y_E is the lateral offset of the engines from the centerline, x_F is the distance between the fin MAC quarter chord and the CG. The 1/2 factor arises from the fact that the HWBs have two fins.

The same engines are used for the HWBs as for the CTWs, where simple pylon mounting is assumed such that the HWB receive no credit for advanced engine installation, such as boundary layer ingestion.

Chapter 4

Aerodynamic Shape Optimization Studies

This chapter describes the use of high-fidelity aerodynamic shape optimization based on the RANS equations in the aerodynamic design of both the CTW and HWB aircraft presented in the preceding chapter. The methods used to choose the mission profiles and to develop the baseline designs in the previous chapter are low-fidelity and do not represent full system-optimal design or operation. Instead, they are meant only to serve as a reasonable starting point for the high-fidelity optimization. All performance comparisons are made based on the high-fidelity optimized designs presented in this, and subsequent, chapters.

4.1 Three Dimensional Models and Grids

Based on the designs presented in Chapter 3, full three-dimensional surface models are created using the geometry toolbox developed by Gagnon and Zingg [93]. The baseline CTW wings are untwisted and use the SC(2)-0012 section at the root and crank, and the SC(2)-0010 at the tip. The baseline HWB bodies use SC(2)-0014 sections, with SC(2)-0012 and SC(2)-0010 sections at the wing root and tip, respectively. Since the initial center-body airfoils are not designed specifically for HWB use, in order to maintain sufficient thickness up to 70% chord to house the cabin, a 14% thick section is used on the center-body. This is an inefficient packing of the cabin within this section, so the optimizer will be used to design a more appropriate section that has a lower maximum thickness-to-chord ratio, which is maintained over a larger fraction of the chord.

The vertical stabilizers, nacelles, and pylons are not included in the three-dimensional models. The vertical stabilizers are not included as they are sized by conditions other than

cruise, which are not included in the high-fidelity optimization. Their drag contribution is accounted for post-optimization by one of two methods: 1) for the regional-class aircraft, upon which most of the detailed studies are based, three-dimensional models of the fins are created and analyzed with the high-fidelity solver in isolation; 2) to reduce cost for the remaining classes, the Mach number corrected version of the Prandtl-Schlichting [15] skin friction equation is used to estimate the skin friction drag coefficient of the vertical stabilizers. As noted by Raymer [15], form drag is typically a constant fraction of the skin friction drag, and it is typically accounted for with "form factors" applied to the skin friction coefficient. The high-fidelity analysis of the regional-class fins, with their different geometries and Reynolds numbers, support this conclusion, and it was found that the ratio of form drag to skin friction drag was between 0.21 and 0.23, resulting in form factors between 1.21 and 1.23. Interference drag between the fins and fuselage/center-body is neglected, as it is typically a small fraction of the profile drag of the fins [15,119], and will be present for both configurations studied. While there will be differences in the fin interference drag magnitude for the two configurations due to different installations, it is postulated that, due to the relatively small contribution of interference drag to total drag, comparison between the two concepts can still be made.[1]

The presence of nacelles and pylons potentially affects the performance of the two configurations differently. For the CTWs, the presence of the nacelles and pylons can affect the spanwise lift distribution, potentially resulting in degraded performance. For the HWBs, there are multiple installation options, such as pylon mounted engines, or boundary layer ingesting engines, both of which are mounted on the upper surface of the center-body. In this work, boundary layer ingestion is considered an advanced technology, and pylon mounted engines are assumed. While challenging, upper surface installation can provide performance benefits, as suggested by Hooker [123]. In light of this, while engine installation is neglected in the high-fidelity optimization, this is a conservative assumption due to the potential benefits for the HWB. Neglecting the vertical stabilizers, nacelles, and pylons also greatly simplifies gridding.

For RANS-based optimization problems with free wing area, it is important that the ratio of induced and friction drag be predicted accurately such that the optimizer can prop-

[1]For the CTW100-1 presented below, the parasitic drag of the fin is 4.6% of the total drag, and via Raymer [15] the interference drag is likely about 0.19% of the total drag. The fin parasitic drag for the HWB100D-1 is 5.1% of the total drag. Assuming the same interference factor for the two configurations, the fin interference drag for the HWB100D-1 is about 0.21% of the total drag. If the HWB's interference factor is twice that of the CTW, the interference drag accounts for 0.41% of the total drag, and the relative total drag of the two configurations changes by 0.2%.

erly trade friction drag for induced drag by changing the wing area. A grid study is conducted to ensure that the grids used for optimization accurately predict this ratio. First, trim-constrained drag minimization is performed on the HWB100C subject to the problem formulation described in the next section, but with only section and twist variables active, resulting in what will be referred to as the HWB100C-0 design. This allows the optimizer to remove shocks, and hence the wave drag contribution to pressure drag.

A grid convergence study is then performed on the resulting geometry, with the grid convergence behavior shown in Figure 4.1 for grids with 764,000 to 11×10^6 nodes. The grid-converged values, represented by the horizontal dashed lines, are obtained using Richardson extrapolation [124] with an order of accuracy of two. The grid-converged friction/pressure drag ratio, C_{D_f}/C_{D_p}, is 1.20, and the grid with 1.5×10^6 nodes yields the same ratio. Thus the grid with 1.5×10^6 nodes, indicated in Figure 4.1, is used for the optimizations. The CTW grids are then created with the same surface resolution; which yields grids with 6.3×10^6 nodes. The local grid distributions are based on the results of studies examining the effects of local refinement on numerical error. The results of these studies are largely in-line with the guidelines of the AIAA Drag Prediction Workshops [125]. The optimization level grids have off-wall spacings of $y^+ \approx 1.0$, leading and trailing edge spacings of $\approx 0.15\%$ chord, and HWB root and tip spacings of $\approx 0.5\%$ and $\approx 0.02\%$ semi-span, respectively, which are refined for the CTWs at the wing-body and tail-body junctions. While these grids are too coarse to provide accurate force and moment estimates, it has been found that they are capable of capturing the dominant flow features and thus properly designing the shape [92,126].

All of the optimizations are conducted on the grid levels found through the above process. To determine the final force and moment coefficients of the optimized designs, grid convergence studies are performed for each optimized design as was done above for the HWB100D-0. For each design, a sequence of two additional grids with 2, and 4 times as many nodes as the optimization grid is created, and Richardson extrapolation is used with an assumed order of accuracy of two to determine the grid-converged performance estimates. For the regional-class designs, an additional grid level is added to the sequence to improve accuracy to allow for comparisons between designs with very similar performance. Unless otherwise stated, all the performance results presented in the remainder of this work

- are Richardson extrapolated estimates for grid-converged performance
- include the parasitic drag contribution from the vertical stabilizers

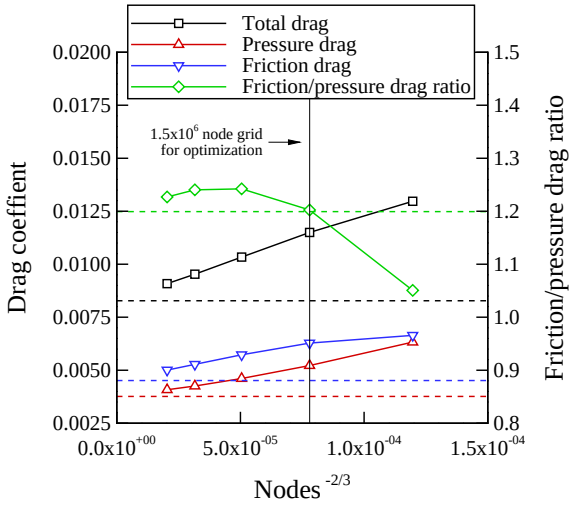

Figure 4.1: Grid refinement study on the HWB100C-0 design which has been optimized to be shock-free. The dashed horizontal lines indicate the Richardson extrapolated values.

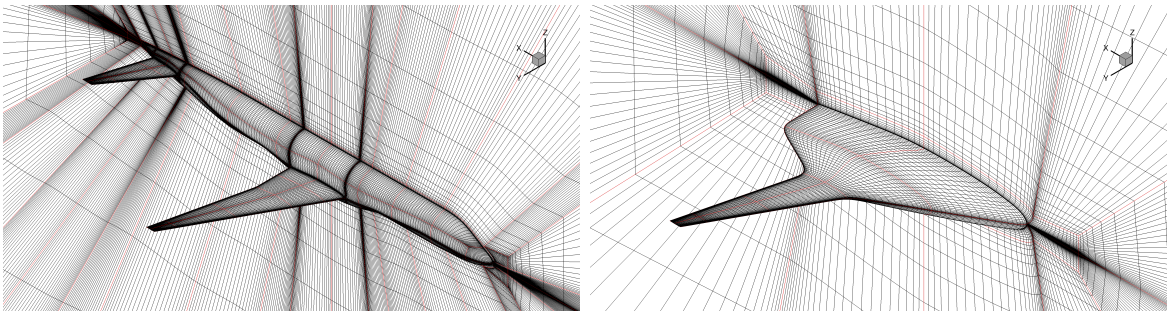

(a) CTW100 (b) HWB100C

Figure 4.2: CFD grids for the CTW100 and HWB100C baselines. (Not shown to the same scale.)

4.2 Optimization Problem Definition

High-fidelity aerodynamic shape optimization is performed at conditions that correspond to the start of the cruise segment of the nominal missions. The starting geometries, which have untwisted wings and use symmetric sections, are initially infeasible and have poor performance. The objective of the optimization is to minimize drag subject to lift and pitching moment constraints, in addition to geometric constraints described below. This work investigates aerodynamically optimal configurations that offer minimum drag for each class of aircraft. Naturally, aircraft design is also driven by additional considerations which need to be taken into account during design. The impact of design changes made by the optimizer

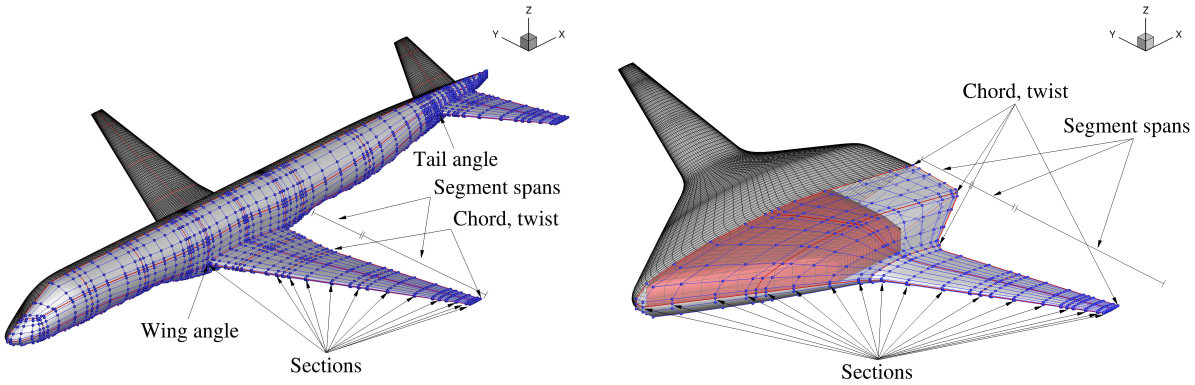

(a) CTW design variables (b) HWB design variables

Figure 4.3: Surface geometries for the regional CTW and HWB baselines showing both the surface CFD mesh and control mesh along with the types and locations of the geometric design variables. The upper surface of the HWB body is translucent to reveal the polyhedron that encloses the cabin. (Not shown to the same scale.)

on structural weight, aeroelastic behaviour, flight dynamics, etc. are not modelled. Rather, since aerodynamic performance is tightly coupled to other disciplines, the optimization problem design variables and constraints are constructed so as to limit geometric changes which have a significant impact on other disciplines, while allowing enough freedom to achieve aerodynamically optimal designs. The following description applies to the optimization for each class.

The surface CFD grid and the geometry parameterization are shown in Figure 4.3. The background surface shows the CFD grid, while the foreground surface shows the B-spline control grid, and the locations of the different geometric design variables are indicated. The design variable definition is that described in Section 2.1.3. The specific design variables and constraints are summarized in Table 4.1 and described below. A portion of the HWB's body upper surface is transparent to show the cabin shape.

The angle-of-attack is a design variable for both configurations and is limited to $\pm 3^\circ$ due to deck angle requirements. The incidence angle of the CTW wing and tail are free to vary between $\pm 5^\circ$. The CTW wing is divided into two segments, one inboard and one outboard of the crank. The HWB consists of three segments, one over the cabin, one transition segment between the edge of the cabin and the wing root, and one for the wing. The span of each of these segments can vary, but the total span remains fixed. The quarter-chord sweep angles of the CTW wing and the HWB wing are fixed. The sweep angle of the transition region of the HWB, between the cabin and the wing, is free to vary such that the optimizer can position the wing to minimize trim drag. For the CTW, the wing chord and twist are allowed to vary

Table 4.1: Design variables and constraints. Bounds given as percentages are deviations from the initial values. Numbers in parentheses are the number of each type of variable/constraint.

	CTW			HWB		
Variables	$-3° \leq$	AoA (1)	$\leq +3°$	$-3° \leq$	AoA (1)	$\leq +3°$
	$-5° \leq$	Wing angle (1)	$\leq +5°$			
	$-5° \leq$	Tail angle (1)	$\leq +5°$			
	$-75\% \leq$	Segment span (2)	$\leq +75\%$	$-75\% \leq$	Segment span (3)	$\leq +75\%$
				$0° \leq$	Transition region sweep (1)	$\leq 85°$
	$-50\% \leq$	Chord (2)	$\leq +50\%$	$-50\% \leq$	Chord (4)	$\leq +50\%$
	$-10° \leq$	Twist (2)	$\leq +10°$	$-10° \leq$	Twist (3)	$\leq +10°$
	$-200\% \leq$	Section shape[1](264)	$\leq +200\%$	$-200\% \leq$	Section shape[1](396)	$\leq +200\%$
	Total effective design variables: 273			Total effective design variables: 408		
Constraints	$-20\% \leq$	t/c (132)	$\leq +50\%$	$-20\% \leq$	t/c (198)	$\leq +50\%$
	$1.25V_{\text{fuel}} \leq$	V_{wing} (1)		$1.25V_{\text{fuel}} \leq$	V_{wing} (1)	
	$-0\% \leq$	Span (1)	$\leq +0\%$	$-0\% \leq$	Span (1)	$\leq +0\%$
	$-0\% \leq$	Wing sweep (2)	$\leq +0\%$	$-0\% \leq$	Wing sweep (1)	$\leq +0\%$
					Cabin shape (2050)	
		$L = W$ (1)			$L = W$ (1)	
		$C_M = 0$ (1)			$C_M = 0$ (1)	

[1] The amount by which the control points defining the sections can move normal to the chordline, as a percentage of their initial distance from the chordline.

at the crank and tip, with linear variation between. For the HWB, the chord is variable at the centerline, and the chord and twist are variable at the outboard edge of the cabin, wing root, and tip, with linear variation between. The CTW and HWB have section control at 12 and 18 span-stations respectively, at each of which there are 22 section variables, 11 for each of the lower and upper surfaces. For each pair of lower and upper surface section shape variables there is a corresponding thickness constraint to prevent the thickness decreasing by more than 20% of the initial value. For the CTW, geometric changes to the fuselage caused by changes of the wing/tail root are handled via the method described in Section 2.1.3. The volume of both the CTW and HWB wings is constrained such that sufficient volume exists in the wings for fuel, with the required volume being taken from the low-fidelity sizing result, which gives 30,000 lb, 46,500 lb, 161,000 lb, and 305,000 lb of fuel for each class, respectively. It is assumed that 80% of the outer mold line volume is usable for fuel tanks. The outer mold line of the HWB is constrained such that it does not violate the fixed HWB cabin shape, shown in Figure 4.3(b).

Lift is constrained to be equal to the weight at the start of cruise, and the pitching moment about the center of gravity must be zero. There are a total of 273 effective design variables for the CTW, and 408 for the HWB. The lift target is not updated during the optimization in response to geometric changes. While changes to weight during the optimization could be captured using the relations used for initial sizing, which are primarily functions of geometry, this is not done due to uncertainties in the accuracy of these equa-

tions. These inaccuracies could be exploited by the optimizer to lighten the aircraft in a way which is unrealistic. The aim is to avoid contaminating the high-fidelity optimization with low-fidelity approximations which can be exploited by the optimizer. As a check, after each optimization, new low-fidelity models are built to reflect any geometric changes, and the resulting changes in OEW are typically less than 2%.

4.3 CTW Optimization

This section presents the results of the CTW optimizations, which are shown in Figures 4.4-4.6. The optimized designs are referred to by the suffix '-1'. As can be seen from the sectional pressure profiles[2], all designs are shock free. While each design started with symmetric sections, the sectional cuts show that the optimizer has found supercritical designs, which are most pronounced for the CTW300-1, which has the highest Mach number. The spanwise lift distributions are nearly elliptical on the outboard portion of the wing, but deviate from the ideal distribution inboard, likely due to the presence of the fuselage. For each class, the maximum section thickness goes to its lower bound along most of the span, with the exception of the wing root. Except for the CTW300-1, which increases the wing area by increasing the tip chord, the wing volumes also go to their lower bound. The CTW300-1 adds the maximum 10° of washout at the tip. These are the only geometric constraints that are active at the optimum. The angle-of-attack for each class goes to its upper bound of 3.0°.

The lift contribution of the fuselage, wing, and tail are shown in Table 4.2. For each class, the fuselage carries between 11.8% and 13.5% of the total lift, and the tail is negatively loaded with between −9.2% and −4.5% of the total lift. The wing produces a nose-down moment which is largely counteracted by the tail, as expected, with some contribution from the fuselage.

The performance of each design is shown in Table 4.3. The lift-to-drag ratios increase with aircraft size as expected due to the increasing wetted aspect ratios. The lift-to-drag ratios are close to what would be expected for modern CTW aircraft, but slightly higher, since nacelle and excrescence drag are not considered, and these designs are point-optimized for this condition. These numbers will form the basis for performance comparisons with the HWBs in the remainder of this thesis.

[2]The small pressure discontinuities seen at the mid-chords are due to the presence of a block boundary and the use of simultaneous approximation terms for the interface conditions. The pressure distribution is shown on the optimization level grid. As the grid spacing at the interface is refined, the magnitude of the discontinuity decreases.

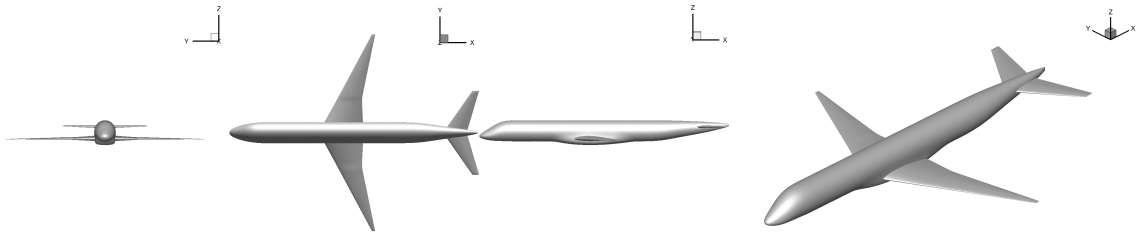

(a) Optimized geometry

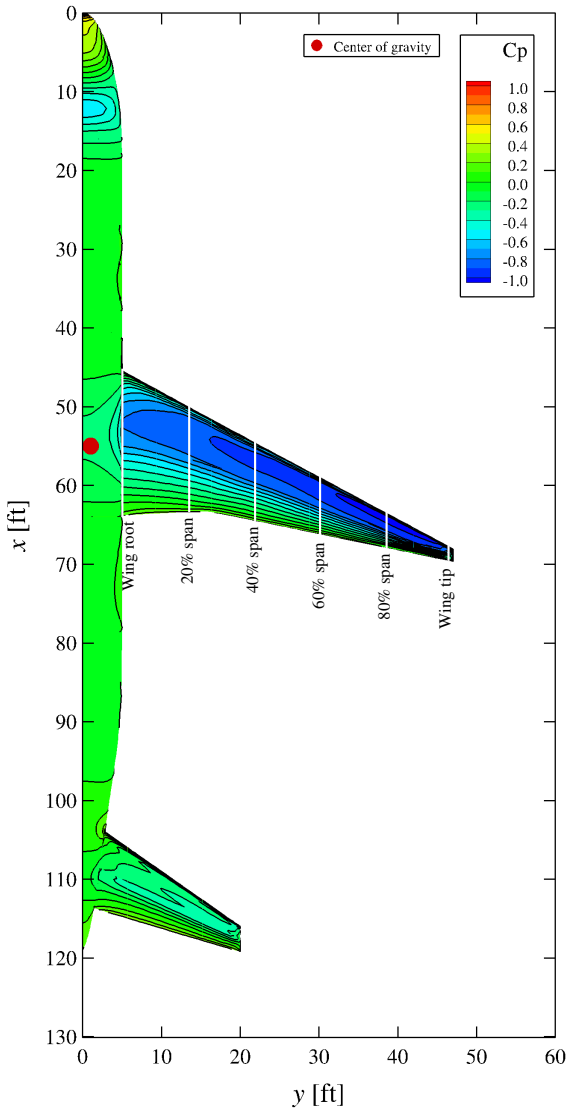

(b) Surface pressure distribution

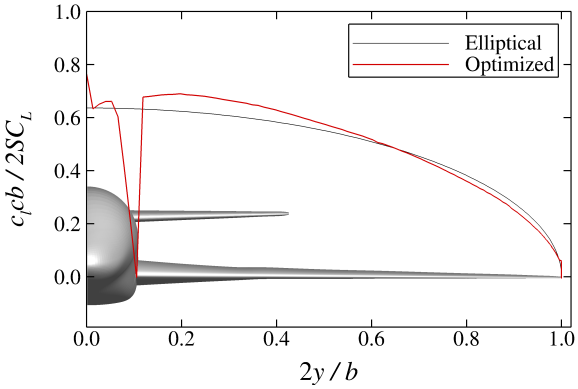

(c) Spanwise lift distribution

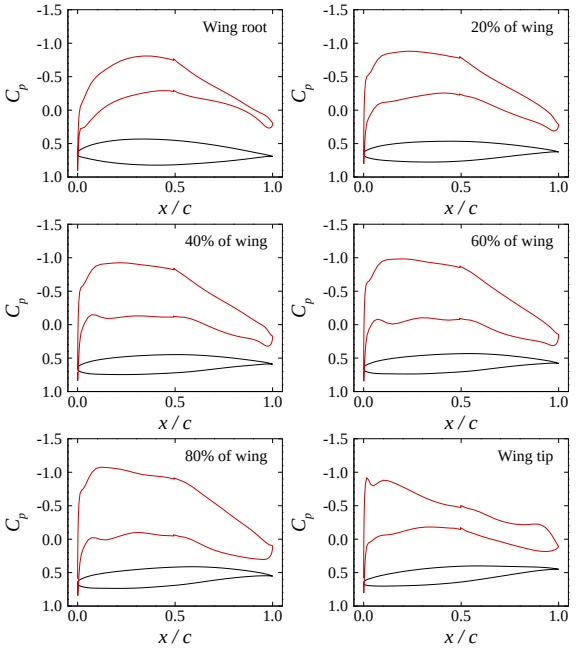

(d) Sectional pressure distributions

Figure 4.4: The optimized CTW100-1 design.

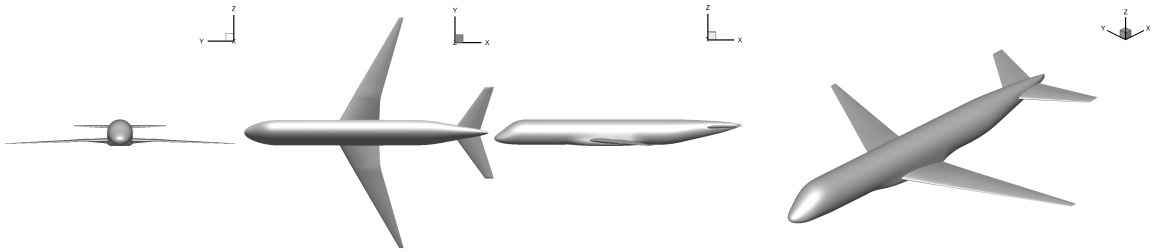

(a) Optimized geometry

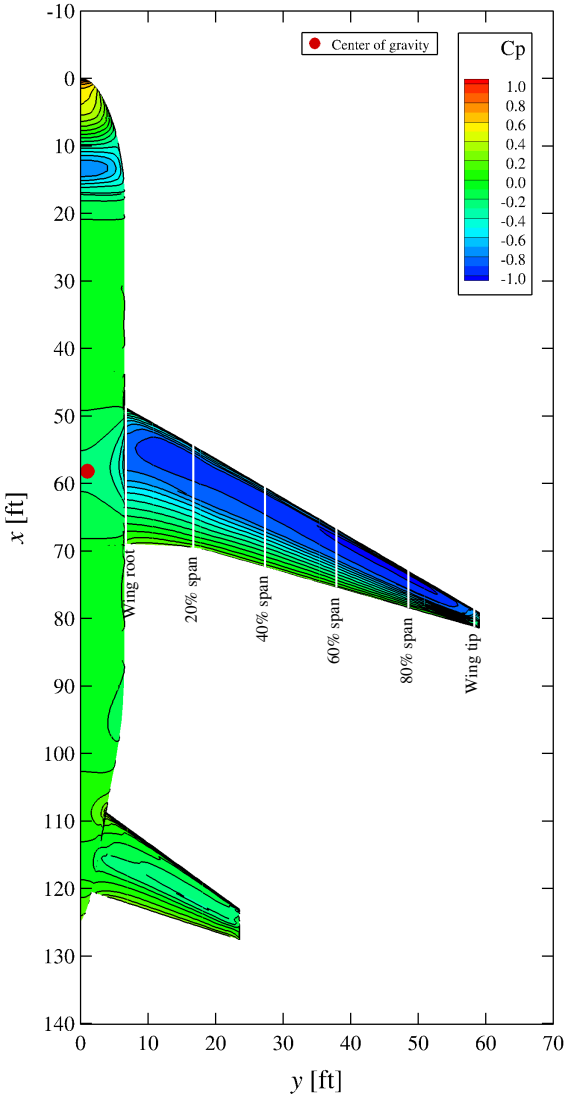

(b) Surface pressure distribution

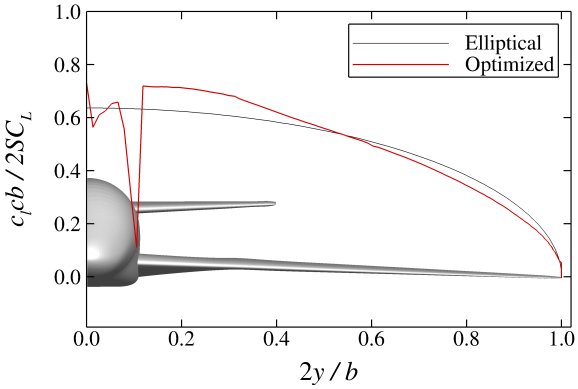

(c) Spanwise lift distribution

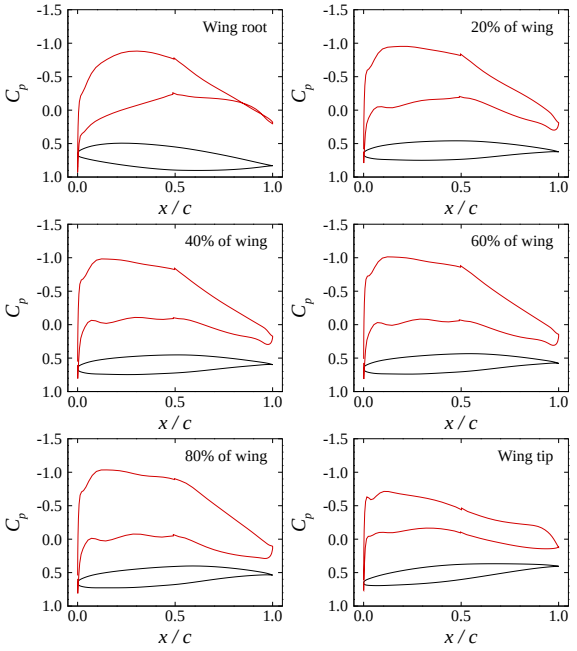

(d) Sectional pressure distributions

Figure 4.5: The optimized CTW160-1 design.

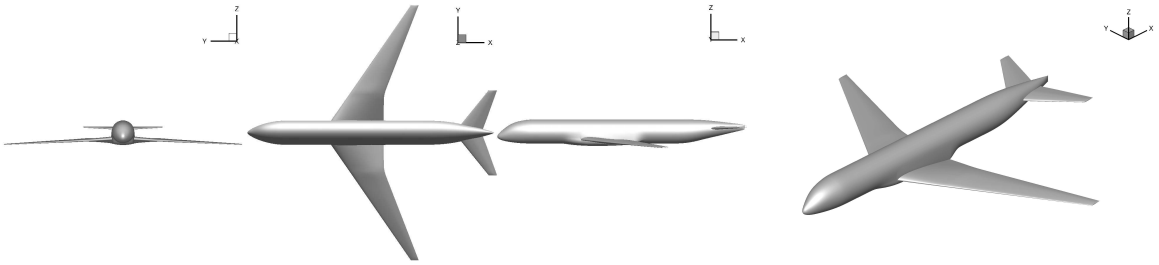

(a) Optimized geometry

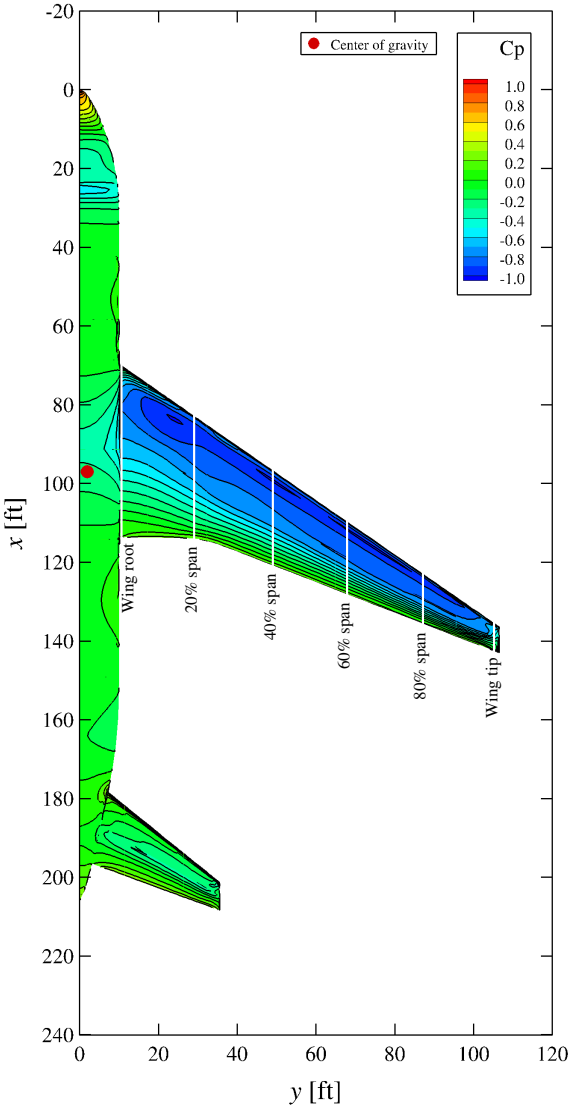

(b) Surface pressure distribution

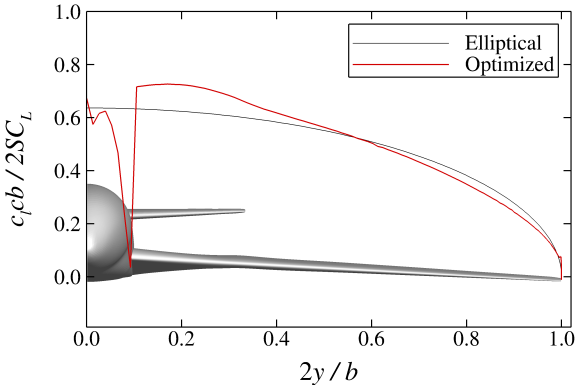

(c) Spanwise lift distribution

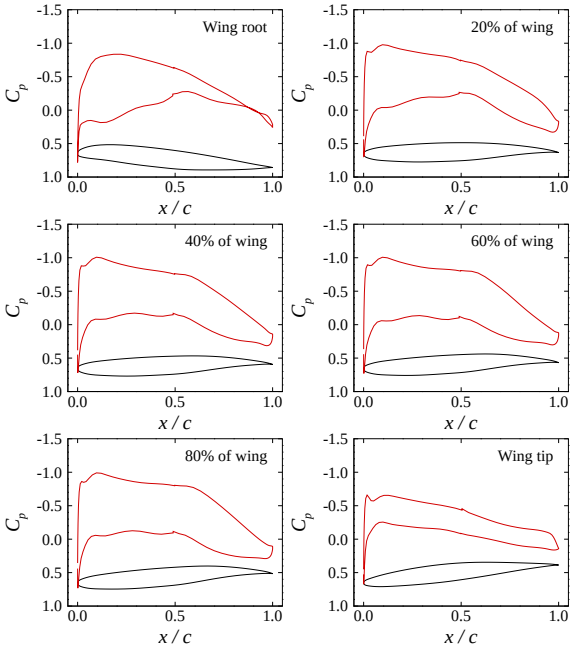

(d) Sectional pressure distributions

Figure 4.6: The optimized CTW300-1 design.

Table 4.2: Percentage of lift carried by the various components of the optimized CTWs.

Design	Fuselage [%]	Wing [%]	Tail [%]
CTW100-1	13.0	91.5	−4.5
CTW160-1	13.5	95.8	−9.2
CTW300-1	11.8	94.4	−6.2

Table 4.3: Optimized CTW performance at the start of cruise.

Design	Weight [lb]	b [ft]	S [ft^2]	S_{wet} [ft^2]	C_L [–]	C_D [–]	L/D [–]	D/q_∞ [ft^2]	Drag [lb]
CTW100-1	91,500	94	935	5,636	0.481	0.0243	19.8	22.7	4,621
CTW160-1	143,300	118	1,370	7,923	0.501	0.0247	20.3	33.8	7,059
CTW300-1	633,900	213	5,209	23,262	0.515	0.0220	23.4	114.7	27,090

4.4 HWB Optimization

This section presents the results of the HWB optimization for each class. The optimized designs will be indicated by the suffix '-1'. For some of the designs, the optimization is conducted in steps, with each optimization warmstarting from a previously converged design. For example, the HWB100C-1 design is warmstarted from the HWB100C-0 optimization discussed in Section 4.1, and the larger span versions of the HWB100C, HWB220D and HWB300E designs are warmstarted from their smaller span counterparts.

Details of the larger span derivatives will be provided, with only performance numbers for the remaining designs. Thus, the focus will be on the HWB100D-1, HWB160D-1, HWB220E-1, and HWB300F-1 designs. For each design, the optimized geometry, surface pressure distribution, spanwise lift distribution, and sectional pressure distributions are shown in Figures 4.7-4.10.

For each class, the action of the optimizer is to wrap the outer mold line of the body around the prescribed cabin shape to minimize wetted area while, in some cases, increasing the chord on the center-body to decrease the maximum t/c. For each class, the wing volume and maximum thickness on the wing go to their lower bounds. With the exception of the wide-body-class HWBs, the tip chords go to their lower bounds. In addition to the cabin shape constraint, these are the only geometric constraints that are active at the optimum. The HWBs all have a final cruise angle-of-attack of between 2.5° and 3.0°.

It is known from linear aerodynamics that an elliptical spanwise lift distribution produces minimum induced drag for a planar wing. When nonlinear considerations are present

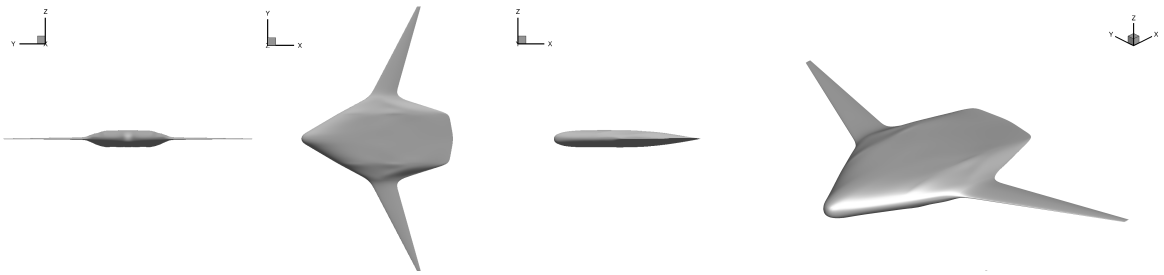

(a) Optimized geometry

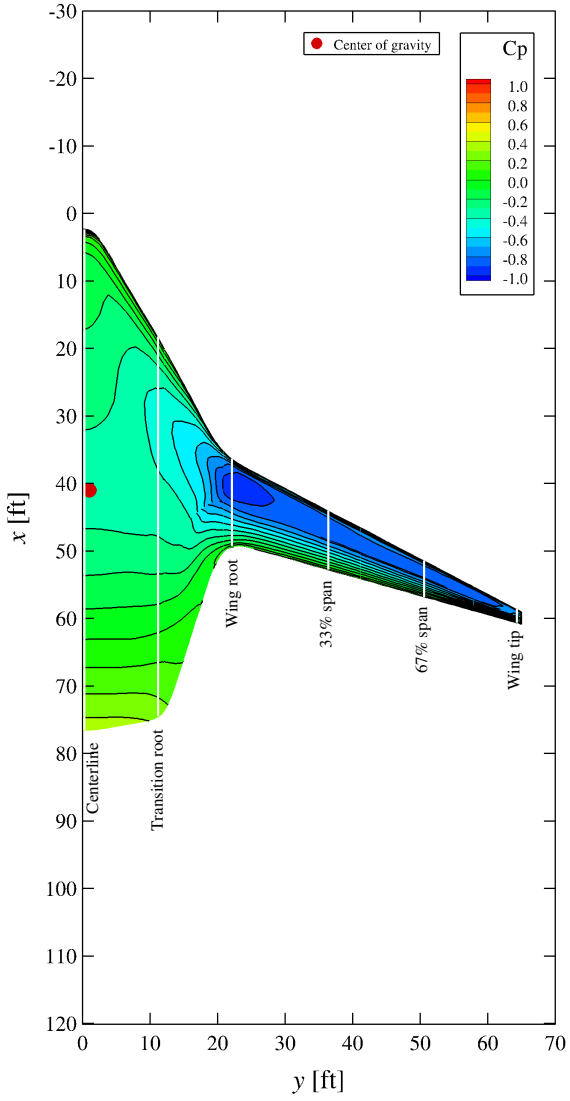

(b) Surface pressure distribution

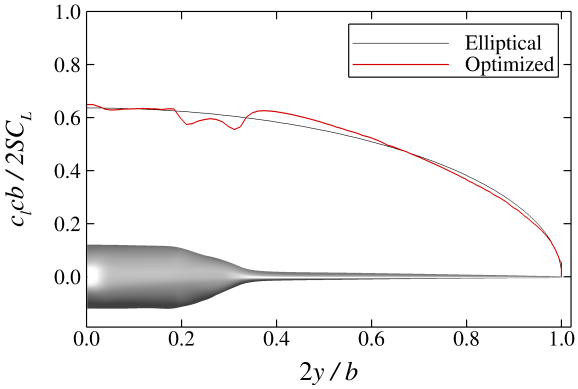

(c) Spanwise lift distribution

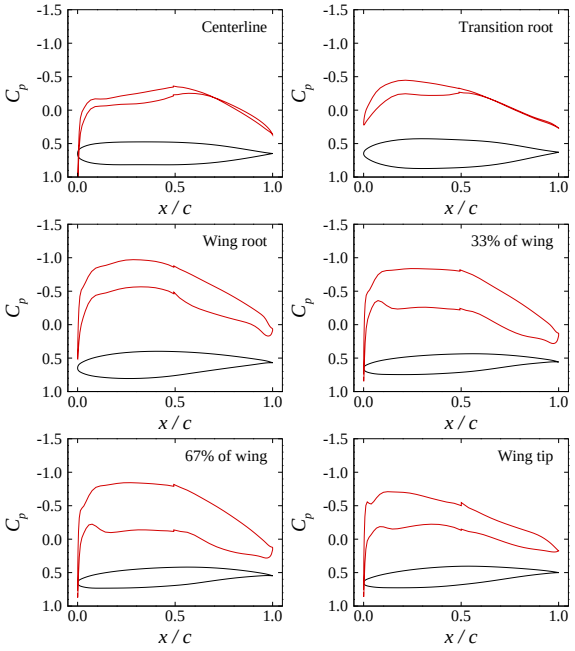

(d) Sectional pressure distributions

Figure 4.7: The optimized HWB100D-1 design.

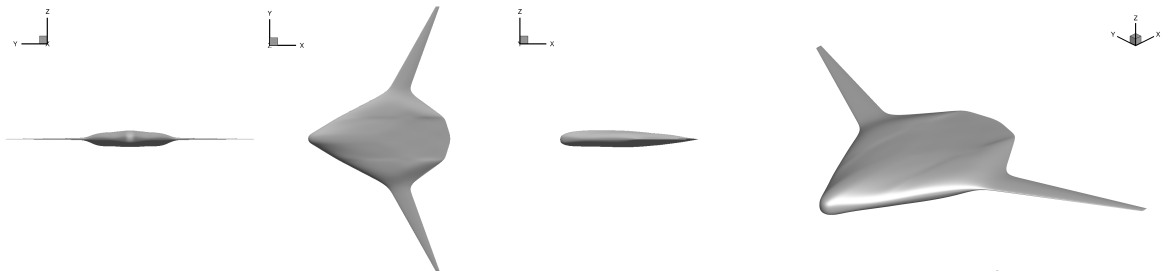

(a) Optimized geometry

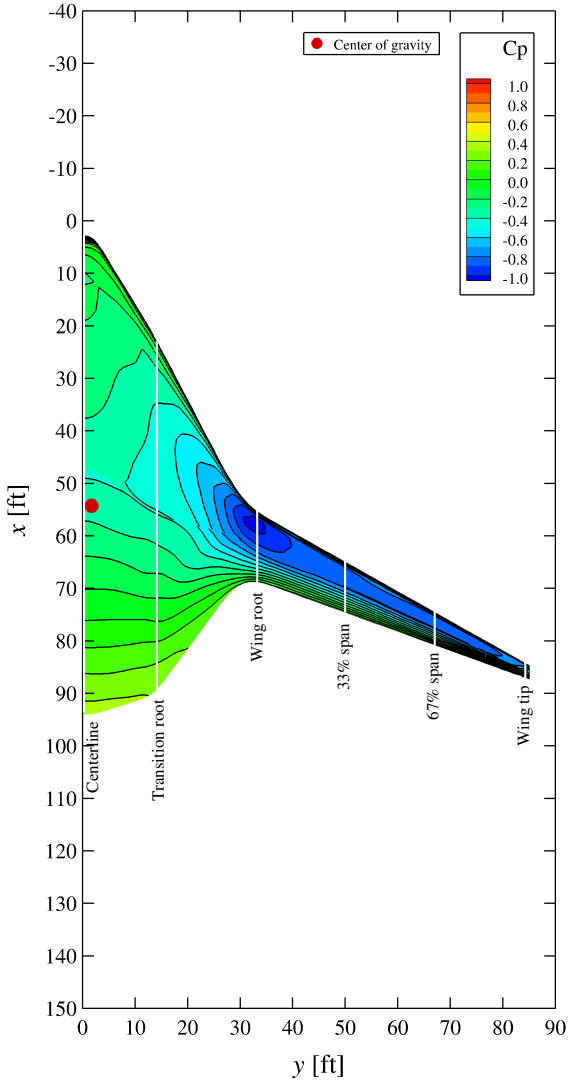

(b) Surface pressure distribution

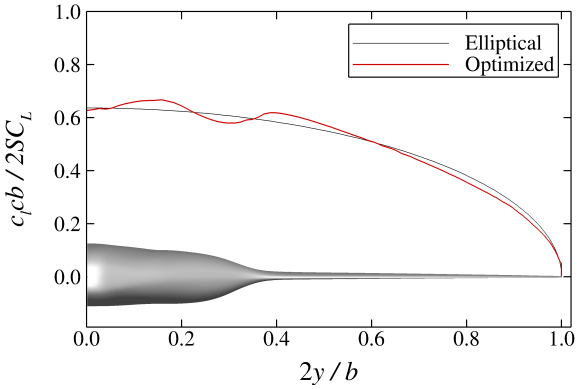

(c) Spanwise lift distribution

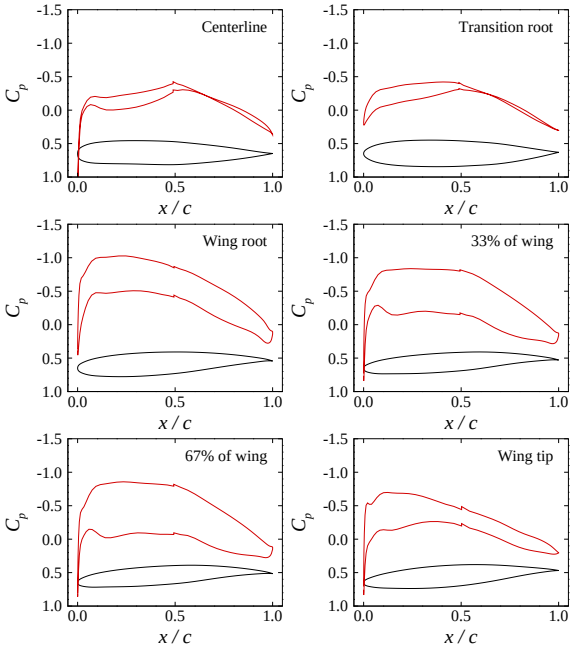

(d) Sectional pressure distributions

Figure 4.8: The optimized HWB160D-1 design.

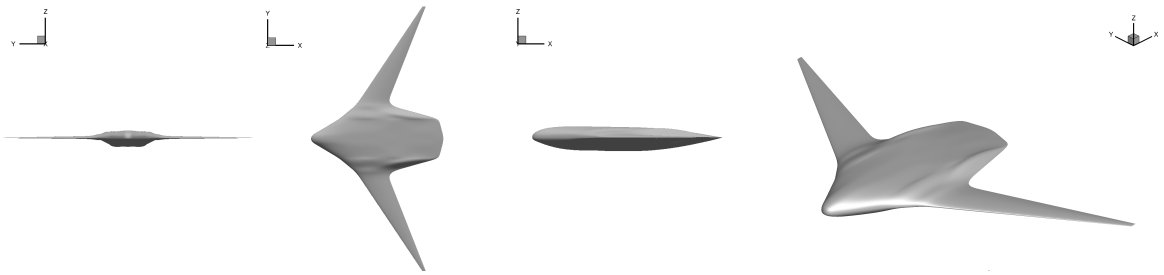

(a) Optimized geometry

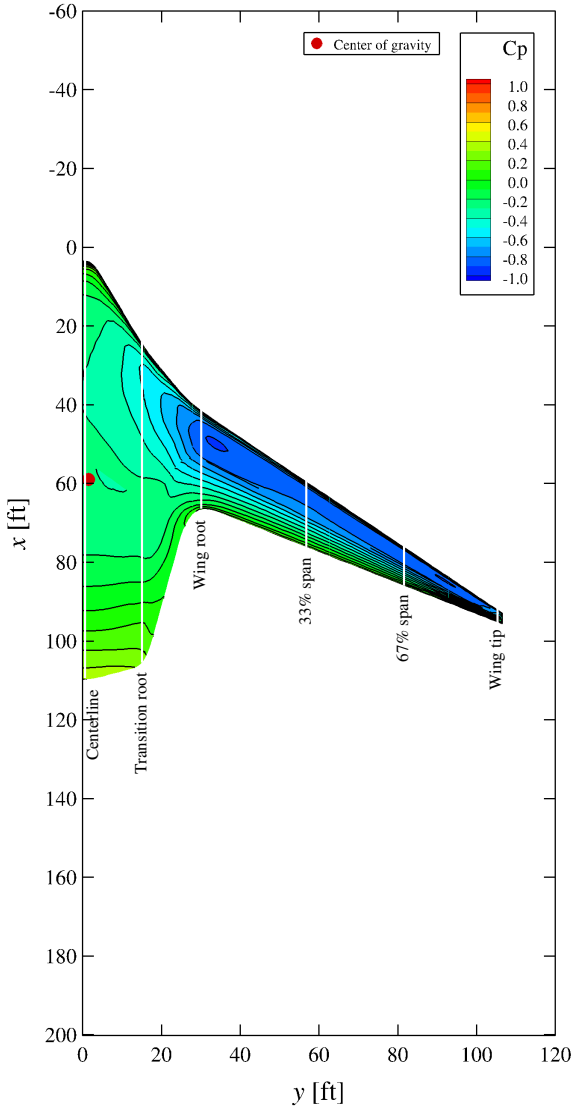

(b) Surface pressure distribution

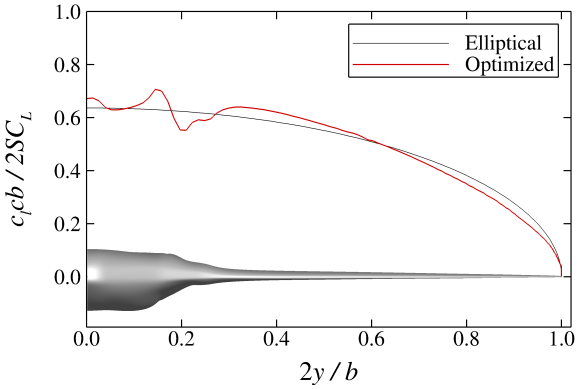

(c) Spanwise lift distribution

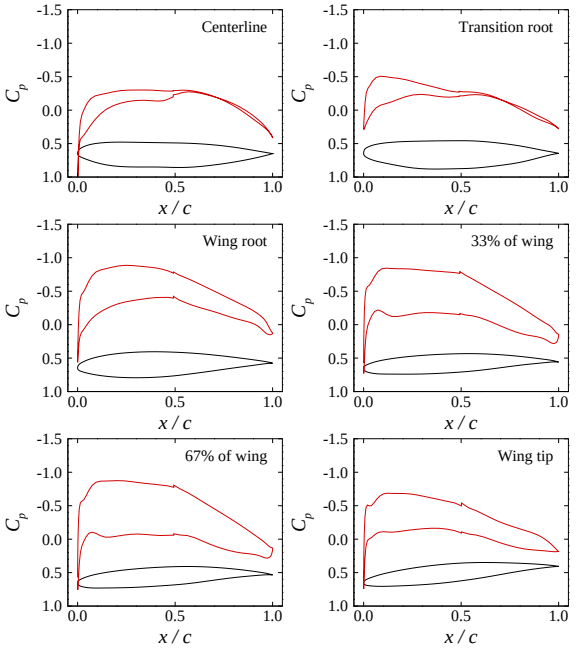

(d) Sectional pressure distributions

Figure 4.9: The optimized HWB220E-1 design.

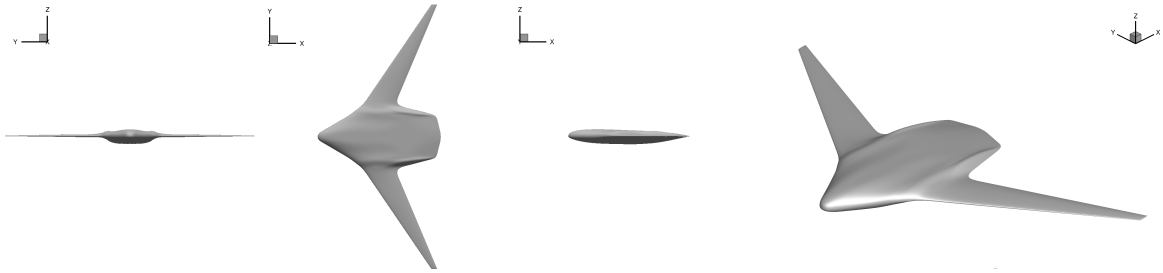

(a) Optimized geometry

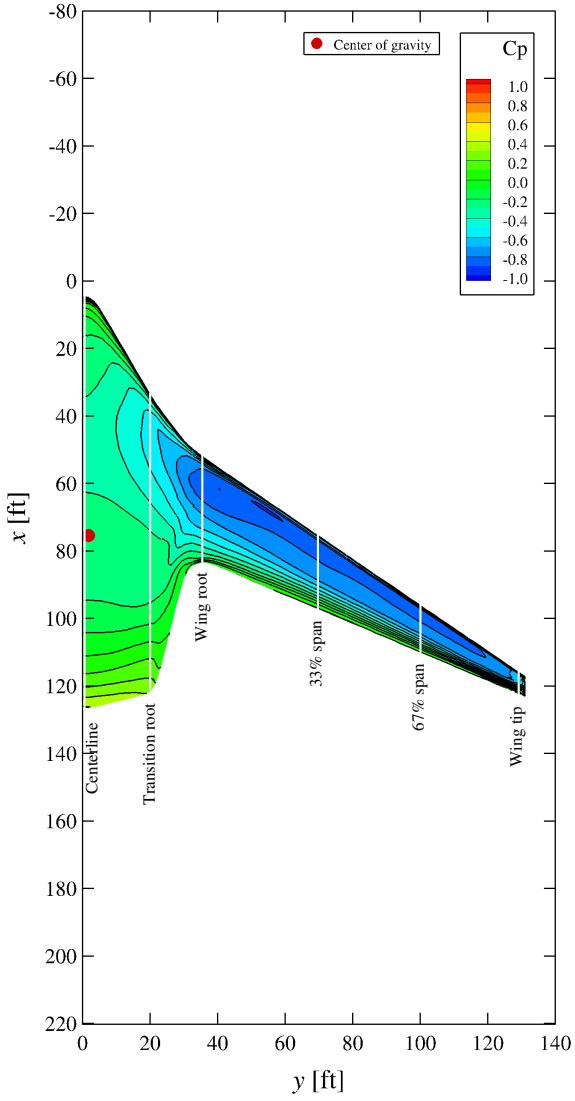

(b) Surface pressure distribution

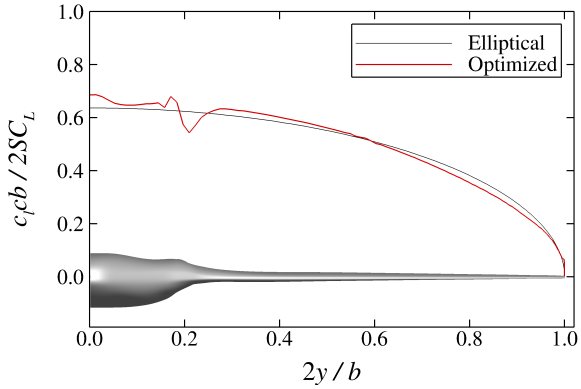

(c) Spanwise lift distribution

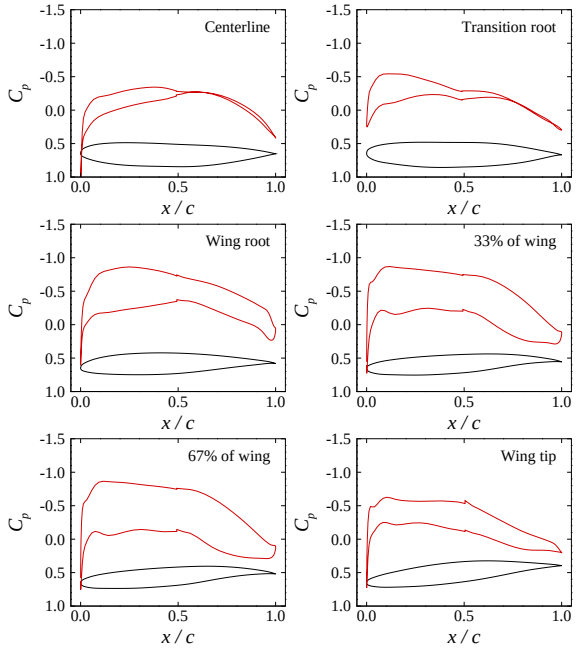

(d) Sectional pressure distributions

Figure 4.10: The optimized HWB300F-1 design.

the same statement cannot be made with such certainty. However, as demonstrated by Osusky et al. [84], a lift distribution close to elliptical can be expected for practical wings in transonic, viscous flows. The spanwise lift distributions shown in Figures 4.7(c)-4.10(c) show near-elliptical behaviour on the wings. There is some deviation, which increases with aircraft size, as a likely consequence of the higher Mach number. As pointed out by Qin et al. [53,73] this can be expected for transonic problems, particularly those with high local lift coefficients, as the optimizer must balance the reduction in induced drag with wave drag. Additional considerations such as the fact that the wings are swept and that they contribute to the trim of the aircraft also place further restrictions on the lift distribution that is optimal for total drag. For each design, there is significant deviation from an elliptical distribution over the center-body-wing transition region due to the rapid change in thickness and chord.

Figures 4.7(d)-4.10(d) show the sectional pressure distributions at the centerline, the transition root (which is at the outboard edge of the cabin where the chord begins to decrease rapidly), and four stations between the wing root and tip. The designs are shock free and nearly separation free. The sectional pressure distributions show the manner in which the optimizer trims the HWBs. The center-body sections are fore-loaded such that they carry almost all of their lift ahead of the center of gravity, with very little inefficient reflex required. The optimizer has found the same trim mechanism as described by Sargeant et al. [23]. The optimizer trims the designs primarily through the center-body design since the large chord implies that small changes in the local c_m produce a significant total change in the pitching moment without inducing large performance penalties associated with strongly fore-loaded sections, as noted by Mialon et al. [127]. On the wing, the optimizer designs supercritical sections. While trimmed, all of the designs are longitudinally unstable, with static margins between 0% and -9.4% and would require some form of an active stability system. The implication of stability requirements will be addressed in Chapter 7.

The distribution of lift on the HWBs is shown in Table 4.4. Across all classes, the HWBs carry 32-46% of the total lift on the center-body, although the center-body is also a large contributor to drag due to both its large wetted area compared to the wings, and the fact that it carries a substantial portion of the total lift. Here, the center-body is taken to mean both the pressurized area and the transition region, i.e. the portion of lift not carried by the wings.

The performance of the optimized designs is given in Table 4.5, with two primary points to note. First, the lift coefficient, and hence wing loading, increases with aircraft size. This would suggest that a higher cruise altitude is required to attain maximum L/D for the smaller sizes. This will be addressed in Chapter 6. Secondly, the lift-to-drag ratio increases

Table 4.4: Percentage of lift carried by the center-body and wing of the optimized HWBs.

Design	Center-body [%]	Wing [%]
HWB100C-1	42.8	57.2
HWB100D-1	40.3	59.7
HWB160D-1	45.8	54.2
HWB200D-1	36.4	63.6
HWB220E-1	33.5	66.5
HWB300E-1	37.7	62.3
HWB300F-1	32.2	67.8

Table 4.5: Optimized HWB performance at the start of cruise.

Design	Weight [lb]	b [ft]	S [ft^2]	S_{wet} [ft^2]	C_L [–]	C_D [–]	L/D [–]	D/q_∞ [ft^2]	Drag [lb]
HWB100C-1	103,100	118	2,732	6,264	0.185	0.0084	22.1	23.0	4,665
HWB100D-1	106,600	130	2,813	6,422	0.186	0.0081	23.0	22.8	4,635
HWB160D-1	185,300	170	4,468	10,070	0.198	0.0080	24.9	35.6	7,444
HWB220D-1	328,000	170	5,788	13,217	0.265	0.0104	25.4	60.2	12,717
HWB220E-1	355,400	213	6,388	14,399	0.260	0.0090	28.9	57.5	12,298
HWB300E-1	638,000	213	8,949	20,323	0.302	0.0117	25.8	104.9	24,729
HWB300F-1	700,500	262	9,467	21,377	0.313	0.0104	30.0	98.8	23,350

with aircraft size. This is partially a consequence of the larger designs operating closer to their optimal lift coefficient, and partly a result of the higher wetted aspect ratio as discussed in Chapter 5. Note that the numbers listed in Table 4.5 include the drag contribution from the vertical stabilizers, but not from the propulsion system or excrescence sources.

As seen in Tables 4.3 and 4.5, the aerodynamic efficiency, i.e. lift-to-drag ratio, for each HWB is higher than its CTW counterpart, with the largest benefit for the HWB300F-1 at over 28%. However, for each class, the HWBs are heavier than their CTW counterpart, such that not all of the aerodynamic efficiency benefits are realized in terms of a drag reduction. The regional-class HWB100D-1 has higher drag than the CTW100-1, while the narrow-body HWB160D-1 has a significant drag penalty, and the wide-body HWB300F-1 has 13.8% lower drag than the CTW300-1.

One of the oft-quoted benefits of the HWB concept is its lower wetted area compared to equivalent CTW designs, particularly for large aircraft. However, the regional and narrow-

body-class HWBs, the HWB100D-1 and HWB160D-1, have 14-27% *higher* wetted area than the CTW100-1 and CTW160-1, respectively. The wetted area for the wide-body HWB300F-1 is 8% lower than that of the CTW300-1. This motivates the question, which forms the basis for the next chapter: Is there a different HWB configuration that is more beneficial for smaller aircraft sizes?

Chapter 5

Exploratory Aerodynamic Design Through High-Fidelity Optimization

The HWBs investigated in Chapter 4 are classically shaped, i.e. they resemble scaled versions of Liebeck's designs. As shown in the previous chapter, for the smaller aircraft, the aerodynamic benefit was not as substantial as for the larger sizes. This is in line with the parametric results of Appendix B, which also show that the shapes for minimum S_{wet} for smaller aircraft are significantly different than the classical shape, which is optimal for larger sizes.

While the optimizations previously presented possessed significant geometric freedom, the specification of the cabin layout and the resulting cabin shape constraint prevented significant geometric changes being made to the center-body, a large source of wetted area, and hence drag. Thus, to investigate alternative HWB shapes that may offer improved aerodynamic efficiency, an exploratory optimization is performed with the cabin shape constraint removed, resulting in increased geometric freedom. The cabin shape constraint is replaced with requirements on the center-body area and volume. This study aims to find the maximum aerodynamic efficiency of the HWB concept. Thus, instead of performing lift-constrained drag minimization as with the original designs, the optimization objective is to maximize the lift-to-drag ratio. No lift target is required, and the pitching moment constraint is not considered. This also reduces the computational cost, as only one adjoint solve is required as compared to the three in the trim-constrained cases. This exploratory optimization is performed for each class of HWB considered so as to understand how the aerodynamically optimal shape changes with aircraft size.

The starting geometry for each HWB is the baseline shape from Section 3.2. The required cabin floor area and usable cabin volume for each class of HWB is shown in Table 5.1.

Table 5.1: Required cabin floor area for each aircraft class, and the associated cabin volume.

Class	Cabin floor area [ft^2]	Cabin volume [ft^3]
Regional-jet	770	5,000
Narrow-body	1,170	8,040
Mid-size	1,700	11,900
Wide-body	3,000	21,000

The assumption is made that only 50% of the projected area and volume of the center-body is usable for housing the cabin due to minimum dimension requirements; the area and volume of the center-body are constrained accordingly.

The design variables and constraints for these problems are similar to those used for the HWB optimizations presented in Chapter 4, with some notable exceptions. The first, already mentioned, is the substitution of the cabin area and volume constraints for the explicit shape constraint. Secondly, the center-body is defined by two segments instead of the three shown in Figure 4.3(b), i.e. the first two segments are combined to represent the center-body.[1] Finally, the leading and trailing edges of the center-body are not required to be straight. There are a total of 425 effective design variables.

The aim of these studies is to find trends in the optimal shape rather than details. Few constraints are imposed, and these studies are intended to guide the design of HWBs which can then take additional requirements into consideration. For example, the resulting shape may have sufficient space in the center-body for the payload, but due to minimum dimension requirements cannot accommodate a practical cabin configuration, thus necessitating a manually designed center-body whose shape is guided by the exploratory result. Such designs will be developed, and subsequently optimized, in Section 5.2.

5.1 Exploratory Optimization Results

The resulting shapes of the exploratory optimization are shown in Figure 5.1, and are identified with the suffix '-E1'. For all cases, the primary action of the optimizer is to minimize the wetted area. All of the area and volume constraints thus go to their lower bounds. For each case, the optimizer decreases the span of the center-body to create a more elongated

[1] With the original three-segment definition, there is no justification for constraining the volume of the transition segment, and the optimizer would thus decrease the transition-span to its lower bound, leading to mesh-movement complications for some classes. For those classes which were successful, the optimal shape was similar to that with the two-segment formulation.

Table 5.2: Summary of exploratory performance for the E1 formulation.

Design	Span [ft]	Bending span [ft]	$\mathcal{R}_{\text{wet}}$ [–]	L/D [–]
HWB100C-E1	118	90	2.6	28.7
HWB160D-E1	170	129	3.5	33.5
HWB220E-E1	213	162	3.8	34.7
HWB300F-E1	262	176	3.5	32.5

shape, while the thickness is limited by transonic effects. The degree to which this occurs decreases with increasing size. The regional and narrow-body-class designs produce a slender center-body with distinct wings, while, for the wide-body, the center-body and wings are more blended together. The net effect is to increase the wetted aspect ratio, and hence the aerodynamic efficiency, both of which are given in Table 5.2. Since the goal of the exploratory optimization is the determination of an optimal shape, the exact aerodynamic performance is less important. As such, for the aerodynamic performance presented in this section, grid refinement studies are not performed. Rather, for each HWB class, the drag error between the optimization level grid and the Richardson extrapolated value is calculated from the lift-constrained drag minimization results of Chapter 4 and applied to the drag computed on the optimization level grids for the cases in this section. This gives a grid-converged performance estimate for each exploratory result, without the cost of grid refinement studies.

It can be seen in Table 5.2 that the wetted aspect ratio, and hence lift-to-drag ratio, increase with aircraft size. The exception to this is the wide-body, for which the choice of the 262 ft span is such that the wetted area has scaled faster than the span for this class relative to the other three. For this class of HWB, the code 'F' gate limit places a hard limit on the aerodynamic performance, as evidenced by the fact that the bending span for this class is the only one that is lower than its equivalent CTW design. Even in this best-case scenario, the large class of HWB would require a span greater than the maximum allowable code 'F' gate to attain a monotonic increase in aerodynamic performance with aircraft size.

All of the above designs have a fixed span. Thus, when the center-body span decreases in order to reduce the wetted area, the bending span must increase. This is beneficial from a purely aerodynamic point of view, but does not consider potential changes in structural weight. To address this, a second problem formulation is investigated, referred to with the suffix '-E2', to ensure that the E1 shapes are not purely a consequence of the problem formulation. The design variable definition is the same as for the E1 cases, except that the total span is free, and the span of the wing region, i.e. the bending span, is fixed at

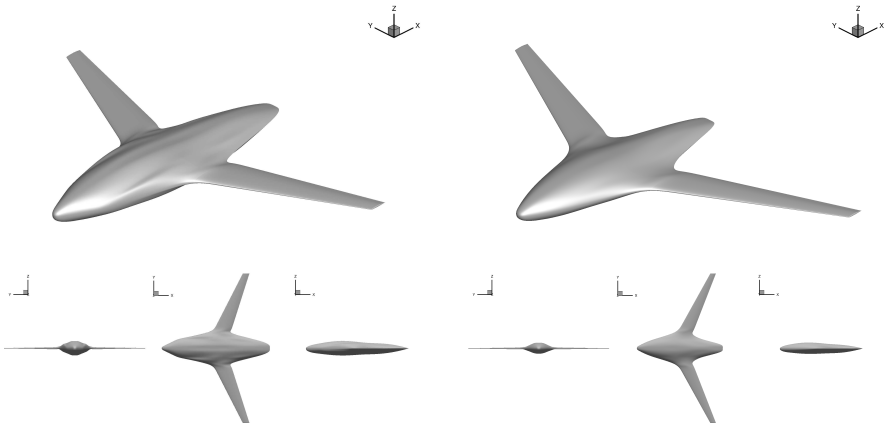

(a) HWB100C-E1

(b) HWB160D-E1

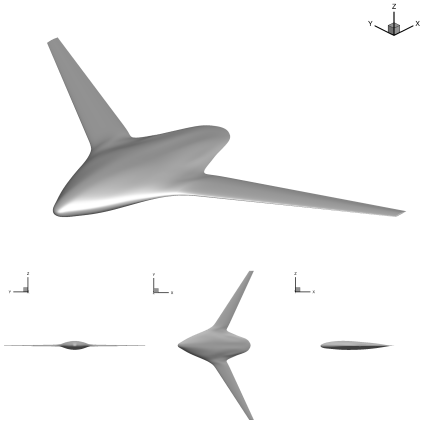

(c) HWB220E-E1

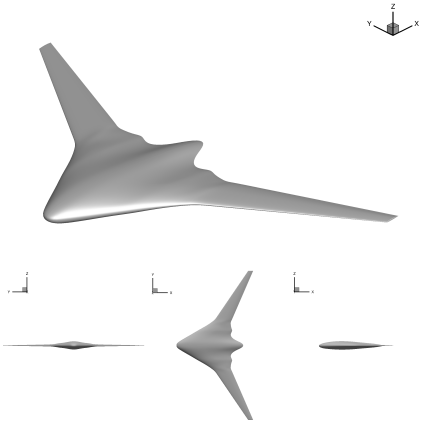

(d) HWB300F-E1

Figure 5.1: Resulting shapes from the 'E1' exploratory optimizations. (Not shown to the same scale.)

the value corresponding to the equivalent CTW aircraft. For this problem, the action of the optimizer would be to increase the center-body span and decrease its chord such that the cabin area constraint would not go to its lower bound, while the thickness decreases so that the volume reaches its lower bound. In other words, the HWB reduces to a pure flying wing, one in which the thickness on the center-body is now insufficient to hold the payload. To prevent this, an average thickness constraint is introduced on the center-body, defined as $\bar{t}_{\text{cab}} = V_{\text{cab}}/A_{\text{cab}}$, where A_{cab} and V_{cab} are the cabin area and volume requirements, respectively. This constraint always goes to its lower bound and thus ensures that there is sufficient floor area, volume, and on average the thickness is sufficient to accommodate the payload. The resulting shapes from the optimization are shown in Figure 5.2, and the corresponding performance is given in Table 5.3. For this problem formulation, the span is not constrained by gate limits, and thus the HWB300F-E2 is able to increase its span;

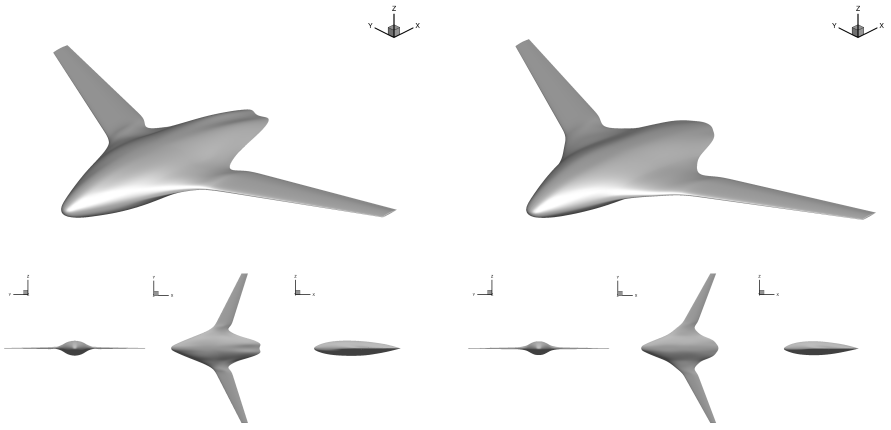

(a) HWB100C-E2

(b) HWB160D-E2

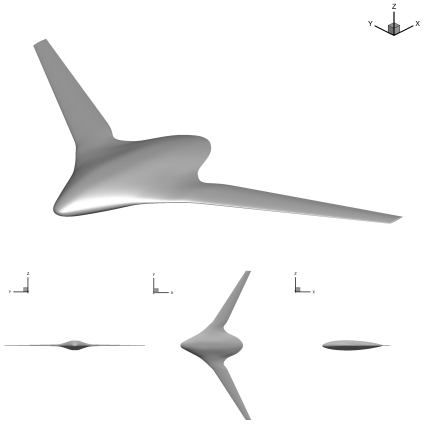

(c) HWB220E-E2

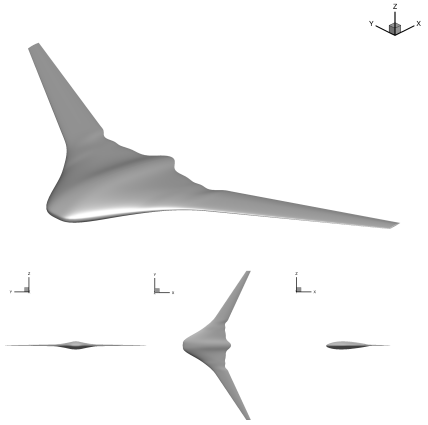

(d) HWB300F-E2

Figure 5.2: Resulting shapes from the 'E2' exploratory optimizations. (Not shown to the same scale.)

hence a monotonic increase in the wetted aspect ratio is obtained across all of the classes. However, despite its higher wetted aspect ratio, the HWB300F-E2 has a lower lift-to-drag ratio than the HWB220E-E2. This is likely a consequence of nonlinear aerodynamics which the correlation of lift-to-drag ratio and wetted aspect ratio does not consider, such as the consequence of the higher Mach number for the HWB300F-E2.

These optimizations produce the same trends as were found in the E1 optimizations, where the center-body spans are reduced compared to the initial shapes. This shows that this is still the optimal configuration when the bending span is considered as a surrogate for wing weight. One thing to note is that the span, and hence wetted aspect ratio, of the HWB160D-E2 is less than in the E1 case. This is due to the fact that the bending span for the E2 is significantly less than in the E1 case, and the same span, wetted aspect ratio, and hence lift-to-drag ratio could not be obtained in this case.

Table 5.3: Summary of exploratory performance for the E2 formulation.

Design	Span [ft]	Bending span [ft]	$\mathcal{R}_{\text{wet}}$ [–]	L/D [–]
HWB100C-E2	122	85	2.9	28.8
HWB160D-E2	157	105	3.3	31.5
HWB220E-E2	218	153	4.0	34.8
HWB300F-E2	294	193	4.3	34.0

5.2 Lifting-Fuselage Configuration Design

The exploratory results of the previous section suggest the shape for optimal aerodynamic efficiency in each class. However, while the center-body volume and area are sufficient to hold the payload if it were to take on an arbitrary shape, the imposition of minimum dimension requirements and other practical considerations leads to the shapes not being capable of holding the payload exactly as they are. Thus, these shapes are used to guide the redesign of aircraft that mimic the results of the previous section, while considering practical requirements such as a feasible cabin layout and trim.

The new designs are significantly different than the classical HWBs, and are characterized by a slender fuselage with distinct wings, where the fuselage still carries a significant portion of the lift. As such, the new designs, presented below, will be termed 'Lifting-Fuselage Configurations' (LFCs). As with the original designs, low-fidelity models of the lifting-fuselage designs are created and are shown in Figure 5.3, with design information given in Table 5.4, and the conditions at the start of cruise shown in Table 5.5. As in Section 3.2, the determination of an appropriate wing span is challenging without a full multidisciplinary design process. The bending span is again used as a surrogate for wing weight. For the regional-class design, termed the LFC100, the bending span is 88 ft for a total span of 118 ft; this is the same bending span as the HWB100D, and close to that of the CTW100. For the narrow-body LFC, the LFC160, the total span is 155 ft which gives a bending span of 110 ft, close to that of the CTW160 and the same as the HWB160D. At a total span of 200 ft, the mid-size LFC, LFC220, has a bending span of 150 ft, similar to the CTW220 and equivalent to the HWB200E. Each of these designs reside in the code 'C', 'D', and 'E' gates, respectively. Only the regional-class LFC, the LFC100, is at a gate limit; the narrow-body and mid-size LFCs are driven by the bending span.

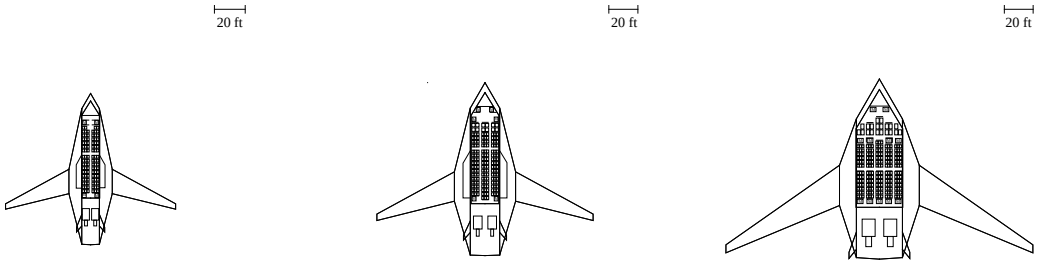

(a) LFC100 (b) LFC160 (c) LFC220

Figure 5.3: Planforms for each of the LFC designs.

Table 5.4: LFC design information.

Design	PAX	Gate	Span [ft]	Bending span [ft]	Area [ft^2]	Wing aspect ratio [–]	MAC [ft]	Max range [nmi]	Max payload [lb]	OEW [lb]	MTOW [lb]
LFC100	100	C	118	88	3,120	8.5	62.8	2,900	28,400	71,100	118,700
LFC160	160	D	155	110	5,140	8.8	73.8	3,700	47,000	122,100	212,400
LFC220	220	E	200	150	7,170	9.0	71.2	8,000	78,400	222,400	436,300

Table 5.5: LFC design information at the start of the nominal mission.

Design	Range [nmi]	ICA [ft]	Mach [–]	Payload [lb]	Weight[3] [lb]
LFC100	500	36,000	0.78	22,000[1]	104,100
LFC160	1,000	36,000	0.79	35,200[1]	180,500
LFC220	3,000	36,000	0.80	61,200[2]	356,900

[1] Full passenger payload (@ 220 lb/PAX)
[2] Full passenger payload plus 50% revenue cargo
[3] At the start of cruise

An attempt was made to create an LFC for the wide-body class, but when a practical cabin layout was created, the resulting design was similar to that of the baseline classical HWB. Thus, no wide-body class LFC is pursued. The same 'home plate' center-body pressure vessel weight model is used for the LFCs as was used for the HWBs. Due to the reduced span loading of the LFC concept, an alternative configuration such as an elliptical or double-bubble cross section could lead to lower center-body weight. Uncertainty in the weights and the use of an alternative pressure vessel weight model will be studied in Section 7.1. The LFC100 and LFC160 have cargo located outboard of the passenger compartment, while the LFC220 has under-floor cargo. Three-dimensional CFD models are created for each of these designs in the same manner as for the HWBs.

5.3 Aerodynamic Shape Optimization of LFC Designs

Trim-constrained drag minimization of the LFC designs is performed in the same manner as with the HWB designs. Geometry and solution information for each of the three classes is shown in Figures 5.4-5.6. The optimized designs are denoted by the suffix '-1'.

As with the HWBs, each design has a lift distribution close to elliptical, particularly on the wings. All designs are shock free and nearly separation free, with most of the center-body lift being carried ahead of the CG. The LFC220-1 is the only design that exhibits any reflex on the fuselage, while the LFC100-1 and LFC160-1 carry essentially no lift aft of 50% chord on the fuselage. Due to the long fuselage chord of the LFC designs, the t/c at the centerline is quite reasonable at 9.6%, 9.7%, and 9.8%, smaller than that of the HWBs. While all designs are shock free, the smaller t/c of the LFCs would aid in maintaining good off-design performance. For each class the wing volume and maximum thickness on the wing go to their lower bounds, as does the tip chord. All of the designs have a cruise angle-of-attack of between 2.5° and 3.0°.

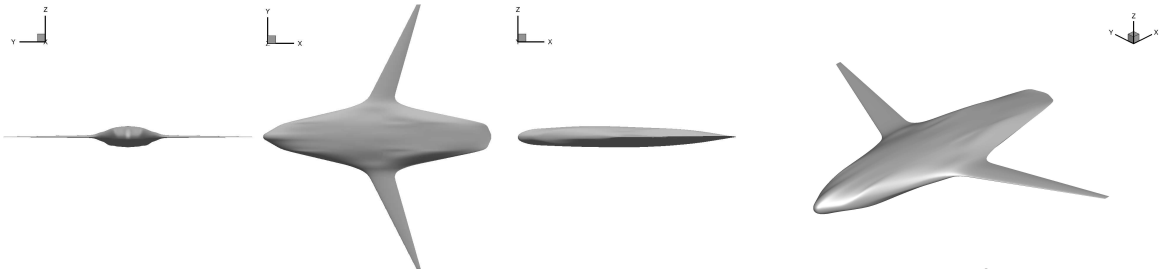

(a) Optimized geometry

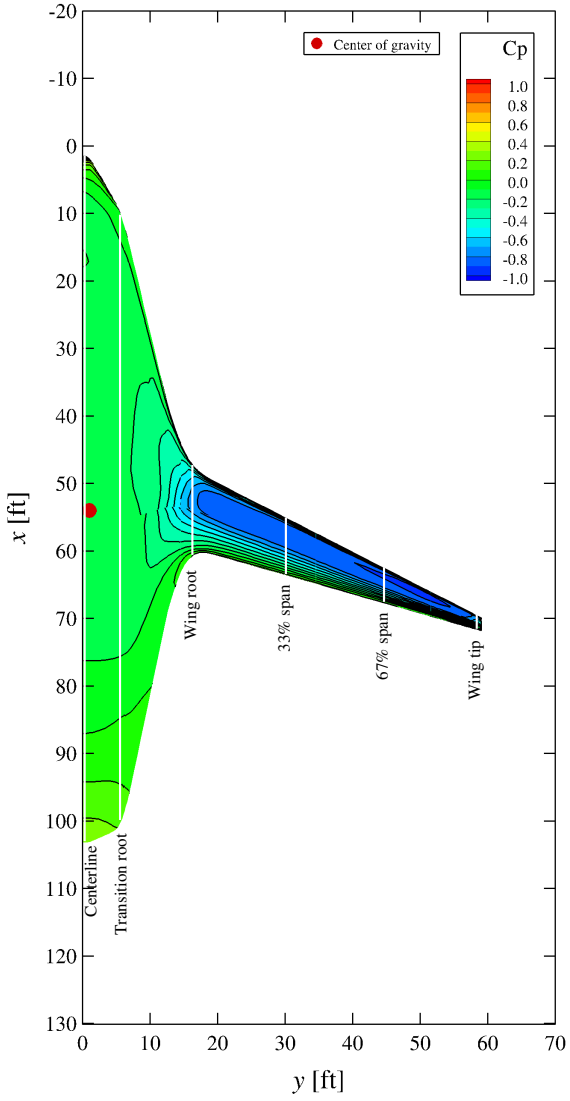

(b) Surface pressure distribution

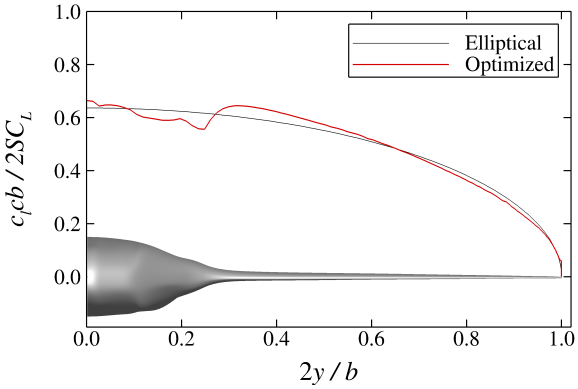

(c) Spanwise lift distribution

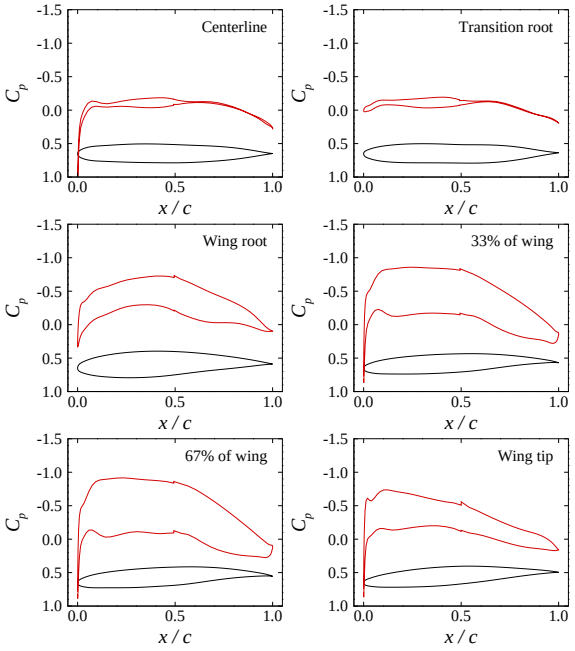

(d) Sectional pressure distributions

Figure 5.4: The optimized LFC100-1 design.

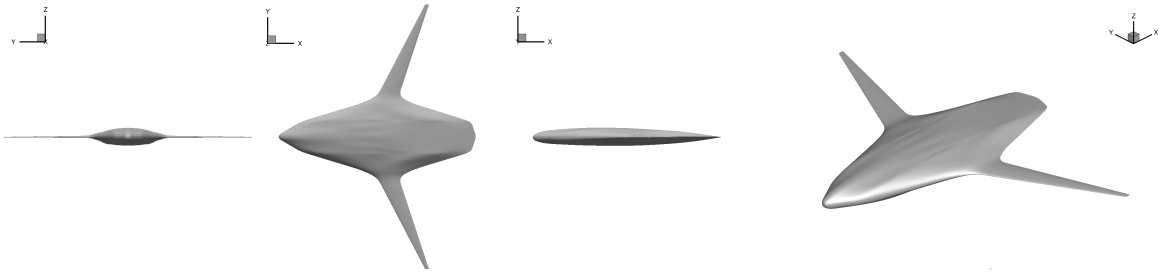

(a) Optimized geometry

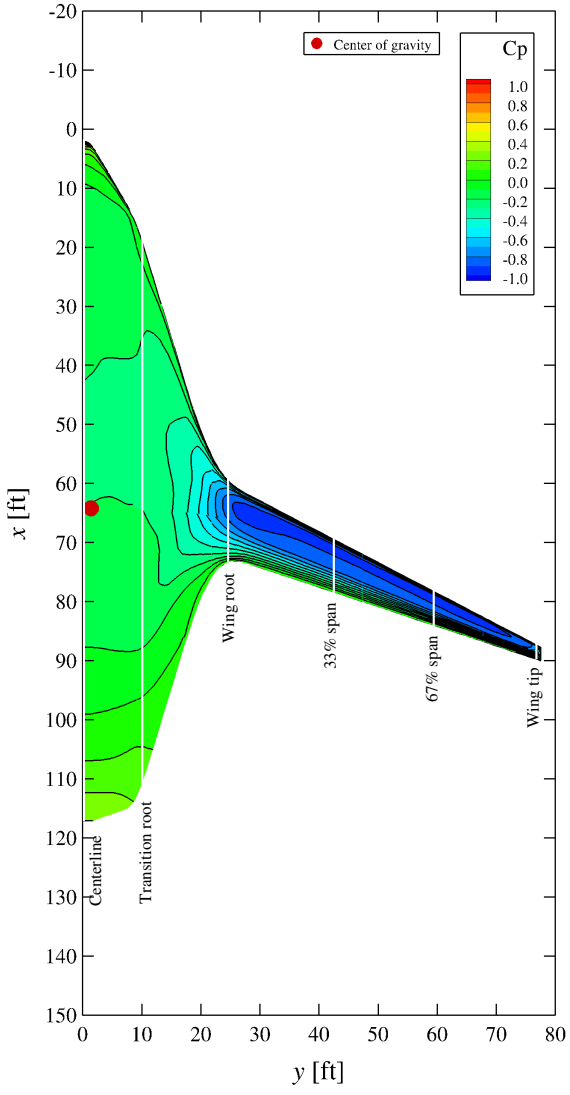

(b) Surface pressure distribution

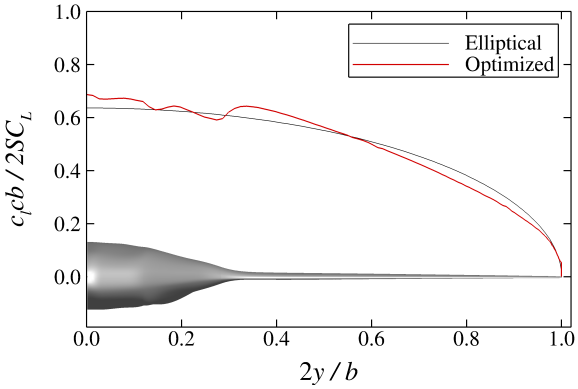

(c) Spanwise lift distribution

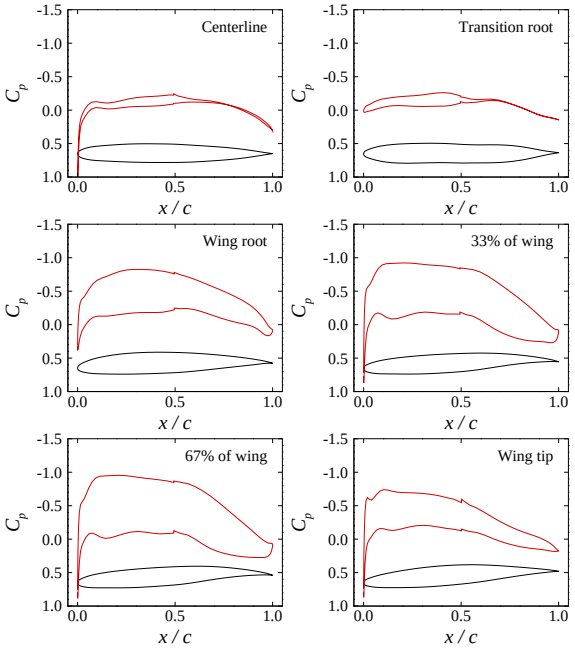

(d) Sectional pressure distributions

Figure 5.5: The optimized LFC160-1 design.

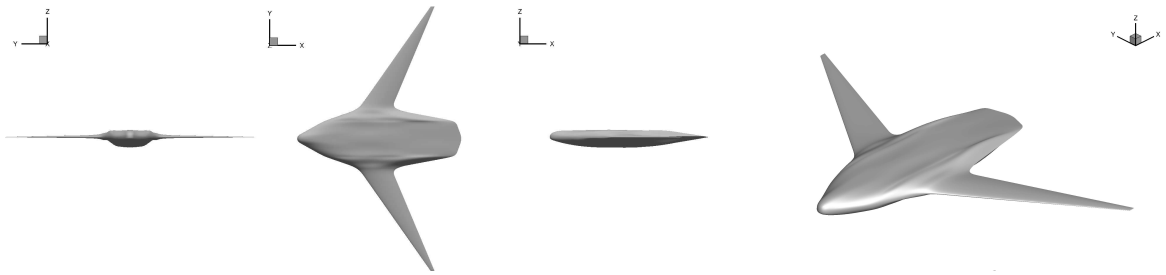

(a) Optimized geometry

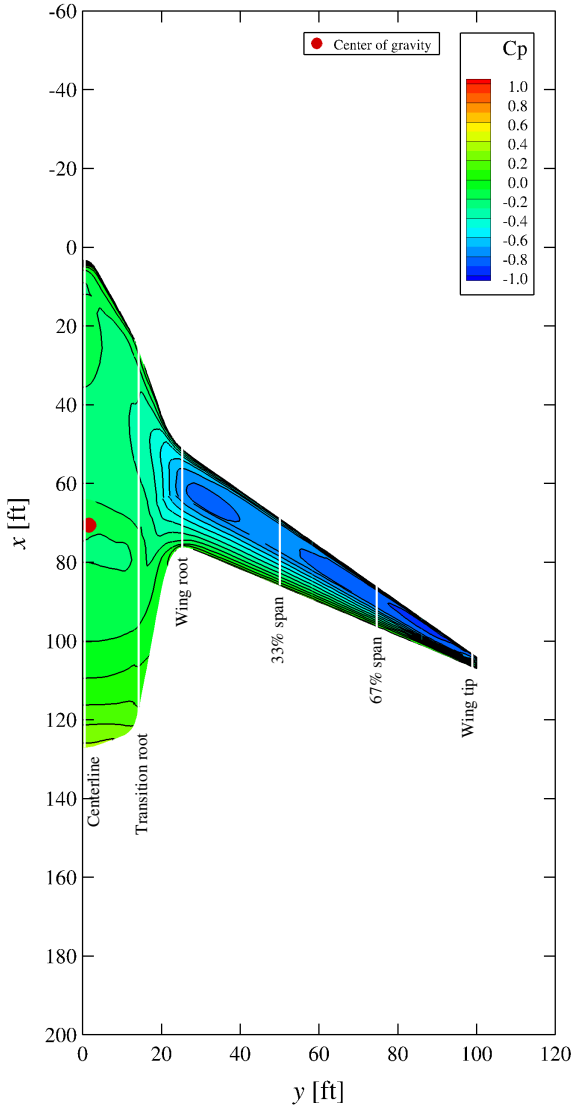

(b) Surface pressure distribution

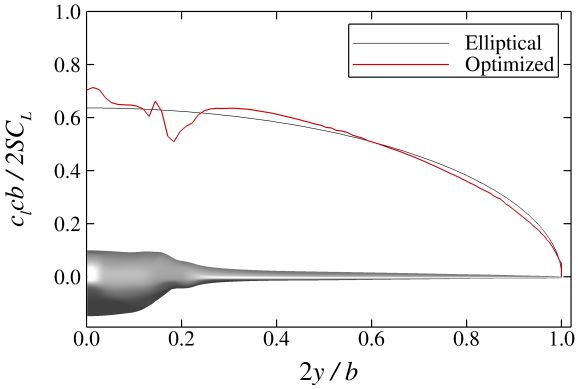

(c) Spanwise lift distribution

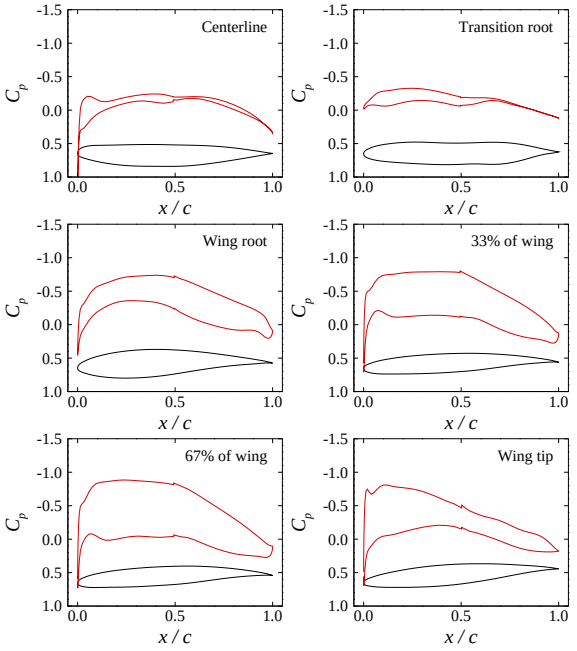

(d) Sectional pressure distributions

Figure 5.6: The optimized LFC220-1 design.

Table 5.6: Percentage of lift carried by the center-body and wing of the optimized LFCs.

Design	Center-body [%]	Wing [%]
LFC100-1	31.5	68.5
LFC160-1	37.4	62.6
LFC220-1	29.0	71.0

Note the sudden transition between the fuselage and wing for the LFC220-1 compared to the more gradual transition for the LFC100-1 and LFC160-1. This is a consequence of the cargo being located outboard of the passenger cabin for the LFC100 and LFC160 designs, while beneath the passenger cabin for the LFC220.

The fuselage for each LFC class carries 32%, 37%, and 29% of the lift for the regional, narrow-body, and mid-size LFCs, respectively. See Table 5.6. This is in comparison to the HWBs which carry 40%, 46%, and 34% of their lift on the center-body, for the same classes, respectively. Here, the center-body is taken to mean the both the pressurized area and the transition region, i.e. the portion of lift not carried by the wings. While each LFC fuselage carries less lift than the corresponding HWB, it is a significantly larger fraction than the 12-13% carried by the CTW fuselages. For reference, the 'double-bubble' D8 configuration which features a lifting fuselage [7], carries 19% of its lift on the fuselage. The LFC concept presented here shares features of both the HWB and D8 concepts. The LFC's fuselage carries more lift than that of the D8 but less than that of the HWB, and maintains the smooth transition between the fuselage and wing as present in the HWB concept.

The performance of the optimized LFC designs is shown in Table 5.7. The lift-to-drag ratio for all of the LFCs is up to over 4% higher than that of the equivalent HWBs, and 21-27% higher than the CTWs. The LFC's higher aerodynamic efficiency, together with the lower weight compared to the HWBs, yields cruise drag savings relative to both the HWBs and CTWs with the exception of the mid-size class. The regional-class LFC has 6.1% lower drag than the CTW, and 6.4% lower drag than the HWB100D-1. In the narrow-body class, the LFC has about the same drag as the CTW, and 5.6% lower drag than the HWB160D-1. In the mid-size class, the LFC and HWB have similar drag. The fuel burn performance of the LFC concept relative to both the CTW and HWB designs for each class is discussed in the next chapter.

While the regional and narrow-body-class HWBs had up to 27% higher wetted area than the CTWs, and the LFCs still have higher wetted area than the CTWs, the difference is reduced to 10% and 20% for the regional and narrow-body-class LFCs, respectively. The

Table 5.7: LFC performance at the start of cruise.

Design	Weight [lb]	b [ft]	S [ft^2]	S_{wet} [ft^2]	C_L [–]	C_D [–]	L/D [–]	D/q_∞ [ft^2]	Drag [lb]
LFC100-1	104,100	118	2,674	6,191	0.191	0.0080	24.0	21.3	4,338
LFC160-1	180,500	155	4,286	9,548	0.202	0.0079	25.7	33.6	7,023
LFC220-1	356,900	200	6,306	14,192	0.264	0.0092	28.8	57.9	12,392

increased wetted area relative to the CTWs is, however, contrasted with a larger span than the CTWs (but similar bending span), such that the wetted aspect ratio of the LFCs is 43% higher than the CTWs in these two classes. The next chapter will further discuss the relative cruise performance of the three concepts.

Chapter 6

Performance Comparison of the Three Configurations

This chapter compares the relative performance, specifically cruise fuel burn, of the three configurations, and demonstrates how the relative performance changes as the designs are allowed to cruise at their optimal altitudes. Only the most promising designs from the previous chapters are pursued, that is, only the HWBs with bending spans equivalent to their CTW counterparts, i.e. the HWB100D, HWB160D, HWB220E, and HWB300F, in addition to all of the LFCs.

6.1 Operation at Optimal Altitude

As noted in Chapter 4, the lower wing loading of the HWBs and LFCs implies a higher cruise altitude to attain the maximum lift-to-drag ratio. To determine the optimal altitude and the corresponding design, the following process is followed. First, optimizations to maximize the lift-to-drag ratio are performed using the same variables, pitching moment constraint, and geometric constraints as for the trim-constrained problems. This allows the optimizer to determine an optimal shape and lift coefficient. This results in lift coefficients higher than those for the trim-constrained cases. To satisfy $W = L = C_L S q_\infty$, this implies a higher cruise altitude for the HWBs and LFCs. However, since Reynolds number decreases with altitude, this would result in an increase in friction drag such that the resulting design would no longer be optimal. To address this, starting from the lift-to-drag ratio maximized result, trim-constrained drag minimization is performed at the altitude suggested by the lift-to-drag ratio maximization and at decrements of 2,000 ft with the target lift coefficient and Reynolds number adjusted accordingly. The altitude and design that provides the maximum lift-to-

Table 6.1: Optimized CTW performance at the start of cruise at their optimal altitude.

Design	Altitude [ft]	Weight [lb]	S [ft^2]	C_L [–]	C_D [–]	L/D [–]	D/q_∞ [ft^2]	Drag [lb]
CTW100-2	40,000	91,500	1,022	0.533	0.0265	20.1	27.1	4,552
CTW160-2	36,000	143,300	1,370	0.501	0.0247	20.3	33.8	7,059
CTW300-2	32,000	633,900	4,757	0.460	0.0189	24.3	90.0	26,086

drag ratio from these optimizations is taken as the optimum and presented below, indicated by the suffix '-2'. This procedure is performed for all of the CTWs, HWBs, and LFCs. This study is based upon aerodynamic performance considerations only and does not take into account the effects of altitude on engine performance, buffet, or operational considerations. At the crest of the L/D-vs-C_L curve, changes in L/D with C_L can be relatively small. Thus, while the altitudes determined below correspond to conditions closest to optimum, deviations in altitude can be permitted with only small reductions in the lift-to-drag ratio.

The performance at optimal altitude for the CTWs is shown in Table 6.1. The regional, narrow-body, and mid-size CTWs optimally cruise at 40,000, 36,000, and 32,000 ft, respectively. For the CTW100, the increase in cruise altitude of 4,000 ft corresponds to a 1.5% increase in L/D. The narrow-body CTW160-2's optimal altitude is 36,000 ft, the same as for the original studies. Finally, the CTW300-2 has an optimal altitude of 32,000 ft, which yields a lift-to-drag ratio increase of almost 4% relative to the CTW300-1 design at 36,000 ft.

Due to their low wing loading, all of the HWBs, except for the HWB300F, have an optimal altitude greater than the original 36,000 ft, as shown in Table 6.2. The change in altitude for the smaller classes is substantial, at up to 10,000 ft for the regional-class HWB, which gives up to almost an 8% increase in the lift-to-drag ratio. While a substantial performance improvement is achieved just by cruising at a higher altitude, the accompanying considerations such as engine size, buffet, and structural and operational considerations, may make such an altitude impractical. As expected, for each class, the HWBs cruise higher than their CTW counterpart. The resulting shapes are shown in Figure 6.1. Comparing these to the shapes shown in Figures 4.7(a)-4.10(a), it can be seen that the optimizer has increased the wing size for those HWBs cruising at the higher altitudes so as to mitigate the increase in induced drag associated with the higher altitude while increasing the parasitic drag such that the two components are equal.

Due to their higher wing loading than the HWBs, the change in altitude for the LFCs is less dramatic, with a correspondingly smaller change in the lift-to-drag ratio. The change in the lift-to-drag ratio for the LFC100-2 is less than 4%, that of the LFC160-2 is less than

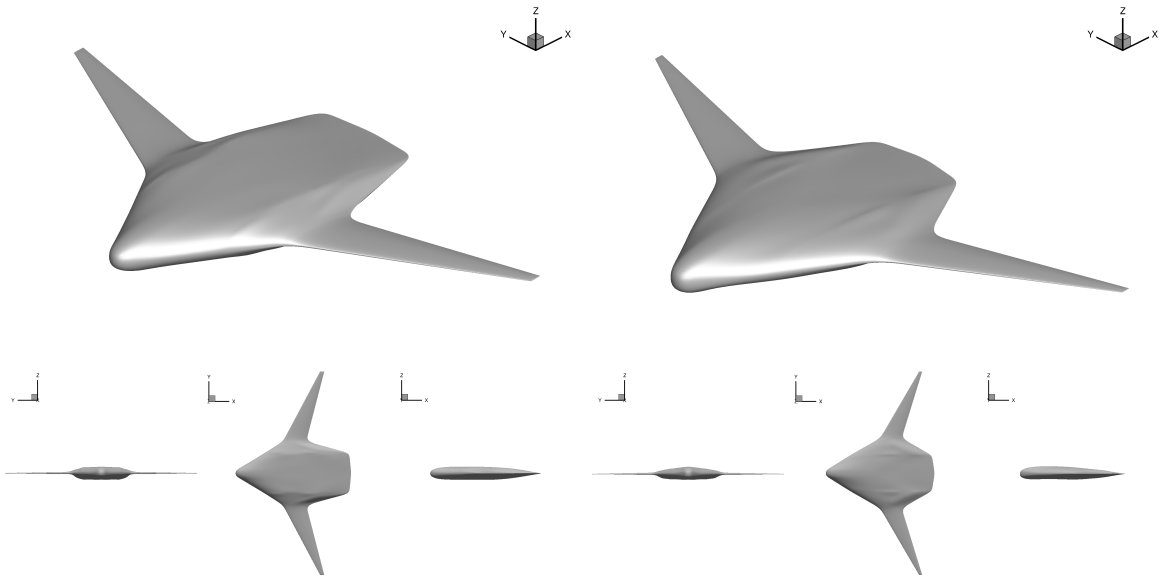

(a) HWB100D-2 at 46,000 ft

(b) HWB160D-2 at 44,000 ft

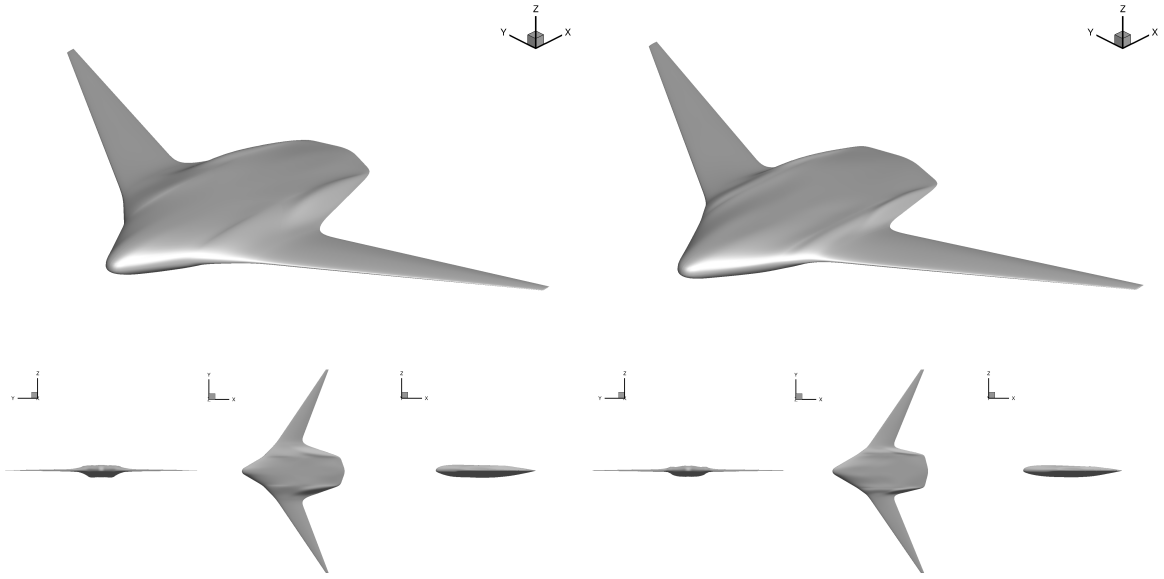

(c) HWB220E-2 at 40,000 ft

(d) HWB300F-2 at 34,000 ft

Figure 6.1: Optimized HWBs at their optimal altitudes.

Table 6.2: Optimized HWB performance at the start of cruise at their optimal altitude. Drag is that at the beginning of the cruise segment, and is given relative to the optimized CTW in each class at its optimal altitude.

Design	Altitude [ft]	Weight [lb]	S [ft^2]	C_L [–]	C_D [–]	L/D [–]	D/q_∞ [ft^2]	Drag [lb]
HWB100D-2	46,000	106,600	2,972	0.284	0.0115	24.8	34.1	4,298
HWB160D-2	44,000	185,300	4,800	0.273	0.0103	26.6	49.2	6,966
HWB220E-2	40,000	355,400	6,629	0.304	0.0104	29.1	69.2	12,213
HWB300F-2	34,000	700,500	9,356	0.288	0.0096	30.0	89.9	23,350

Table 6.3: Optimized LFC performance at the start of cruise at their optimal altitude. Drag is that at the beginning of the cruise segment, and is given relative to the optimized CTW in each class at its optimal altitude.

Design	Altitude [ft]	Weight [lb]	S [ft^2]	C_L [–]	C_D [–]	L/D [–]	D/q_∞ [ft^2]	Drag [lb]
LFC100-2	44,000	104,100	2,803	0.267	0.0107	24.9	30.1	4,181
LFC160-2	42,000	180,500	4,575	0.253	0.0096	26.4	43.9	6,837
LFC220-2	38,000	356,900	6,375	0.288	0.0099	29.0	63.3	12,307

3%, and that of the LFC220-2 is negligible. The performance is summarized in Table 6.3, and the resulting fuel burn performance is discussed in the following section. As with the HWBs, the wing area increases relative to the designs optimized at 36,000 ft, as shown in Figure 6.2.

The breakdown of friction and pressure drag for each design is shown in Figures 6.3 and 6.4 for cruise at 36,000 ft and optimal altitude, respectively. At 36,000 ft, both the regional and narrow-body-class HWBs have higher friction drag due to their higher wetted areas, and lower pressure drag due to their higher spans. In the same classes, the LFCs provide further reductions in pressure drag, while simultaneously reducing friction drag compared to the HWBs, thus yielding the drag benefit shown previously. The wide-body-class HWB has both lower friction and pressure drag relative to the CTW.

At the optimal altitudes, the friction drag is lower than the pressure drag for each design. The maximum lift-to-drag ratio is achieved when the induced and parasitic drag are equal, which is attainable if the friction drag is less than the pressure drag since parasitic drag is the friction drag plus the form drag portion of pressure drag.

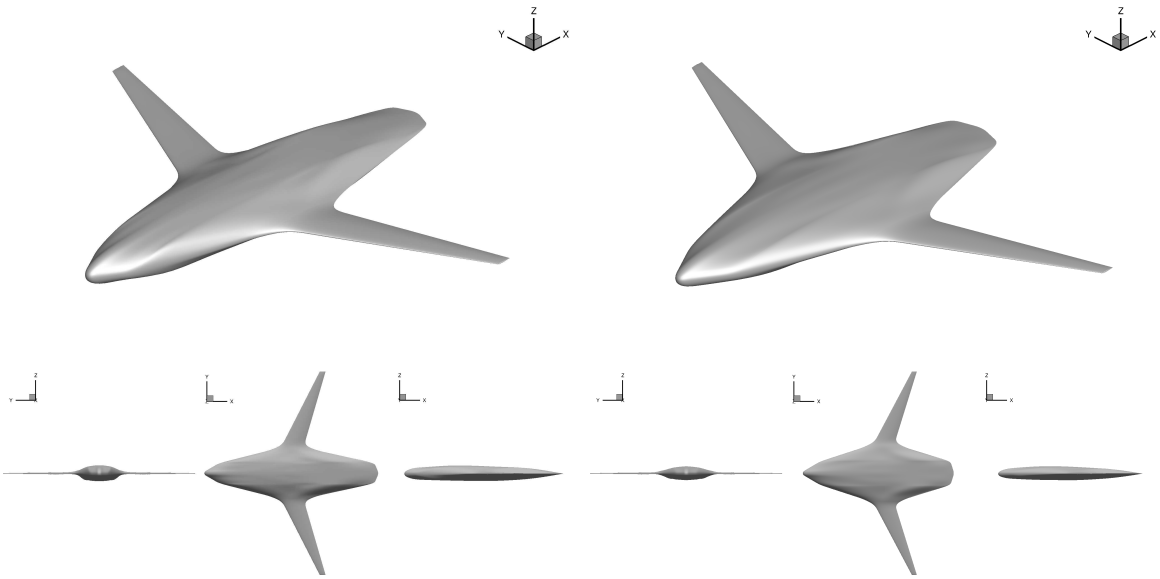

(a) LFC100-2 at 44,000 ft

(b) LFC160-2 at 40,000 ft

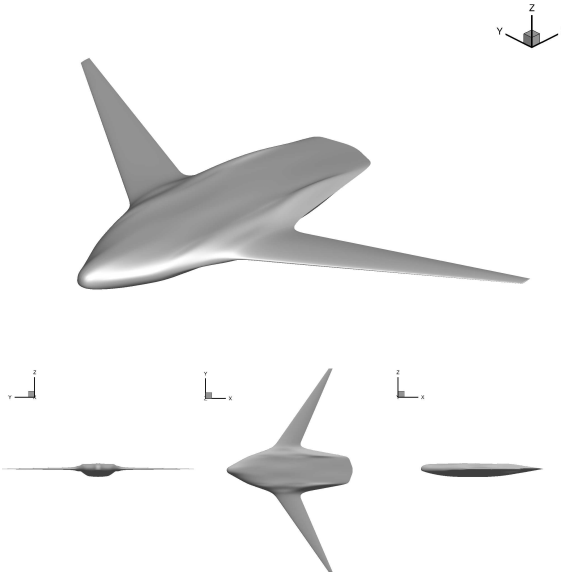

(c) LF220-2 at 38,000 ft

Figure 6.2: Optimized LFCs at their optimal altitudes.

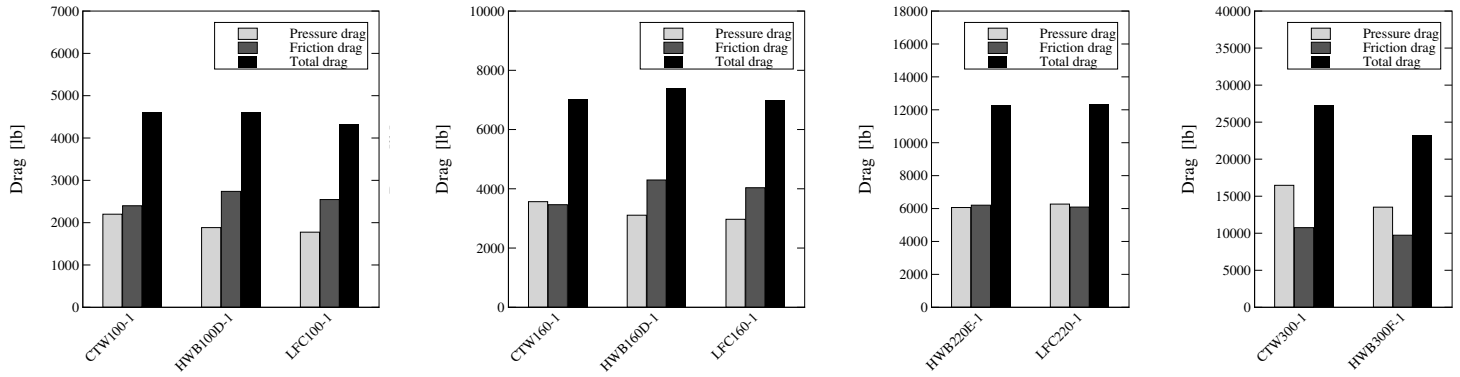

(a) Regional (b) Narrow-body (c) Mid-size (d) Wide-body

Figure 6.3: Drag breakdown for each concept across the range of classes, cruising at 36,000 ft.

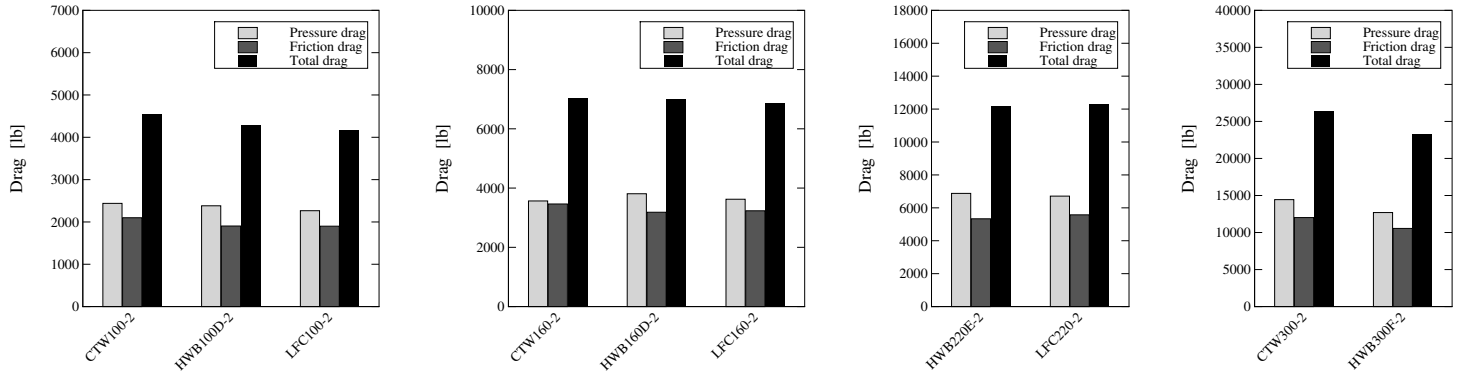

(a) Regional (b) Narrow-body (c) Mid-size (d) Wide-body

Figure 6.4: Drag breakdown for each concept across the range of classes, cruising at their optimal altitudes.

At the optimal altitudes, the friction drag of the HWB and LFC designs is lower than the CTW for each class. This is not a consequence of reduced wetted area, but rather differences in the dynamic pressure arising from the different altitudes for each design. For those designs which have an optimal altitude greater than 36,000 ft, the wetted area increases slightly relative to the optimized designs at 36,000 ft, and the friction drag coefficient increases due to Reynolds number effects.

Since the changes in the optimal aerodynamic performance are greatest for the HWBs and LFCs, all of the HWBs and LFCs now exhibit a benefit compared to the CTWs, as will be discussed in the following section. However, the higher cruise altitudes for the HWBs and LFCs may present challenges due to buffet, engine and pressure vessel sizing, and, for the regional and narrow-body-classes, the practicality of having to climb to such a high altitude for a short range mission.

6.2 Performance Comparison

This work is driven by the desire to reduce fuel burn, and thus the environmental impact of air travel. To this end, the fuel burn reduction potential of each design is presented in addition to the lift-to-drag ratio. Assuming a cruise-climb profile for the duration of the cruise segment of the mission, cruise fuel burn is computed using the Breguet range equation through Equation 1.3, where W_0 is the non-fuel portion of the weight of the aircraft at the start of the cruise segment, i.e. the weight at the end of cruise.[1] The variation in the lift-to-drag ratio and cruise fuel burn with aircraft size is shown in Figures 6.5 and 6.6 for the three concepts when cruising at 36,000 ft and their optimal altitudes, respectively.

The aerodynamic efficiency, i.e. lift-to-drag ratio, for each HWB is higher than its CTW counterpart, with the largest benefit for the HWB300F-1 at over 28%. However, for each class, the HWBs are heavier than their CTW counterpart, such that not all of the aerodynamic efficiency benefits are realized in terms of drag, and hence fuel burn, reductions. The regional-class HWB100D-1 has higher drag and burns slightly more fuel than the CTW100-1, while the narrow-body HWB160D-1 has a significant drag and fuel burn penalty, and the wide-body HWB300F-1 burns 10.9% less fuel than the CTW300-1. This is consistent with the trends seen by Nickol [70]. His study found that the HWBs offered higher lift-to-drag

[1] Temperature is constant for the ISA between 36,000 ft and 64,000 ft. Thus, for designs which have an optimal altitude above 36,000 ft, the cruise speed and TSFC remain unchanged at the fixed Mach number. For the wide-body designs which cruise below 36,000 ft, the change in cruise speed and TSFC resulting from the higher temperatures is accounted for in the fuel burn calculations. The change in TSFC is obtained using the temperature lapse rate scaling described by Mattingly et al. [3]

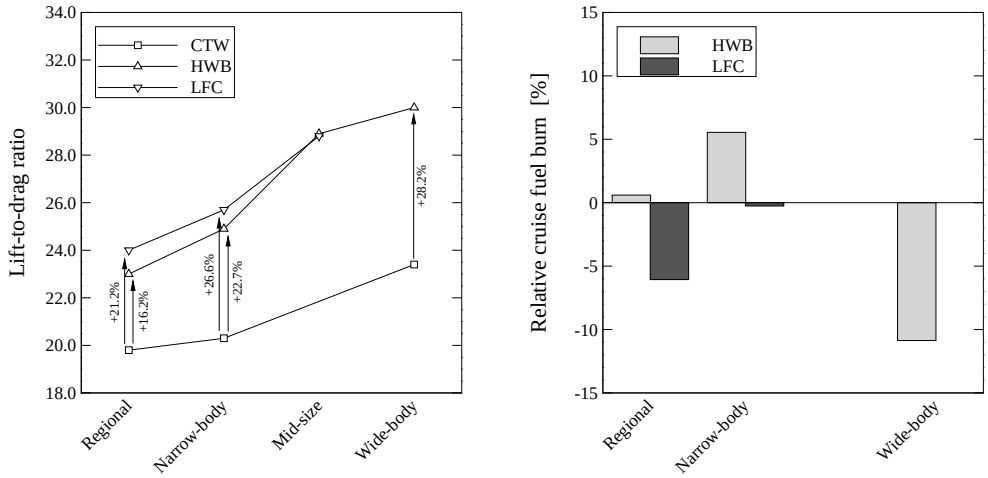

(a) Lift-to-drag ratio (b) Relative cruise fuel burn

Figure 6.5: The lift-to-drag ratio and relative cruise fuel burn across all aircraft classes at 36,000 ft. Fuel burn is given relative to that of the CTW for each class at 36,000 ft.

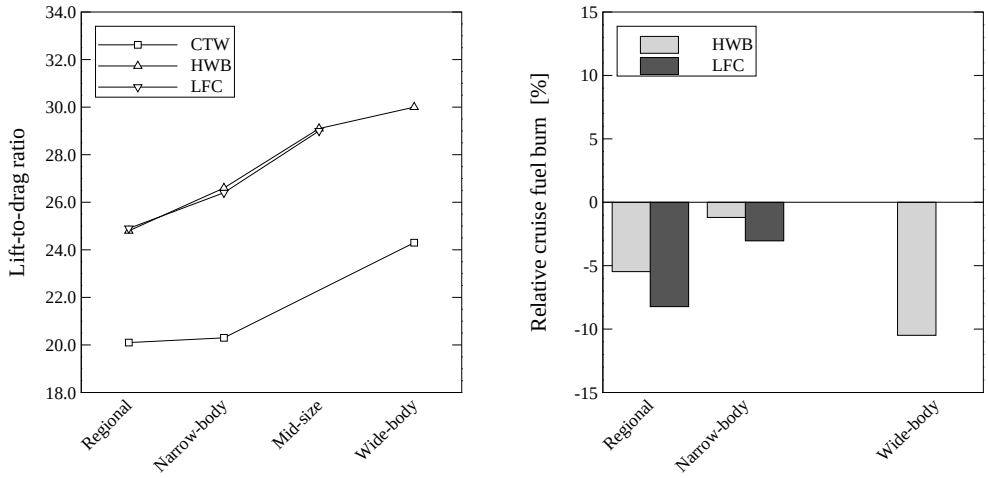

(a) Lift-to-drag ratio (b) Relative cruise fuel burn

Figure 6.6: The lift-to-drag ratio and relative cruise fuel burn across all aircraft classes at their optimal altitude. Fuel burn is given relative to that of the CTW for each class at its optimal altitude.

ratios across all classes, but the higher weight of the HWBs resulted in the regional and narrow-body-class HWBs burning more fuel than the CTWs. Note that the lift-to-drag ratio increases monotonically with size, but the relative fuel burn does not. This is a result of the narrow-body-class HWB having a higher relative weight compared to the CTWs than the other classes. The OEW of the HWB100D, HWB160D, and HWB300F is 24%, 43%, and 29% higher than the respective CTWs. This leads to the increased fuel burn of the

HWB160D-1. This same trend was observed by Nickol, where the relative OEW difference between the HWB and CTW in the narrow-body-class was over twice as large as for the other classes. Thus, while the HWBs offer lift-to-drag ratio advantages in all classes, reducing weight will be critical to making them more efficient than CTWs, particularly for the smaller classes. Allowing the designs to operate at their optimal altitude increases the lift-to-drag ratio enough that the smaller HWBs can produce a fuel burn reduction of 5.5% for the regional-class HWB and 1.2% for the narrow-body-class HWB; see Figure 6.6(b). The wide-body-class HWB burns 10.5% less fuel than the optimized CTW when both at their optimal altitudes, which is slightly less than the benefit at 36,000 ft due to the change in altitude, and hence lift-to-drag ratio, of the CTW.

The lift-to-drag ratio for all of the LFCs is up to over 4% higher than that of the equivalent HWBs, and 21-27% higher than the CTWs. The improved performance of the LFCs relative to the HWBs is largely a consequence of their lower wetted areas and higher wing loadings which allow them to be closer to their optimal lift-to-drag ratios at 36,000 ft. The LFC's higher aerodynamic efficiency, together with the lower weight compared to the HWBs, yields cruise fuel burn savings relative to both the HWBs and CTWs with the exception of the mid-size class. While neither the HWB100D-1 or HWB160D-1 showed a fuel burn benefit relative to the CTWs, the regional-class LFC burns 6.1% less fuel than the CTW, and the narrow-body-class LFC burns approximately the same amount as the CTW. This benefit increases to 8% and 3%, respectively, if the designs cruise at their optimal altitude. For the mid-size LFC and HWB, the performance is quite similar since the two concepts begin to converge at this size, while in the regional and narrow-body classes the LFCs burn 5.5-6.6% less fuel than the HWBs. The relative fuel burn of the mid-size HWB and LFC is not given in Figures 6.5(b) and 6.6(b) since there is no mid-size CTW reference aircraft.

For the smaller classes, particularly for the regional class, the LFC offers operational benefits compared to the HWB. First, for the regional-class, the LFC is able to fit within code 'C' gates currently used by regional aircraft while the HWB cannot. Secondly, the higher wing loading of the LFC compared to the HWB means it can operate closer to its optimal lift-to-drag ratio at lower altitudes as compared to the HWB.

A breakdown of the relative cruise fuel burn for all concepts and classes is summarized in Table 6.4 for both the nominal mission, and for a second, longer range mission, with the same payload, both at 36,000 ft. Throughout this work, only a nominal mission has been considered for each class. The fuel burn for a longer range mission is investigated to quantify the potential of the different concepts for missions for which the aerodynamic

Table 6.4: Fuel burn for each design, for both the nominal mission, and a second, longer range mission, given as both the absolute load, and relative to the optimized CTW in each class.

Class	Design	Fuel burn			
		[lb]	[%]	[lb]	[%]
		500 nmi		1,800 nmi	
Regional	CTW100-1	3,244	–	12,248	–
	HWB100D-1	3,263	+0.6	12,240	−0.1
	LFC100-1	3,047	−6.1	11,409	−6.8
		1,000 nmi		2,800 nmi	
Narrow-body	CTW160-1	9,474	–	28,249	–
	HWB160D-1	9,999	+5.5	29,465	+3.6
	LFC160-1	9,449	−0.3	27,802	−1.6
		3,000 nmi		6,000 nmi	
Mid-size	HWB220E-1	46,170	–	99,334	–
	LFC220-1	46,682	–	100,460	–
		6,000 nmi		8,600 nmi	
Wide-body	CTW300-1	151,614	–	231,503	–
	HWB300F-1	135,137	−10.9	203,374	−12.2

efficiency becomes a stronger factor for fuel burn. The range for the longer range mission is chosen to be the maximum range attainable with the same payload, as provided by the conceptual design tool for the baseline designs. It is assumed that the lift-to-drag ratio for the nominal mission at 36,000 ft is also attained for the longer range mission. Due to the higher fuel loads, this would require an increased ICA, which is not accounted for. As expected, the fuel burn benefit of the unconventional concepts is increased for the longer range missions due to their higher lift-to-drag ratios.

Chapter 7

Sensitivity and Feasibility Studies

As demonstrated in the previous chapters, the new LFC shows the potential to reduce fuel burn in the regional class. This chapter examines the implications of variations in weight, and of additional considerations such as trim and longitudinal static stability requirements on this concept in the regional class. The HWB100D is also considered in order to compare the relative impact of these requirements on the two concepts in this class. All of the studies in this chapter are performed at a cruise altitude of 36,000 ft.

7.1 Weight Sensitivity

There is large uncertainty in the center-body weight estimates for both the HWB and LFC designs, as well as the suitability of the low-fidelity weight models used for the airframe weight prediction. As shown in the previous sections, a portion of the improved aerodynamic efficiency of the unconventional configurations is negated by their higher weight, resulting in drag reductions relative to the CTW100-1 that are significantly less than the lift-to-drag benefits. Thus, a weight sensitivity study is conducted whereby the OEW of the HWB100D and LFC100 predicted by the low-fidelity models is perturbed by $\pm 10\%$. This perturbation is the same as that of Nickol's scaling study [70]. The CTW weights are assumed to be relatively accurate, as shown in Appendix A, and are thus not perturbed. The optimizations start from the optimized designs obtained previously, but with the new lift target. The resulting performance is shown in Table 7.1.

If the OEW has been over-predicted by the low-fidelity sizing tool by 10%, then both of the unconventional designs offer lower drag than the CTW100-1, up to almost 10% for the LFC100-1. Conversely, if the weight was under-predicted by 10% then only the LFC100-1 offers lower drag than the CTW100-1, although the savings is reduced to 2.2%. Thus, the

Table 7.1: Performance of the HWB100D-1 and LFC100-1 designs, and those with ±10% variability in OEW. Drag is given relative to the CTW100-1 reference aircraft.

Design	Relative drag [%]		
	Baseline OEW	OEW−10%	OEW+10%
HWB100D-1	+0.3	−2.5	+3.6
LFC100-1	−6.1	−9.6	−2.2

new LFC concept exhibits high enough aerodynamic efficiency such that, even in the face of still higher weight, it has lower drag than the CTW100-1 reference aircraft.

The HWB pressure vessel model of Bradley [121] is used for the center-body weight estimates for the LFC100 design. However, the cabin shape is significantly different than that for which the model was created. It is also possible that this centerbody layout would be better served by an elliptical or double-bubble type cross section. To address this possibility, the non-cylindrical center-body weight model is replaced with that for a cylindrical pressure vessel, so as to form an optimistic estimate and thus bracket the 'true' weight. This results in an OEW of 60,300 lbs and an MTOW of 106,300 lbs; compared to 71,100 lbs and 118,700 lbs, respectively, for the original LFC100. This brings the weight of the LFC100 down close to that of the CTW100. Trim-constrained drag minimization is performed with the weight at the start of cruise corresponding to this weight model, resulting in a drag reduction relative to the CTW100-1 of 11.2%.

Both the HWB and LFC concepts, particularly the LFC, offer higher aerodynamic efficiency than the CTW design. Minimizing structural weight as much as possible will thus be critical in obtaining the full aerodynamic potential of this concept. Recent work suggests that the weight of the non-cylindrical pressure vessel could likely be reduced through advanced structural design [21]. Thus, the structural weights assumed in this work will likely lead to conservative estimates for the performance of the unconventional configurations.

7.2 Effect of Trim Requirements

All of the designs have been optimized with a trim constraint, i.e. constraints on both lift and pitching moment. One of the challenges with the HWB designs is that the main lifting surface must also provide pitch trim. This section investigates the performance degradation caused by the imposition of the pitching moment constraint. To investigate this, the HWB100D and LFC100C configurations are optimized as in Chapter 4, but without the pitching moment

Table 7.2: Design performance without a pitching moment constraint. The constrained cases are included for reference. Drag is given relative to the CTW100-1.

Design	Weight [lb]	C_L [–]	C_D [–]	C_M [–]	L/D [–]	Relative drag [%]
HWB100D-1	106,600	0.186	0.0081	0.000	23.0	+0.3
HWB100D-3	106,600	0.187	0.0081	−0.012	23.0	+0.3
LFC100-1	104,100	0.191	0.0080	0.000	24.0	−6.1
LFC100-3	104,100	0.195	0.0081	−0.014	24.1	−6.5

constraint, and are referred to with the suffix '-3'. The sections of the unconstrained designs are largely similar to those of the constrained case; the wing sections are nearly identical, while those on the center-body dispense with any reflex. The primary change is the increased sweep of the transition region, where the transition sweep increases by 5° for the HWB100D-3, and by 3° for the LFC100C-3. The resulting performance is shown in Table 7.2, from which it can be seen that there is little-to-no performance degradation as a result of the pitching moment constraint. This small performance degradation is in agreement with the results of Le Moigne and Qin [74], however the differences between the sections for the constrained and unconstrained cases are less than those seen by Le Moigne and Qin.

7.3 Effect of Stability Requirements

While all of the designs are trimmed, only the CTW100-1 has a positive static margin, although no such constraint was included in the optimization. Both the HWB100D-1 and LFC100-1 have a margin greater than −5%, which could potentially be accepted through the use of an active stability system. However, certification challenges would exist with such a design. Thus, the performance impact of requiring a more positive static margin is investigated for the HWB100D-1 and LFC100-1 designs, which have −2.5% and −3.2% margins, respectively. Two trim-constrained drag minimization problems are performed for each design using the same formulation as before, but with the addition of 0% and +5% static margin constraints. The static margin constraint is calculated as $K_n = -\frac{\partial C_M}{\partial C_L} \approx -\frac{\Delta C_M}{\Delta C_L}$, via a finite-difference with respect to the angle-of-attack, with a step-size of $\Delta\alpha = 0.1°$. In addition, the CG location is now included as a design variable such that the optimizer can adjust it to find the optimal trade-off between the trim and static-margin constraints. It is allowed to vary by ±10% of the MAC about the point predicted by the low-fidelity models used for the previous cases. Changes in the CG location are taken into account in the static

Table 7.3: Design performance when subjected to a static margin constraint. The unconstrained cases are included for reference. Drag is given relative to the CTW100-1.

Design	Weight [lb]	Δx_{CG}[1] [% MAC]	K_n [% MAC]	C_L [–]	C_D [–]	L/D [–]	Relative drag [%]
HWB100D-1	106,600	—	−2.5	0.186	0.0081	23.0	+0.3
HWB100D-4	106,600	−1.3	0.0	0.186	0.0081	23.0	+0.3
HWB100D-5	106,600	−6.2	+5.0	0.186	0.0082	22.8	+1.2
LFC100-1	104,100	—	−3.2	0.191	0.0080	24.0	−6.1
LFC100-4	104,100	−2.5	0.0	0.191	0.0080	23.8	−5.4
LFC100-5	104,100	−7.7	+5.0	0.190	0.0083	22.8	−1.2

[1] Change in CG location. Negative values correspond to forward movement of the CG.

margin calculation through the calculation of C_M, which uses the current CG location at each iteration. Fixing the CG can potentially result in an unrealistic performance penalty due to the reduced freedom available to the optimizer, and it is postulated that the CG could be moved within ±10% of the MAC by proper distribution of systems and fuel. The CG is not included as a design variable for the previous cases as it would simply be moved to its aft bound to minimize trim drag. The resulting performance of the optimized designs is shown in Table 7.3. The suffix '-4' indicates cases with the 0% static margin constraint, and '-5' denotes those cases with the +5% constraint.

In each case the optimizer moves the CG forward with the increasingly positive static margin requirement. This is accompanied by forward movement of the centers of pressure on the center-body to maintain trim, as shown in Figures 7.1 and 7.2. For the HWB100D-4, the 0% static margin is obtained by moving the CG forward by 1.3% of the MAC, together with a slight aft movement of the wing, and hence aerodynamic centers. For the LFC100-4 the 0% static margin is satisfied primarily by forward movement of the CG and some tailoring of the sections near the wing tip to move the local aerodynamic centers aft. The HWB100D-4 is able to achieve the required static margin with no performance penalty, while the LFC100-4 design sees a slight performance decrement such that its drag reduction relative to the CTW100-1 is reduced from 6.1% to 5.4%. For the +5% static margin cases, the required margin is obtained by moving the CG forward by about 5% of the MAC relative to the 0% margin cases, with an associated forward movement of the centers of pressure on the center-bodies to maintain trim for both the HWB100D-5 and LFC100-5. For the HWB100D-5, the resulting performance penalty is such that this design now has 1.2% higher drag than the CTW100-1. The drag increase for the LFC100-5 causes the drag reduction relative to the CTW100-1 to be reduced to 1.2%. As can be seen from Figures 7.1 and 7.2, for all cases

except the LFC100C-5, the aerodynamic centers on the outboard wing are near the quarter chord location as one would expect. For the LFC100C-5, the aerodynamic centers are moved aft of the quarter chord through tailoring of the sectional pressure distribution. This is most pronounced between 70% and 90% of the span, at which point said pressure tailoring results in a region of separated flow as indicated in the inset of Figure 7.4(b). For all of the designs, the aerodynamic centers on the wing are ahead of the centers of pressure such that the wing is destabilizing, and vice versa for the center-body. To summarize, for the HWBs, there is no drag penalty to increase the static margin to zero and a small penalty to reach +5%. In contrast, the new LFC shape displays a small penalty for the zero margin and a substantial drag penalty for the large positive static margin. Hence the proposed LFC concept is most advantageous if relaxed static stability can be accepted.

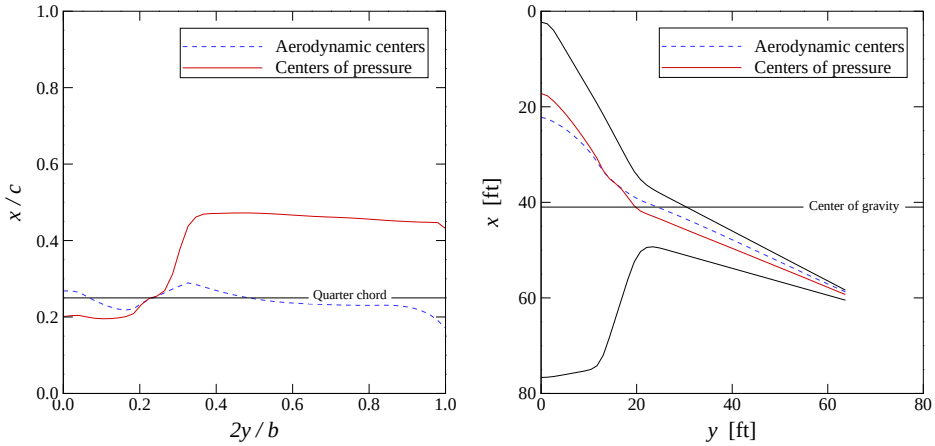

(a) HWB100D-1

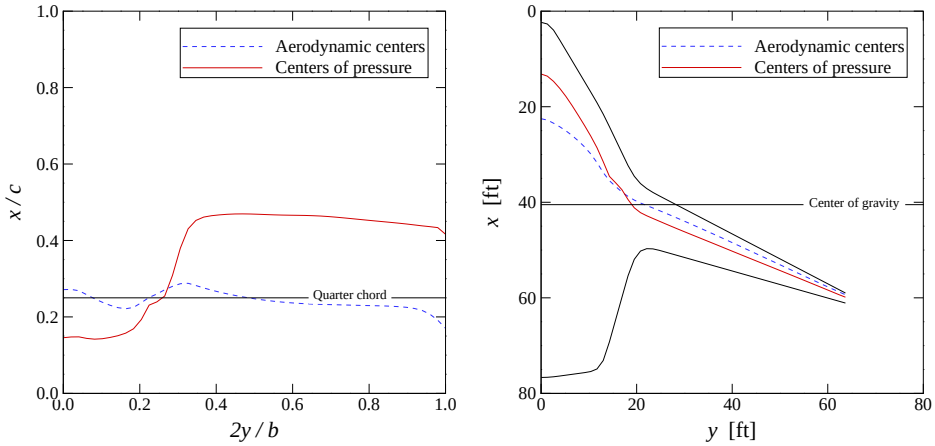

(b) HWB100D-4

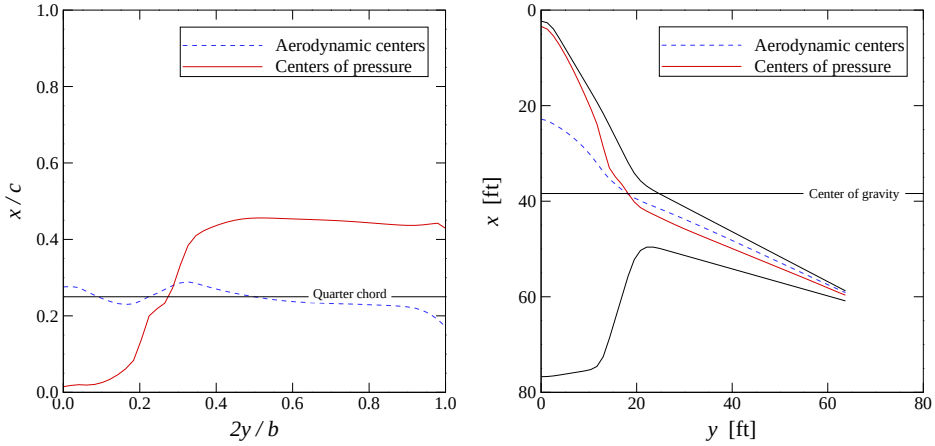

(c) HWB100D-5

Figure 7.1: Spanwise distribution of the centers of pressure and aerodynamic centers for each HWB100D design.

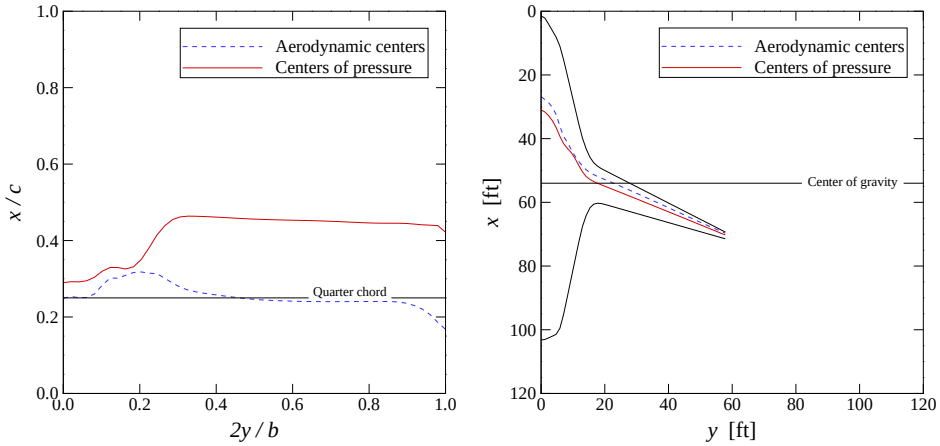

(a) LFC100-1

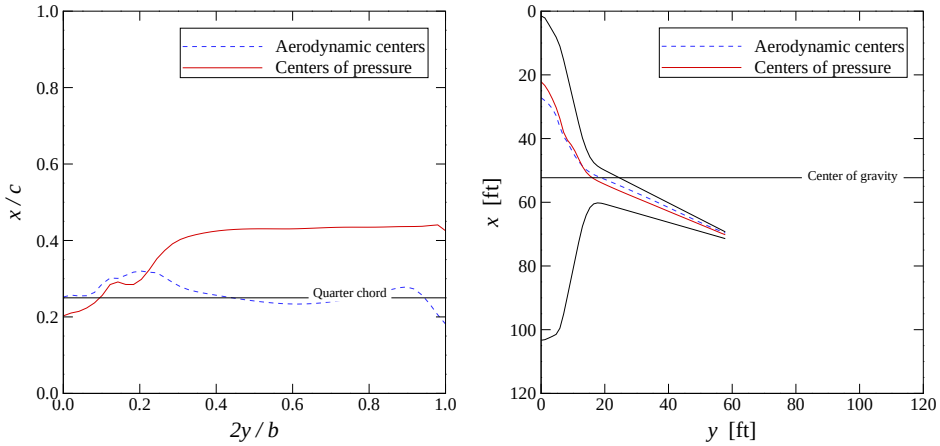

(b) LFC100-4

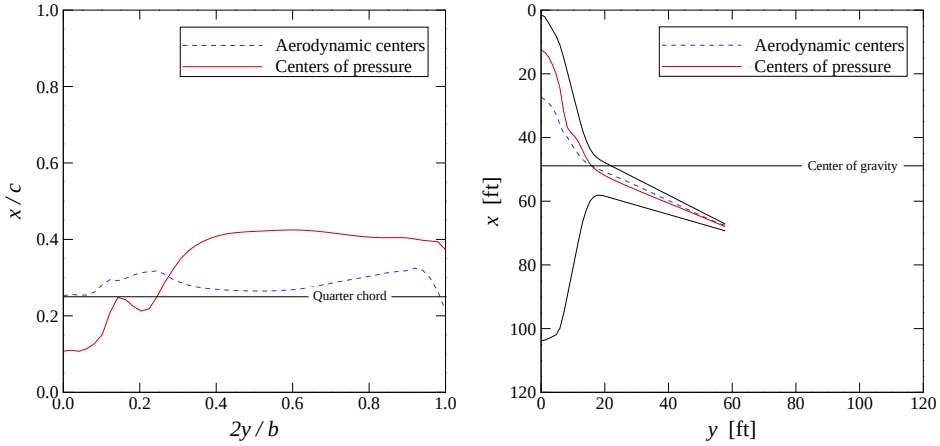

(c) LFC100-5

Figure 7.2: Spanwise distribution of the centers of pressure and aerodynamic centers for each LFC100 design.

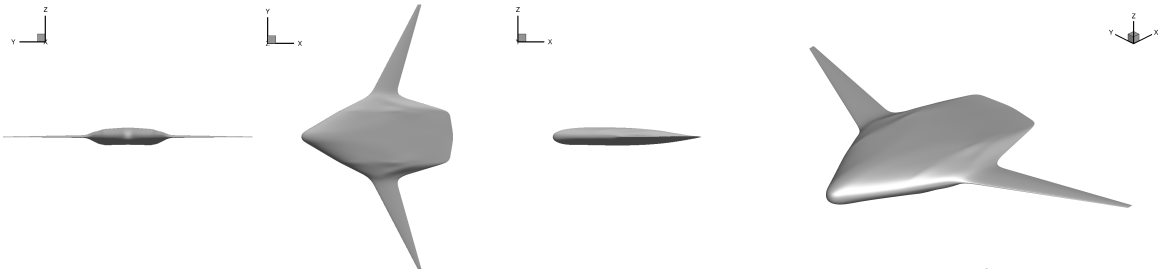

(a) Optimized geometry

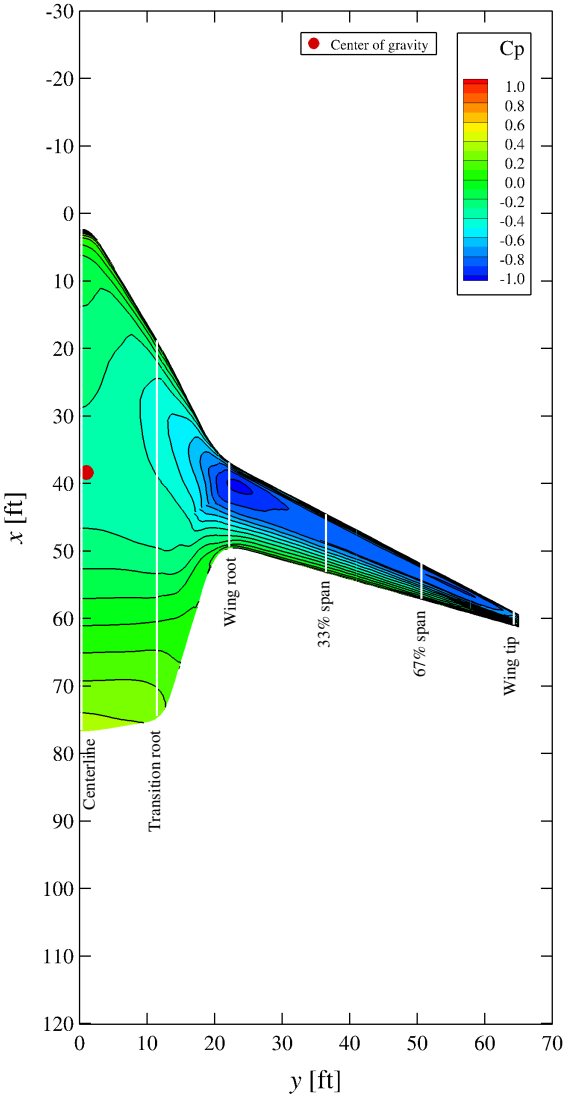

(b) Surface pressure distribution

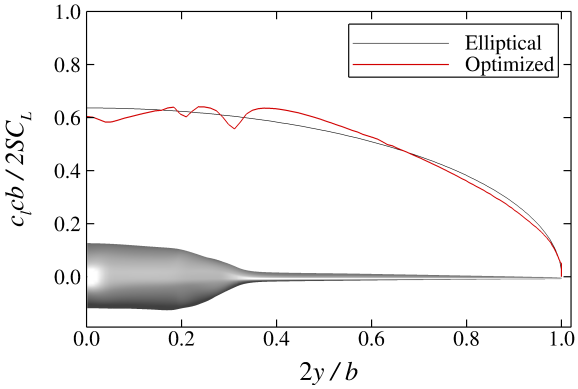

(c) Spanwise lift distribution

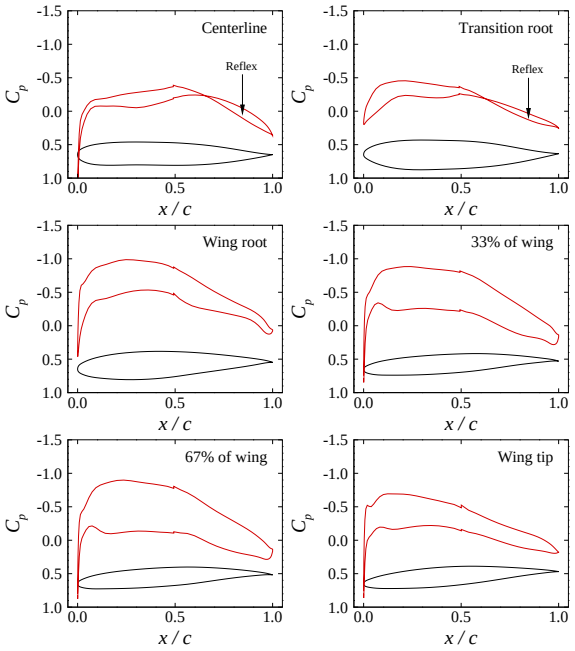

(d) Sectional pressure distributions

Figure 7.3: The optimized HWB100D-5 design.

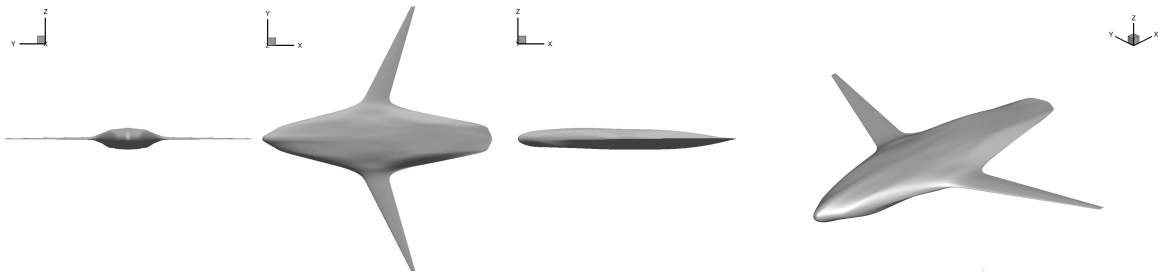

(a) Optimized geometry

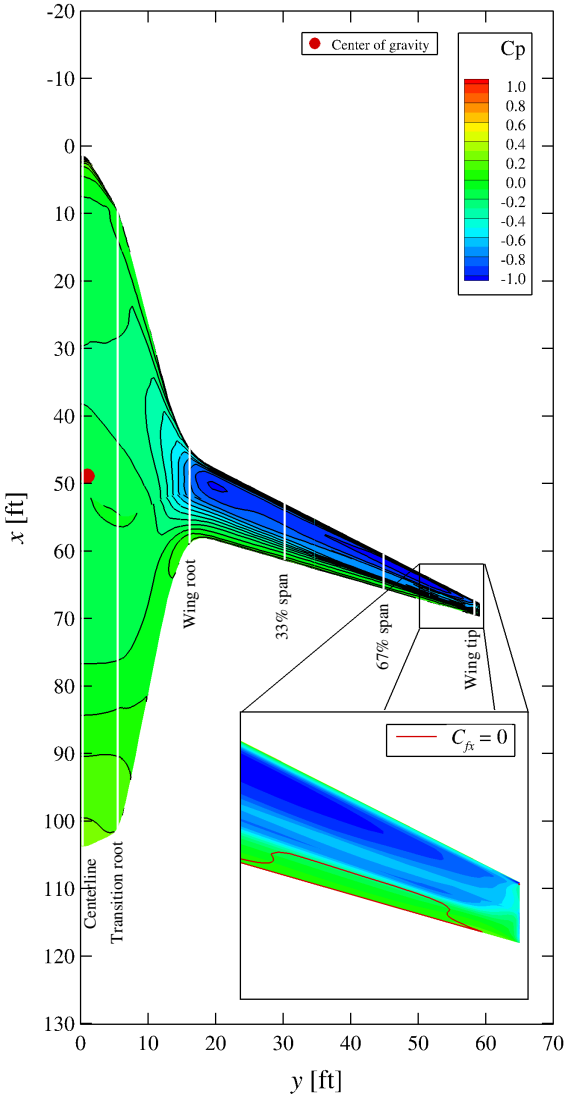

(b) Surface pressure distribution, including detail showing separated flow identified by the contour of $C_{f_x} = 0$

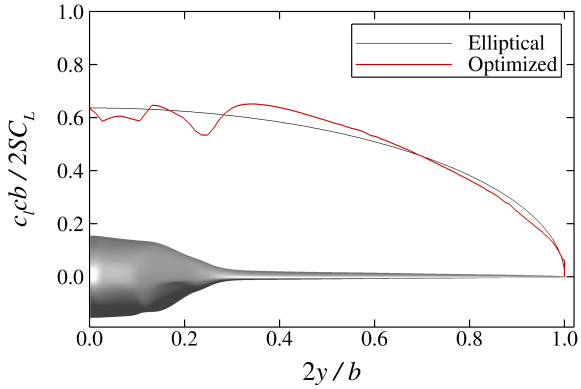

(c) Spanwise lift distribution

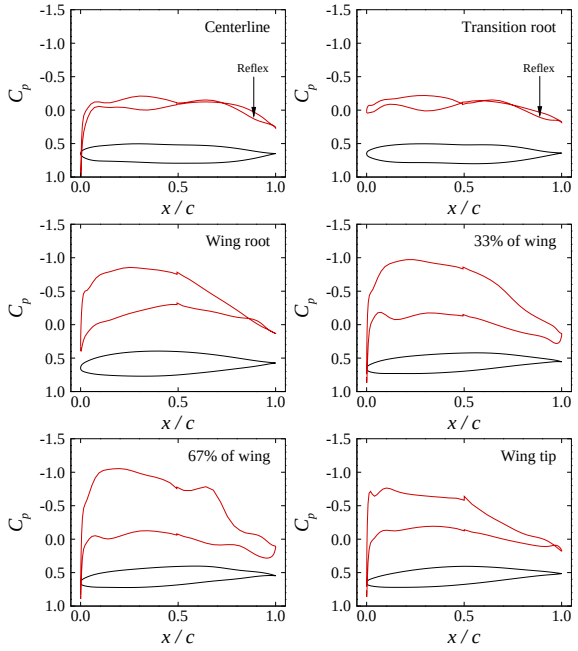

(d) Sectional pressure distributions

Figure 7.4: The optimized LFC100-5 design.

Chapter 8

Conclusions, Contributions, and Recommendations

8.1 Conclusions

This thesis aimed to:

1. examine how the efficiency of the HWB concept relative to CTWs scales with aircraft size, including down to smaller classes of aircraft for which this concept is often not considered, and the potential of ASO to yield HWB designs that offer performance benefits in these smaller classes;
2. investigate alternative configurations which may be more efficient than HWB aircraft, and how the optimal shape changes with aircraft size.

In order to achieve these objectives, high-fidelity aerodynamic shape optimization based on the RANS equations was applied to the aerodynamic design of conventional aircraft, hybrid wing-bodies, and a new lifting-fuselage configuration. Using RANS-based ASO, while more computationally expensive than linear or Euler-based optimizations, allows for accurate determination of both inviscid and viscous effects, which are critical for HWB design, since the center-body, a large source of parasitic drag, is also responsible for generation of a significant portion of the total lift. The use of RANS-based ASO also permits the use of more geometric freedom, such as variations in chord distribution and wing area, since all drag components are captured and the optimizer can thus trade various types of drag so as to produce a design with the lowest total drag.

In order to investigate the correlation of HWB performance with size, a range of HWBs, including regional, narrow-body, mid-size, and wide-body classes were considered. Conven-

tional tube-and-wing designs for the regional, narrow-body, and wide-body classes were similarly optimized and serve as performance references for the unconventional configurations. The regional and narrow-body-class HWBs provide no drag or fuel burn savings compared to the CTWs. The wide-body HWB provides an almost 11% cruise fuel burn reduction relative to the wide-body CTW. All of these designs were assumed to operate at 36,000 ft. When allowed to operate at the altitude corresponding to the maximum lift-to-drag ratio, the regional-class HWB provides a 5.5% reduction in cruise fuel burn, the narrow-body-class HWB provides a marginal reduction, and the wide-body HWB's advantage is reduced slightly to 10.5% due to the change in altitude of the reference CTW aircraft.

The smaller optimized HWBs had more wetted area than their CTW counterparts. While not unexpected, the reduction of wetted area is one of the key drivers of the HWB concept, and one of the reasons the smaller HWBs did not provide any drag reductions. To address this, exploratory aerodynamic shape optimization, that is, optimizations with increased geometric freedom, were performed in order to more thoroughly explore the potential design space to see if there is an HWB configuration which can produce improved performance, particularly for smaller aircraft. This led to the development of the lifting-fuselage configuration (LFC). This configuration consists of a lifting center-body which is more slender than that of the HWBs, with more distinct wings. This exploration was performed for each class, which resulted in a distinct trend in optimal shape with aircraft size. The smaller aircraft, including the regional and narrow-body classes, have the slender fuselage of the LFC, while the larger sizes transitioned back to the HWB shape for the largest class. The spectrum of shapes between LFC and HWB is primarily driven by the packaging of the fuselage/center-body so as to produce minimum wetted area. Based upon these explorations, new LFC configurations were developed and optimized. The regional-class LFC has 6% lower cruise fuel burn than the CTW, the narrow-body-class LFC has a marginal fuel burn reduction, and these increase to 8% and 3%, respectively, when allowed to cruise at their optimal altitudes.

All of the HWBs and LFCs have higher aerodynamic efficiency, i.e. higher lift-to-drag ratios, than their CTW counterparts, but the predicted increased weight negates some of the aerodynamic benefit. All of the studies used existing technology. Investigations of the impact of weight uncertainty showed that a 10% reduction in OEW could lead to a 10% drag savings for the regional-class LFC relative to the CTW, and the HWB would then become competitive with the CTW in this class.

Since one of the challenges with the HWB and LFC concepts is longitudinal trim and stability due to the absence of an empennage, the effect of requiring trim and a given static

margin was investigated for the regional-class HWB and LFC designs. The trim requirement was found to be relatively benign, with little resulting performance degradation. The imposition of a 5% static margin requirement was found to incur a 1-5% drag penalty, however a neutrally stable, i.e. 0% static margin, aircraft was found to have a greatly reduced drag penalty, such that the LFC would still have lower drag and fuel burn than the equivalent CTW.

8.2 Contributions

The main contributions of this work can be broken down into three categories.

1. Demonstration of the scaling behaviour of HWB aircraft

Using high-fidelity analysis and optimization, it was shown that HWB aircraft do not offer a significant drag benefit for regional and narrow-body-class aircraft. For these sizes, no wetted area reduction is achieved relative to CTW designs, although they are more aerodynamically efficient due to their larger span. For larger classes, HWBs do offer reduced drag and fuel burn relative to CTW designs.

2. Novel application of exploratory aerodynamic shape optimization to develop more efficient regional-class aircraft

Through a problem formulation selected so as to address the shortcomings of the HWB concept in the smaller classes, exploratory aerodynamic shape optimization with significant geometric freedom led to the development of a new, more efficient configuration.

3. A proposed lifting-fuselage configuration for more efficient regional-class aircraft

This configuration maintains the all-lifting nature of the HWB concept, but allows for reduced wetted area compared to equivalent HWBs. It was shown that there is a continuum in optimal aircraft configuration, with the LFC concept being optimal for the smaller classes, and transitioning to the HWB for the larger classes. This new LFC concept was shown to be more aerodynamically efficient than both the CTW and HWB aircraft across all the classes, and allows for a reduction in cruise fuel burn of up to 8% relative to equivalent CTW aircraft for the regional class when using existing technology.

In addition, the development of the geometry control system described in Section 2.1.3 forms a contribution to the aerodynamic shape optimization framework used in this work.

8.3 Recommendations

The following areas need to be addressed to further establish the viability of both the HWB and LFC concepts.

Suitability for other markets: As this work was restricted to commercial aircraft, nothing smaller than a regional aircraft was considered. With the LFC's improved performance for small aircraft demonstrated, its suitability for business-class aircraft should also be considered.

Improved weight estimation: Uncertainty in the structural weight of both the HWB and LFC concepts leads to uncertainty in their aerodynamic performance. High-fidelity structural sizing is needed to establish more accurate weight estimates, particularly for the center-body.

Aerostructural optimization: In this work, the HWB and LFC spans were determined either via a low-fidelity argument or based upon gate limits. However, since span is such a critical parameter for aerodynamic performance, a high-fidelity, multidisciplinary optimization which could capture the trade-offs in weight and aerodynamic performance associated with span could potentially allow for both further performance improvements, as well as more confidence in the final design.

Multipoint optimization: This work examined performance at cruise alone. Features of the HWB and LFC concept, such as their low wing loading, could yield even more substantial performance improvements in other parts of the flight envelope, such as field performance. Multipoint optimization including a wider range of operating conditions would serve to establish a block fuel burn benefit, instead of simply cruise fuel burn. Any performance gains in these other conditions would particularly benefit the smaller aircraft which spend more time in these conditions.

Operating condition optimization: All of the optimizations performed in this thesis used a single cruise speed for each class, typical of that used for CTW missions. However, the low wing loading of the HWB and LFC concepts is likely to make operation at higher Mach numbers feasible. This would reduce block times and hence operational costs, and could be a key advantage of these concepts.

Stability and control: This work focused on trim at cruise, with some consideration of longitudinal static stability. Stability and control, particularly at low-speed, will be challenging due to the absence of an empennage. Optimal methods of control, and their cruise drag impact, could be investigated as part of an ASO study.

References

[1] Lee, D. S., Pitari, G., Grewe, V., Gierens, K., Penner, J. E., Petzold, A., Prather, M. J., Schumann, U., Bais, A., Berntsen, T., Iachetti, D., Lim, L. L., and Sausen, R., "Transport impacts on atmosphere and climate: Aviation," *Atmospheric Environment*, Vol. 44, No. 37, 2010, pp. 4678–4734.

[2] Stocker, T. F., Qin, D., Plattner, G. K., Tignor, M., Allen, S. K., Boschung, J., Nauels, A., Xia, Y., Bex, V., and Midgley, P., editors, *IPCC, 2013: Climate Change 2013: The Physical Science Basis. Contribution of Working Group I to the Fifth Assessment Report of the Intergovernmental Panel on Climate Change*, Cambridge University Press, Cambridge, United Kingdom and New York, NY, USA.

[3] Mattingly, J. D., Heiser, W. H., and Pratt, D. T., *Aircraft Engine Design*, American Institute of Aeronautics and Astronautics, 2nd ed., 2002.

[4] Gern, F. H., Gundlach, J. F., Ko, A., Naghshineh-Pour, A., Sulaeman, E., Tetrault, P.-A., Grossman, B., Kapania, R. K., Mason, W. H., Schetz, J. A., and Haftka, R. T., "Multidisciplinary Design Optimization of a Transonic Commercial Transport with a Strut-Braced Wing," *1999 World Aviation Conference*, 1999-01-5621, San Francisco, CA, October 1999.

[5] Bradley, M. K. and Droney, C. K., "Subsonic Ultra Green Aircraft Research: Phase I Final Report," Tech. Rep. NASA/CR-2011-216847, National Aeronautics and Space Administration, 2011.

[6] Gagnon, H. and Zingg, D. W., "Euler-Equation-Based Drag Minimization of Unconventional Aircraft Configurations," *Journal of Aircraft*, Vol. 53, No. 5, 2016, pp. 1361–1371.

[7] Drela, M., "Development of the D8 Transport Configuration," *29th AIAA Applied Aerodynamics Conference*, AIAA-2011-3970, Honolulu, HI, June 2011.

[8] "Lockheed Martin ERA N+2 Advanced Vehicle Concept Results," *50th AIAA Aerospace Sciences Meeting and Exhibit*, Nashville, TN, January 2012, (Presentation).

[9] Gallman, J. W., Smith, S. C., and Kroo, I. M., "Optimization of Joined-Wing Aircraft," *Journal of Aircraft*, Vol. 30, No. 6, 1993, pp. 597–905.

[10] Frediani, A., "The Prandtl Wing," *VKI lecture series on Innovative Configurations and Advanced Concepts for Future Civil Aircraft*, June 2005.

[11] Gagnon, H. and Zingg, D. W., "Aerodynamic Optimization Trade Study of a Box-Wing Aircraft Configuration," *Journal of Aircraft*, Vol. 53, No. 4, 2016, pp. 971–981.

[12] Kroo, I. M., Gallman, J. W., and Smith, S. C., "Aerodynamic and Structural Studies of Joined-Wing Aircraft," *Journal of Aircraft*, Vol. 28, No. 1, 1991, pp. 74–81.

[13] Liebeck, R. H., "Design of the Blended Wing Body Subsonic Transport," *Journal of Aircraft*, Vol. 41, No. 1, 2004, pp. 10–25.

[14] Mody, P. C., Sato, S., Hall, D. K., de la Rosa Blanco, E., and Hileman, J. I., "Conceptual Design of an N+3 Hybrid Wing Body Subsonic Transport," *28th AIAA Applied Aerodynamics Conference*, AIAA-2010-4812, Chicago, IL, June 2010.

[15] Raymer, D. P., *Aircraft Design: A Conceptual Approach*, American Institute of Aeronautics and Astronautics, 5th ed., 2012.

[16] Mukhopadhyay, V., Sobieszczanski-Sobieski, J., Kosaka, I., Quinn, G., and Vanderplaats, G. N., "Analysis, Design, and Optimization of Noncylindrical Fuselage for Blended-Wing-Body Vehicle," *Journal of Aircraft*, Vol. 41, No. 4, 2004, pp. 925–930.

[17] Mukhopadhyay, V., "Hybrid-Wing-Body Pressurized Fuselage, Modelling, Analysis, and Design for Weight Reduction," *53rd AIAA/ASME/ASCE/AHS/ASC Structures, Structural Dynamics and Materials Conference*, AIAA-2012-1999, Honolulu, HI, 2012.

[18] Velicki, A., Yovanof, N., Baraja, J., Linton, K., Li, V., Hawley, A., Thrash, P., DeCoux, S., and Pickell, R., "Damage Arresting Composites for Shaped Vehicles - Phase II Final Report," Tech. Rep. NASA/CR-2011-216880, The Boeing Company, Phantom Works, 2011.

[19] Li, V. and Jegley, D. C., "PRSEUS Structural Concept Development," *52nd Aerospace Sciences Meeting*, AIAA-2014-0259, National Harbor, MD.

[20] Jegley, D. C. and Velicki, A., "Development of the PRSEUS Multi-Bay Pressure Box for a Hybrid Wing Body Vehicle," *56th AIAA/ASCE/AHS/ASC Structures, Structural Dynamics, and Materials Conference*, AIAA-2015-1871, Dallas, TX, 2015.

[21] Mukhopadhyay, V. and Sorokach, M. R., "Composite Structure Modeling and Analysis of Advanced Aircraft Fuselage Concepts," *AIAA Modeling and Simulation Technologies Conference*, AIAA-2015-3096, Dallas, TX, 2015.

[22] Etkin, B. and Reid, L. D., *Dynamics of Flight: Stability and Control*, John Wiley and Sons, 3rd ed., 1995.

[23] Sargeant, M. A., Hynes, T. P., Graham, W. R., Hileman, J. I., Drela, M., and Spakovszky, Z. S., "Stability of Hybrid-Wing-Body Aircraft with Centerbody Leading-Edge Carving," *Journal of Aircraft*, Vol. 47, No. 3, 2010, pp. 970–974.

[24] Cook, M. V. and de Castro, H. V., "The Longitudinal flying Qualities of a Blended-Wing-Body Civil Transport Aircraft," *The Aeronautical Journal*, Vol. 108, No. 1080, 2004, pp. 75–84.

[25] Garmendia, D. C., Chakraborty, I., and Mavris, D. N., "Method for Evaluating Electrically Actuated Hybrid Wing-Body Control Surface Layouts," *Journal of Aircraft*, Vol. 52, No. 6, 2015, pp. 1780–1790.

[26] Chhabra, R., Mulani, S. B., Kapania, R. K., and Schetz, J. A., "Control Power Optimization using Artificial Intelligence for Hybrid Wing Body Aircraft," *16th AIAA/ISSMO Multidisciplinary Analysis and Optimization Conference*, AIAA-2015-2323, Dallas, TX, 2015.

[27] Garmendia, D. C. and Mavris, D. N., "Alternative Trim Analysis Formulations for Vehicles with Redundant Multi-Axis Control Surfaces," *Journal of Aircraft*, Vol. 53, No. 1, 2016, pp. 60–72.

[28] Méheut, M., Grenon, R., Carrier, G., Defos, M., and Duffau, M., "Aerodynamic Design of Transonic Flying Wing Configurations," *CEAS Katnet II Conference on Key Aerodynamic Technologies*, Breme, Germany, May 2009.

[29] Rahman, N. U. and Whidborne, J. F., "A Lateral Directional Flight Control System for the MOB Blended Wing Body Planform," *International Conference on Control*, Manchester, UK, 2008.

[30] Plas, A. P., Madani, V., Sargeant, M. A., Greitzer, E. M., Hall, C. A., and Hynes, T. P., "Performance of a Boundary Layer Ingesting (BLI) Propulsion System," *45th Aerospace Sciences Meeting*, AIAA-2007-0450, Reno, NV, 2007.

[31] Kawai, R. T., Friedman, D. M., and Serrano, L., "Blended Wing Body (BWB) Boundary Layer Ingestion (BLI) Inlet Configuration and System Studies," Tech. Rep. NASA/CR2006-214534, The Boeing Company, Huntington Beach, CA, 2006.

[32] Owens, L. R., Allan, B. G., and Gorton, S. A., "Boundary-Layer-Ingesting Inlet Flow Control," *Journal of Aircraft*, Vol. 45, No. 4, 2008, pp. 1431–4440.

[33] Kim, H. and Liou, M.-S., "Flow Simulation of N3B Hybrid Wing Body Configuration," *50th AIAA Aerospace Sciences Meeting*, AIAA-2012-0838, Nashville, TN, January 2012.

[34] Leifsson, L., Ko, A., Mason, W., Schetz, J., Grossman, B., and Haftka, R., "Multidisciplinary Design Optimization of Blended-Wing-Body Transport Aircraft with Distributed Propulsion," *Aerospace Science and Technology*, Vol. 25, No. 1, 2013, pp. 16–28.

[35] Kim, H. and Liou, M.-S., "Flow Simulation of N3-X Hybrid Wing-Body Configuration," *31st AIAA Applied Aerodynamics Conference*, AIAA-2013-0221, San Diego, CA, June 2013.

[36] Papamoschou, D. and Mayoral, S., "Jet Noise Shielding for Advanced Hybrid Wing-Body Configurations," *49th AIAA Aerospace Sciences Meeting*, AIAA-2011-0912, Orlando, FL, 2011.

[37] Czech, M. J., Thomas, R. H., and Elkoby, R., "Propulsion Airframe Aeroacoustic Integration Effects for a Hybrid Wing Body Aircraft Configuration," *International Journal of Aeroacoustics*, Vol. 11, No. 3, 2012, pp. 335–367.

[38] Clark, L. R. and Gerhold, C. H., "Inlet Noise Reduction by Shielding for the Blended-Wing-Body Airplane," *5th AIAA/CEAS Aeroacoustics Conference*, AIAA-1999-1937, Seattle, WA, 1999.

[39] Guo, Y., Burley, C. L., and Thomas, R. H., "On Noise Assessment for Blended Wing Body Aircraft," *52nd AIAA Aerospace Sciences Meeting*, AIAA-2014-0365, National Harbor, MD, 2014.

[40] Guo, Y., Czech, M. J., and Thomas, R. H., "Open Rotor Noise Shielding by Blended-Wing-Body Aircraft," *53rd AIAA Aerospace Sciences Meeting*, AIAA-2015-1214, Kissimmee, FL, 2015.

[41] Agarwal, A. and Dowling, A. P., "Low-Frequency Acoustic Shielding by the Silent Aircraft Airframe," *AIAA Journal*, Vol. 45, No. 2, 2007, pp. 358–365.

[42] Ng, L. W. T. and Spakovszky, Z. S., "Noise Shielding Assessment of Hybrid Wing-Body Aircraft Configurations," *AIAA Journal*, Vol. 49, No. 11, 2011, pp. 2444–2452.

[43] Guo, Y., Brusniak, L., Czech, M., and Thomas, R., "Hybrid Wing Body (HWB) Slat Noise Analysis," *51st AIAA Aerospace Sciences Meeting*, AIAA-2013-0462, Grapevine, TX.

[44] Hileman, J. I., Spakovszky, Z. S., Drela, M., Sargeant, M. A., and Jones, A., "Airframe Design for Silent Fuel-Efficient Aircraft," *Journal of Aircraft*, Vol. 47, No. 3, 2010, pp. 956–969.

[45] Ghigliazza, H. H., Martínez-Val, R., Perez, E., and Smrcek, L., "Wake of Transport Flying Wings," *Journal of Aircraft*, Vol. 44, No. 2, 2007, pp. 558–562.

[46] Martinez-Val, R., Cuerno, C., Pérez, E., and Ghigliazza, H. H., "Potential Effects of Blended Wing Bodies on the Air Transportation System," *Journal of Aircraft*, Vol. 47, No. 5, 2010, pp. 1599–1604.

[47] van der Voet, Z., Geuskens, F. J. J. M. M., Ahmed, T. J., van Eyben, B. N., and Beukers, A., "Configuration of the Multibubble Pressure Cabin in Blended Wing Body Aircraft," *Journal of Aircraft*, Vol. 49, No. 4, 2012, pp. 991–1007.

[48] Galea, E. R., Filippidis, L., Wang, Z., and Ewer, J., "Fire and evacuation analysis in BWB aircraft configurations: computer simulations and large-scale evacuation experiment," *The Aeronautical Journal*, Vol. 114, No. 1154, 2010, pp. 271–277.

[49] Sturm, R. and Hepperle, M., "Crashworthiness and Ditching Behaviour of Blended-Wing-Body (BWB) Aircraft Design," *International Journal of Crashworthiness*, Vol. 20, No. 6, 2015, pp. 592–601.

[50] Willcox, K. and Wakayama, S., "Simultaneous Optimization of a Multiple Aircraft Family," *Journal of Aircraft*, Vol. 40, No. 4, 2003, pp. 616–622.

[51] Morris, A. J., "MOB: A European Distributed Multi-Disciplinary Design and Optimisation Project," *9th AIAA/ISSMO Symposium on Multidisciplinary Analysis and Optimization*, AIAA-2002-5444, Atlanta, GA, September 2002.

[52] Morris, A. J., Arendsen, P., La Rocca, G., Voss, R., and Hönlinger, H., "MOB - A European Project on Multidisciplinary Design Optimisation," *24th International Congress of the Aeronautical Sciences*, Yokohama, Japan, September 2004.

[53] Qin, N., Vavalle, A., Le Moigne, A., Laban, M., Hackett, K., and Weinerfelt, P., "Aerodynamic Considerations of Blended Wing Body Aircraft," *Progress in Aerospace Sciences*, Vol. 40, No. 6, 2004, pp. 321–343.

[54] Siouris, S. and Qin, N., "Study of the Effects of Wing Sweep on the Aerodynamic Performance of a Blended Wing Body Aircraft," *Journal of Aerospace Engineering*, Vol. 221, No. 1, 2007, pp. 47–55.

[55] Strüber, H. and Hepperle, M., "Aerodynamic Optimisation of a Flying Wing Transport Aircraft," *New Results in Numerical and Experimental Fluid Mechanics*, Vol. 92, 2006, pp. 69–76.

[56] Mialon, B. and Hepperle, M., "Flying Wing Aerodynamics Studies at ONERA and DLR," Tech. Rep. TP 2005-122, ONERA, Catillon Cedex, France, 2005.

[57] Hansen, L. U., Heinze, W., and Horst, P., "Blended Wing Body Structures in Multidisciplinary Pre-Design," *Structural and Multidisciplinary Optimization*, Vol. 38, No. 1, 2008, pp. 93–106.

[58] Voskuijl, M., La Rocca, G., and Dircken, F., "Controllability of Blended Wing Body Aircraft," *26th International Congress of the Aeronautical Sciences*, Anchorage, AL, September 2008.

[59] "NACRE Final Activity Report 2005-2010," Tech. rep., 2011.

[60] Kozek, M. and Schirrer, A., editors, *Modeling and Control for a Blended Wing Body Aircraft*, Springer, 2015.

[61] Bolsunovsky, A., Buzoverya, N., Gurevich, B., Denisov, V., Dunaevsky, A., Shkadov, L., Sonin, O., Udzhuhu, A., and Zhurihin, J., "Flying Wing - Problems and Decisions," *Aircraft Design*, Vol. 4, No. 4, 2001, pp. 193–219.

[62] Liebeck, R. H., Page, M. A., and Rawdon, B. K., "Blended Wing Body Subsonic Commercial Transport," *36th AIAA Aerospace Sciences Meeting and Exhibit*, AIAA-1998-0438, Reno, NV, 1998.

[63] Vicroy, D. D., "Blended-Wing-Body Low-Speed Flight Dynamics: Summary of Ground Tests and Sample Results," *47th AIAA Aerospace Sciences Meeting and Exhibit*, AIAA-2009-0933, Orlando, FL, January 2009.

[64] Risch, T., Cosentino, G., Regan, C., Kisska, M., and Princen, N., "X-48B Flight Test Progress Overview," *47th AIAA Aerospace Sciences Meeting*, AIAA-2009-0934, Orlando, FL, 2009.

[65] Bradley, M. K. and Droney, C. K., "Subsonic Ultra Green Aircraft Research Phase II: N+4 Advanced Concept Development," Tech. Rep. NASA/CR-2012-217556, National Aeronautics and Space Administration, 2012.

[66] Pitera, D. M., DeHaan, M., Brown, D., Kawai, R. T., Hollowell, S., Camacho, P., Bruns, D., and Rawden, B. K., "Blended Wing Body Concept Development with Open Rotor Engine Intergration," Tech. Rep. NASA/CR2011-217303, The Boeing Company, Huntington Beach, CA, 2011.

[67] Gern, F. H., "Conceptual Design and Structural Analysis of an Open Rotor Hybrid Wing Body Aircraft," *54th AIAA/ASME/ASCE/AHS/ASC, Structures, Structural Dynamics, and Materials Conference*, AIAA-2013-1688, Boston, MA, 2013.

[68] Greitzer, E. M., "N+3 Aircraft Concept Designs and Trade Studies Final Report," Tech. rep., Massachusetts Institute of Technology, 2010.

[69] Gatlin, G. M., Vicroy, D. D., and Carter, M. B., "Experimental Investigation of the Low-Speed Aerodynamic Characteristics of a 5.8-Percent Scale Hybrid Wing Body Configuration," *30th AIAA Applied Aerodynamics Conference*, AIAA-2012-2669, New Orleans, LA, 2012.

[70] Nickol, C. L., "Hybrid Wing Body Configuration Scaling Study," *50th AIAA Aerospace Sciences Meeting and Exhibit*, AIAA-2012-0337, Nashville, TN, January 2012.

[71] Jameson, K. K., Marshall, D. D., Golden, R., Paciano, E., Englar, R. J., Gaeta, R. J., Paterson, J., and Mason, D., "Part 1: The Wind Tunnel Model Design and Fabrication of Cal Polys AMELIA 10 Foot Span Hybrid Wing-Body Low Noise CESTOL Aircraft," *49th AIAA Aerospace Sciences Meeting*, AIAA-2011-1306, Orlando, FL, 2011.

[72] Peigin, S. and Epstein, B., "Computational Fluid Dynamics Driven Optimization of Blended Wing Body Aircraft," *AIAA Journal*, Vol. 44, No. 11, 2006, pp. 2736–2745.

[73] Qin, N., Vavelle, A., and Le Moigne, A., "Spanwise Lift Distribution for Blended Wing Body Aircraft," *Journal of Aircraft*, Vol. 42, No. 2, 2005, pp. 356–365.

[74] Le Moigne, A. and Qin, N., "Aerofoil Profile and Sweep Optimisation for a Blended Wing-Body Aircraft Using A Discrete Adjoint Method," *The Aeronautical Journal*, Vol. 110, No. 1111, 2006, pp. 589–604.

[75] Osusky, L. and Zingg, D. W., "Application of an Efficient Newton-Krylov Algorithm for Aerodynamic Shape Optimization Based on the Reynolds-Averaged Navier-Stokes Equations," *21st AIAA Computational Fluid Dynamics Conference*, AIAA-2013-2584, San Diego, CA, June 2013.

[76] "Aerodynamic Shape Optimizations of a Blended Wing Body Configuration for Several Wing Planforms," *30th AIAA Applied Aerodynamics Conference*, AIAA-2012-3122, New Orleans, LA, June 2012.

[77] Lyu, Z. and Martins, J. R. R. A., "Aerodynamic Shape Optimization Studies of a Blended-Wing-Body Aircraft," *Journal of Aircraft*, Vol. 51, No. 5, 2014, pp. 1604–1617.

[78] Kuntawala, N. B., Hicken, J. E., and Zingg, D. W., "Preliminary Aerodynamic Shape Optimization of a Blended-Wing-Body Aircraft Configuration," *49th AIAA Aerospace Sciences Meeting*, AIAA-2011-0642, Orlando, FL, January 2011.

[79] Hicken, J. E. and Zingg, D. W., "A Parallel Newton-Krylov Solver for the Euler Equations Discretized Using Simultaneous Approximation Terms," *AIAA Journal*, Vol. 46, No. 11, 2008, pp. 2773–2786.

[80] Hicken, J. E. and Zingg, D. W., "Aerodynamic Optimization Algorithm with Integrated Geometry Parameterization and Mesh Movement," *AIAA Journal*, Vol. 48, No. 2, 2010, pp. 401–413.

[81] Hicken, J. E., *Efficient Algorithms for Future Aircraft Design: Contributions to Aerodynamic Shape Optimization*, Ph.D. thesis, University of Toronto, 2009.

[82] Osusky, M. and Zingg, D. W., "A Parallel Newton-Krylov-Schur Flow Solver for the Navier-Stokes Equations Discretized Using Summation-By-Parts Operators," *AIAA Journal*, Vol. 51, No. 12, 2013, pp. 2833–2851.

[83] Osusky, M., *A Parallel Newton-Krylov-Schur Algorithm for the Reynolds-Averaged Navier-Stokes Equations*, Ph.D. thesis, University of Toronto, 2013.

[84] Osusky, L., Buckley, H., Reist, T., and Zingg, D. W., "Drag Minimization Based on the Navier-Stokes Equations Using a Newton-Krylov Approach," *AIAA Journal*, Vol. 53, No. 6, 2015, pp. 1555–1577.

[85] Osusky, L. M., *A Numerical Methodology for Aerodynamic Shape Optimization in Turbulent Flow Enabling Large Geometric Variation*, Ph.D. thesis, University of Toronto, 2014.

[86] Telidetzki, K., Osusky, L., and Zingg, D. W., "Application of Jetstream to a Suite of Aerodynamic Shape Optimization Problems," *52nd Aerospace Sciences Meeting*, AIAA-2014-0571, National Harbor, MD, January 2014.

[87] Lee, C., Koo, D., Telidetzki, K., Buckley, H., Gagnon, H., and Zingg, D. W., "Aerodynamic Shape Optimization of Benchmark Problems Using Jetstream," *53rd AIAA Aerospace Sciences Meeting*, AIAA-2015-0262, Kissimmee, FL, January 2015.

[88] Koo, D. and Zingg, D. W., "Progress in Aerodynamic Shape Optimization Based on the Reynolds-Averaged Navier-Stokes Equations," *54th Aerospace Sciences Meeting*, AIAA-2016-1292, San Diego, CA, January 2016.

[89] Hicken, J. E. and Zingg, D. W., "Induced Drag Minimization of Nonplanar Geometries Based on the Euler Equations," *AIAA Journal*, Vol. 48, No. 11, 2010, pp. 2564–2575.

[90] Leung, T. M. and Zingg, D. W., "Aerodynamic Shape Optimization of Wings Using a Parallel Newton-Krylov Approach," *AIAA Journal*, Vol. 50, No. 3, 2012, pp. 540–550.

[91] Leung, T. M. and Zingg, D. W., "Design of Low-Sweep Wings for Maximum Range," *29th AIAA Applied Aerodynamics Conference*, AIAA-2011-3178, Honolulu, HI, June 2011.

[92] Chernukhin, O. and Zingg, D. W., "Multimodality and Global Optimization in Aerodynamic Design," *AIAA Journal*, Vol. 51, No. 6, 2013, pp. 1342–1354.

[93] Gagnon, H. and Zingg, D. W., "Geometry Generation of Complex Unconventional Aircraft with Application to High-Fidelity Aerodynamic Shape Optimization," *21st AIAA Computational Fluid Dynamics Conference*, AIAA-2013-2850, San Diego, CA, June 2013.

[94] Reist, T. A. and Zingg, D. W., "Aerodynamic Shape Optimization of a Blended-Wing-Body Regional Transport for a Short Range Mission," *31st AIAA Applied Aerodynamics Conference*, AIAA-2013-2414, San Diego, CA, June 2013.

[95] Reist, T. A. and Zingg, D. W., "Optimization of the Aerodynamic Performance of Regional and Wide-Body-Class Blended Wing-Body Aircraft," *33rd AIAA Applied Aerodynamics Conference*, AIAA-2015-3239, Dallas, TX, June 2015.

[96] Zhang, Z. J., Khosravi, S., and Zingg, D. W., "High-Fidelity Aerostructural Optimization with Integrated Geometry Parameterization and Mesh Movement," *56th AIAA/ASCE/AHS/ASC Structures, Structural Dynamics, and Materials Conference*, AIAA-2015-1132, Kissimmee, FL, January 2015.

[97] Khosravi, S. and Zingg, D. W., "A Numerical Optimization Study on Winglets," *15th AIAA/ISSMO Multidisciplinary Analysis and Optimization Conference*, AIAA-2014-2173, Atlanta, GA, June 2014.

[98] Jameson, A. and Reuther, J., "Control Theory Based Airfoil Design Using the Euler Equations," *IAA/USAF/NASA/ISSMO Symposium on Multidisciplinary Analysis and Optimization*, Panama City Beach, 1984.

[99] Hicks, R. M. and Henne, P. A., "Wing Design by Numerical Optimization," *Journal of Aircraft*, Vol. 15, No. 7, 1978, pp. 407–412.

[100] Kulfan, B. M., "A Universal Paramtric Geometry Representation Method CST," *The 45th AIAA Aerospace Sciences Meeting and Exhibit*, AIAA-2007-0062, Reno, NV, January 2007.

[101] Sederberg, T. W. and Parry, S. R., "Free-Form Deformation of Solid Geometric Models," *Proceedings of the 13th Annual Conference on Computer Graphics and Interactive Techniques*, New York, NY, 1986.

[102] Truong, A. H. and Zingg, D. W., "Surface Mesh Movement Algorithm for Computer-Aided-Design-Based Aerodynamic Shape Optimization," *AIAA Journal*, Vol. 54, No. 2, 2016, pp. 542–556.

[103] Jakobsson, S. and Amoignon, O., "Mesh Deformation Using Radial Basis Functions for Gradient-Based Aerodynamic Shape Optimization," *Computers and Fluids*, Vol. 36, No. 6, 2007, pp. 11191136.

[104] Truong, A. H., Oldfield, C. A., and Zingg, D. W., "Mesh Movement for a Discrete-Adjoint Newton-Krylov Algorithm for Aerodynamic Optimization," *AIAA Journal*, Vol. 46, No. 7, 2008, pp. 1695–1704.

[105] Balay, S., Gropp, W. D., McInnes, L. C., and Smith, B. F., "Efficient Management of Parallelism in Object Oriented Numerical Software Libraries," *Modern Software Tools in Scientific Computing*, edited by E. Arge, A. M. Bruaset, and H. P. Langtangen, Birkhäuser Press, 1997, pp. 163–202.

[106] Spalart, P. R. and Allmaras, S. R., "One-Equation Turbulence Model for Aerodynamic Flows," *30th AIAA Aerospace Sciences Meeting and Exhibit*, AIAA-0092-0439, Reno, NV, 1992.

[107] Del Rey Fernández, D. C., Hicken, J. E., and Zingg, D. W., "Review of Summation-by-Parts Operators with Simultaneous Approximation Terms for the Numerical Solution of Partial Differential Equations," *Computers and Fluids*, Vol. 95, 2014, pp. 171–196.

[108] Hicken, J. E. and Zingg, D. W., "A Simplified and Flexible Variant of GCROT for Solving Nonsymmetric Linear Systems," *SIAM Journal of Scientific Computing*, Vol. 32, No. 3, 2010, pp. 1672–1694.

[109] Osusky, M., Boom, P. D., and Zingg, D. W., "Results from the Fifth AIAA Drag Prediction Workshop obtained with a parallel Newton-Krylov-Schur flow solver discretized using summation-by-parts operators," *31st AIAA Applied Aerodynamics Conference*, AIAA-2013-2511, San Diego, CA, June 2013.

[110] Holland, J. H., *Adaptation in Natural and Artificial Systems*, MIT Press, Cambridge, MA, USA, 1992.

[111] Zingg, D. W., Nemec, M., and Pulliam, T. H., "A Comparative Evaluation of Genetic and Gradient-Based Algorithms Applied to Aerodynamic Optimization," *European Journal of Computational Mechanics*, Vol. 17, No. 1, 2008, pp. 103–126.

[112] Gill, P. E., Murray, W., and Saunders, M. A., "SNOPT: An SQP Algorithm for Large-Scale Constrained Optimization," *Society for Industrial Applied Mathematics Review*, Vol. 47, No. 1, 2005, pp. 99–131.

[113] Pironneau, O., "On Optimum Design in Fluid Mechanics," *Journal of Fluid Mechanics*, Vol. 61, No. 1, 1974, pp. 97–110.

[114] Jameson, A., "Aerodynamic Design via Control Theory," *Journal of Scientific Computing*, Vol. 3, No. 3, 1988, pp. 233–260.

[115] Embraer Commercial Aircraft, *Embraer 190 Airport Planning Manual*, 2005, (Revision 10 - 18 February 2013).

[116] Boeing Commercial Airplanes, *737 Airplane Characteristics for Airport Planning*, 2013.

[117] Boeing Commercial Airplanes, *767 Airplane Characteristics for Airport Planning*, 2005.

[118] Boeing Commercial Airplanes, *777-200LR/-300ER/-Freighter Airplane Characteristics for Airport Planning*, 2009.

[119] Torenbeek, E., *Synthesis of Subsonic Airplane Design*, Delft University, 1976.

[120] "Aircraft Design: Synthesis and Analysis," http://adg.stanford.edu/aa241/AircraftDesign.html, December 2014.

[121] Bradley, K. R., "A Sizing Methodology for the Conceptual Design of Blended-Wing-Body Transports," Tech. Rep. NASA/CR-2004-213016, NASA/Langley Research Center: Joint Institute for Advancement of Flight Sciences, 2004.

[122] Thomas, R. H., Czech, M. J., and Doty, M. J., "High Bypass Ratio Jet Noise Reduction and Installation Effects Including Shielding Effectiveness," *51st Aerospace Sciences Meeting*, AIAA-2013-0541, Grapevine, TX.

[123] Hooker, J. R., "Design of a Hybrid Wing Body for Fuel Efficient Air Mobility Operations at Transonic Flight Conditions," *52nd AIAA Aerospace Sciences Meeting*, AIAA-2014-1285, National Harbor, MD, 2014.

[124] Richardson, L. F. and Gaunt, J. A., "The Deferred Approach to the Limit," *Philosophical Transactions of the Royal Society*, Vol. 226, No. 636-646, 1927, pp. 299–349.

[125] Mavriplis, D. J., Vassberg, J. C., Tinoco, E. N., Mani, M., Brodersen, O. P., Eisfeld, B., Wahls, R. A., Morrison, J. H., Zickuhr, T., Levy, D., and Murayama, M., "Grid Quality and Resolution Issues from the Drag Prediction Workshop Series," *Journal of Aircraft*, Vol. 46, No. 3, 2009, pp. 935–950.

[126] Buckley, H. P. and Zingg, D. W., "An Approach to Aerodynamic Design Through Numerical Optimization," *AIAA Journal*, Vol. 51, No. 8, 2013, pp. 1972–1981.

[127] Mialon, B., Fol, T., and Bonnaud, C., "Aerodynamic Optimization of Subsonic Flying Wing Configurations," *20th AIAA Applied Aerodynamics Conference*, AIAA-2002-2931, St. Louis, MO, 2002.

[128] Roskam, J., *Airplane Design Part V: Component Weight Estimation*, Aviation and Engineering Corporation, 1989.

Appendix A

Low-Fidelity Conceptual Design Tool

While high-fidelity aerodynamic shape optimization is accurate and allows for detailed design, its computational expense renders it, for now, infeasible for full system-level design. However, for the optimizations presented in this work, estimates of aircraft weight and CG location are required for the high-fidelity ASO. To obtain these, a low-fidelity conceptual design tool, called 'Suite for Parametric Aircraft Design and Evaluation' (SPADE), has been developed to allow for their determination.

For a specified planform, engine parameters, cabin and payload information, and a number of points on a desired payload-range diagram, SPADE computes the corresponding aircraft structural and fuel weights. The tool is constructed in a modular way such that new weight and aerodynamic models can be inserted such as may be required for the analysis of unconventional aircraft. For example, models for either a cylindrical or 'home plate' shaped pressure vessel can be chosen for the analysis of either CTW or HWB designs.

A.1 Aerodynamic and Weight Models

The main purpose of SPADE is the determination of aircraft weights, and the change in weight during flight, such that these can be used for the high-fidelity ASO. Thus, most emphasis is placed on the structural models. A number of component types are included:

- Wing
- Horizontal stabilizer
- Vertical stabilizer
- Cylindrical fuselage

- Home plate shaped pressure vessel and center-body (for HWBs)
- Propulsion
- Operational
- Fuel

For each of these components, with the exception of the HWB center-body, the weight models of Torenbeek [119], Roskam [128], Raymer [15], and Kroo [120], were tested. A series of aircraft and payload-range diagrams were reconstructed to correspond to the Embraer E190, Boeing 737-800, and Boeing 777-200LR, and the weight breakdown was analyzed for each of these aircraft with the different models, and combinations thereof. While certain models worked best for different aircraft classes, it was found that taking the average of the weights predicted by Torenbeek's and Kroo's models gave the best agreement over the range of aircraft classes. For the HWB center-body, the model of Bradley [121] is used. Fuel weights are calculated via the Breguet equation for cruise and using fuel fractions for other phases of flight.

Aerodynamic performance, including lift, drag, and pitching moment, are calculated using the relations provided by Raymer [15]. The aerodynamic prediction comes into the weight estimation via the use of the Breguet equation for cruise fuel.

The solution strategy is summarized as follows:

1. Specify:
   (a) Aircraft geometry
   (b) Propulsion system info (geometry, weight, TSFC)
   (c) A number of required payload/range combinations and operating conditions
2. Solve:
   (a) For each mission, in an iterative manner, calculate the aerodynamic coefficients (via the Prandtl-Schlichting relation with form factors for parasitic drag, span efficiency factors for induced drag, Korn equation for wave drag), fuel weights (via the Breguet equation for cruise and fuel factors for other missions segments), structural weights (via Torenbeek, Kroo, and Bradley relations.)
   (b) Resulting weight information from the different missions is used to determine the system weights, i.e. MTOW, max fuel, MZFW, etc., as well as weight and CG variations throughout the various missions.

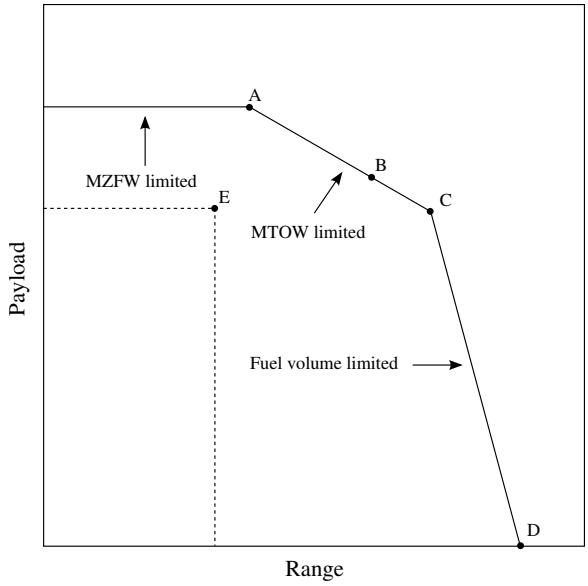

Figure A.1: A notional payload-range diagram with points A-D used for aircraft sizing. Point E is the nominal mission point.

A.2 Validation

To validate SPADE and to determine any correction factors, models for regional, narrow-body, and wide-body aircraft are constructed. These are designed to replicate the E190, B737-800, and B777-200LR. For sizing, four points are taken from the payload-range diagrams published in each type's airport planning manual (APM), References 115, 116, and 118, respectively, to correspond with points A, B, C, and D shown in Figure A.1. Point A corresponds to maximum range with maximum payload, point B is the point for maximum range with maximum passenger payload (i.e. full PAX at 220 lbs/PAX), point C corresponds to MTOW with full fuel, and point D is that for ferry range.

A comparison of the weights predicted by SPADE with those in the APMs is shown in Table A.1. For the regional-jet the default models underpredict the structural weights, thus a 10% correction factor is applied to obtain the results in Table A.1 and for the rest of this thesis. No correction factors are needed for the narrow and wide-body designs. With the exception of MFW for the regional-jet, all weight estimates are within 4% of their reference values, with the MTOW estimates within about 1%.

Since SPADE is also to be used for sizing the HWBs, it must be validated for this configuration as well as for CTWs. Nickol's scaling study provides a range of aircraft sizes against which to compare [70]. One difference between that work and this thesis is his use of advanced technology factors to account for things such as laminar flow, advanced engines,

Table A.1: A comparison of the weights predicted by SPADE with existing reference aircraft.

Aircraft	Model	MTOW [lb]	OEW [lb]	MZFW [lb]	MFW [lb]
E190	Reference 115	105,400	61,500	89,900	28,700
	SPADE	105,900	59,200	87,600	27,100
	Difference	+0.5%	−3.7%	−2.6%	−5.6%
B737-800	Reference 116	174,200	91,300	138,300	46,100
	SPADE	173,500	87,700	134,700	46,000
	Difference	−0.4%	−3.9%	−2.6%	−0.2%
B777-200LR	Reference 118	766,000	320,000	461,000	320,900
	SPADE	775,500	330,900	471,900	313,900
	Difference	+1.2%	+3.4%	+2.3%	−2.2%

and advanced materials. Estimates for these technology factors are taken from his paper and converted into scaling factors for weight, drag, and engine size/efficiency. For the tube-and-wing (TW) designs, only the wing span and aspect ratio are given by Nickol. Thus, the fuselage and empennage are assumed to be the same as the existing reference aircraft upon which the TW designs are based, and the wing is simply scaled to give the correct span and aspect ratio. Using this geometry and these technology factors, models for the advanced TW regional-jet, narrow-body, and wide-body designs, referred to as the TW98, TW160, and TW301, respectively, are created and analyzed in SPADE, the results of which are shown in Table A.2. The SPADE and reference MTOW, OEW, and MZFW for each design agree within 7%. This is a larger variation than the first validation case due to the uncertainty in the advanced technology factors and the missions. There are larger differences in the fuel weight. These are likely due to differences in the flight profile between the two analyses, as the reference lacked sufficient detail of the flight profile, thus necessitating assumptions.

Similarly, models are created for Nickol's regional-jet, narrow-body, and wide-body hybrid wing-body (HWB) designs, referred to as the HWB98, HWB160, and HWB301, respectively. Again, his advanced technology factors are applied. The resulting weight comparisons are shown in Table A.3. As with the TW designs, the MTOW, OEW and MZFW weights are relatively accurately predicted, within 3%, but there are large uncertainties in both the aerodynamic performance and fuel weights.

SPADE agrees well with the existing CTW aircraft, while comparison with Nickol's advanced designs becomes harder due to assumptions which must be made about the advanced technology factors and mission profiles. For this work, the low-fidelity models included in

Table A.2: A comparison of the weights predicted by SPADE with the TW results of Nickol. For comparison with Nickol's results, his advanced technology factors for weight, drag, and engine performance are applied to the SPADE models.

Aircraft	Model	MTOW [lb]	OEW [lb]	MZFW [lb]	L/D [–]	Block fuel [lb]
TW98	Reference 70	91,700	55,000	76,600	19.8	12,500
	SPADE	93,200	53,100	74,800	20.8	14,000
	Difference	+1.6%	−3.5%	−2.3%	+5.1%	+12.0%
TW160	Reference 70	140,700	76,400	114,200	19.8	22,000
	SPADE	145,400	75,700	113,400	20.4	25,000
	Difference	+3.3%	−0.9%	−0.7%	+3.0%	+13.6%
TW301	Reference 70	539,900	248,900	367,000	21.5	155,900
	SPADE	574,900	260,100	378,200	21.6	167,600
	Difference	+6.5%	+4.5%	+3.1%	+0.5%	+7.5%

Table A.3: A comparison of the weights predicted by SPADE with the HWB results of Nickol. For comparison with Nickol's results, his advanced technology factors for weight, drag, and engine performance are applied to the SPADE models.

Aircraft	Model	MTOW [lb]	OEW [lb]	MZFW [lb]	L/D [–]	Block fuel [lb]
HWB98	Reference 70	101,000	63,300	84,900	20.7	13,000
	SPADE	103,600	62,500	84,100	23.0	14,600
	Difference	+2.6%	−1.3%	−0.9%	+11.1%	+12.3%
HWB160	Reference 70	166,100	100,800	138,500	23.1	22,900
	SPADE	170,100	98,700	136,500	24.7	25,800
	Difference	+2.4%	−2.1%	−1.4%	+6.9%	+12.7%
HWB301	Reference 70	542,600	261,300	379,400	23.5	146,600
	SPADE	551,400	272,000	390,100	27.5	135,100
	Difference	+1.6%	+4.1%	+2.8%	+17.0%	−7.8%

SPADE are deemed sufficiently accurate to provide the basis for the high-fidelity optimizations. In the future, higher-fidelity sizing models, particularly for the HWBs, would be a great asset in more accurately predicting performance.

Appendix B

Geometric Scaling of HWB Aircraft

One of the oft-quoted benefits of the HWB concept is its lower wetted area than comparable conventional tube-and-wing designs for a given internal volume [13]. However simply using internal volume as a metric for capacity over-simplifies the problem. To investigate how the wetted area benefit of HWBs scales with aircraft size and shape, a simple geometric model for HWBs is constructed, from which the wetted area can be approximated in order to understand its correlation with aircraft size and shape.

This model consists of a conventional cylindrical fuselage of a given cabin length and height, with the nose and tail cone modelled as a semi-sphere and cone, respectively. This can be converted to an HWB by 'exploding' the cylinder laterally and adding a home plate shaped center plug in the cabin with the leading edge being a half cylinder and a wedge aft of the cabin. This model is shown in Figure B.1. For a zero width center plug this model reduces to a cylindrical fuselage. For a given fuselage height, the length of the aft tail-wedge is determined by assuming a slope of the upper and lower surfaces of 15%, similar to existing transonic airfoils. For a given cabin length, height, center plug width, sweep angle (50°), and tail cone slope (15%) the fuselage geometry is fully defined, and the cabin floor area and the fuselage wetted area can be calculated. In addition, the 'masking' of wing area by the fuselage is accounted for. For a number of existing aircraft ranging from regional jets to large wide-bodies, correlations are made for wing span, b, and area, S, as a function of cabin floor area, A. These are found to be approximately $b = 2.062A^{0.574}$ and $S = 0.712A^{1.089}$, respectively, for A in square feet. Assuming a taper ratio of 0.1 allows for the determination of the size of a trapezoidal wing, also shown in Figure B.1. The portion of the wing covered by the fuselage does not contribute to the wetted area.

First, this model is used to determine the wetted area per unit cabin floor area, S_{wet}/A, of conventional designs, i.e. with zero center plug width. For a 100-passenger design the floor

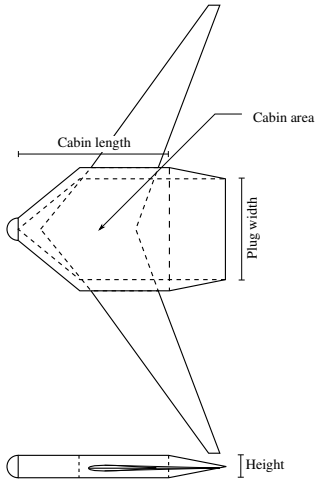

Figure B.1: Simple geometric model for a generic HWB.

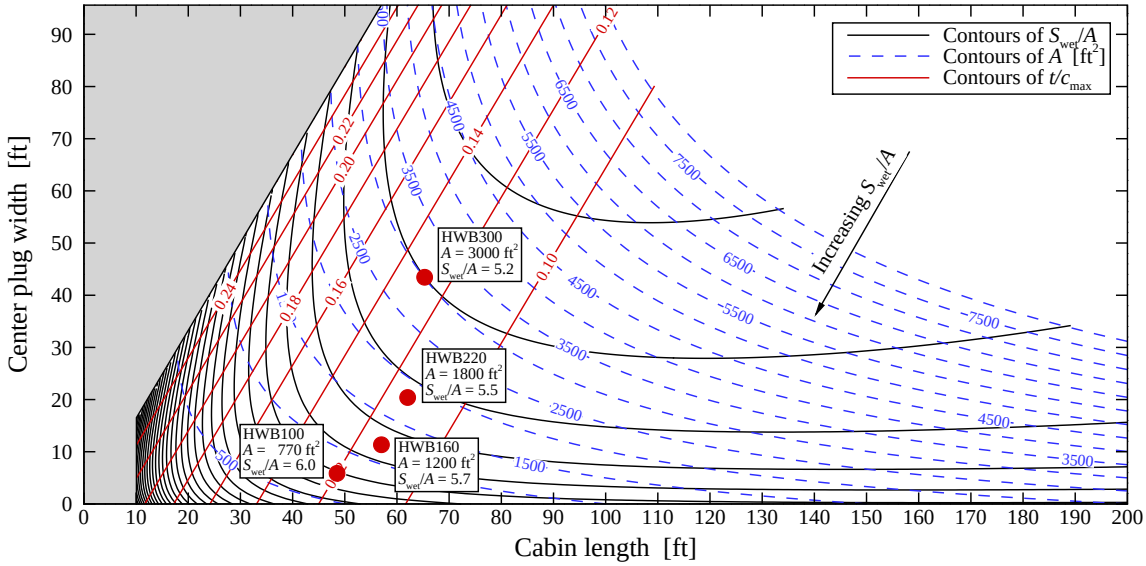

Figure B.2: Wetted area per unit floor area, S_{wet}/A, for a parametric HWB with a fuselage height of 10 ft, where A is the cabin floor area and S_{wet} is the wetted area.

area requirement is approximately 770 ft^2, a height of 10 ft; this yields $S_{\text{wet}}/A = 6.2$. A 300-passenger design requires a cabin floor area of approximately 3,000 ft^2 and has a height of 20 ft, resulting in $S_{\text{wet}}/A = 6.5$. A model of S_{wet}/A for HWBs is now created. A center plug is added to a 10 ft height design, with the resulting contours of S_{wet}/A shown in Figure B.2. This model reveals two important ideas: 1) The shape for a small HWB which minimizes S_{wet}/A, marked as HWB100 in Figure B.2 and shown in Figure B.3, has a slender fuselage with only a narrow center plug, while the optimal large HWB has a wide center-body as

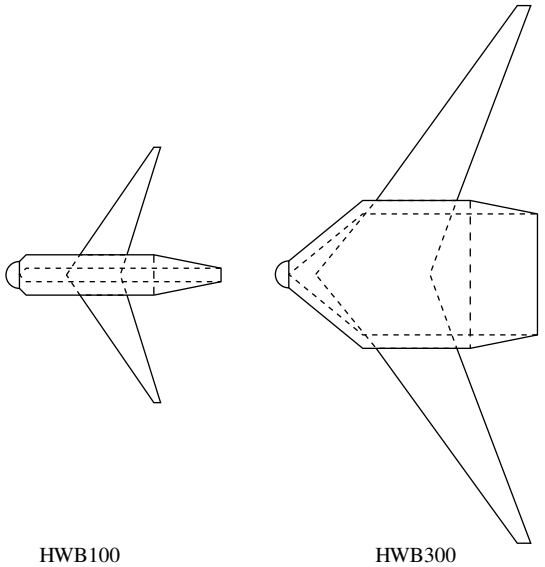

Figure B.3: The HWB shapes for minimum S_{wet}/A for 100 and 300-passenger HWBs as predicted by the model in Figure B.2.

indicated in Figure B.2 and shown in Figure B.3. 2) The S_{wet}/A for the small HWB is only 3% lower than the similarly sized conventional tube-and-wing, while for the large HWB this benefit is 20%.

While this 10 ft diameter does provide sufficient underfloor cargo volume, the cargo compartment height is less than 3 ft which would preclude the use of existing unit load devices (ULDs) and present operational challenges, particularly for larger aircraft. Should a larger height of 15 ft be used to accommodate LD3s, the same trends still hold; however the minimum S_{wet}/A shape is longer with a smaller plug width, and the magnitude of S_{wet}/A for a given floor area is increased. This 15 ft height would not be practical for the 100-passenger design, as the fuselage would reduce to a conventional cylinder and become very short. However, for the 300-passenger design, this larger diameter would likely be required in order to house the ULDs, in which case S_{wet}/A increases from 5.2 to 5.8, still 11% lower than the conventional reference.

This is a very simple analysis which neglects many considerations and simply tries to minimize wetted area. However, it provides suggestions as to what the optimal shape would be to minimize the wetted area for a given capacity. Of course, this simple model neglects many considerations, such as transonic performance, and higher-fidelity analysis is required to lend credibility to these conclusions.